Monthly Notices of the ROYAL ASTRONOMICAL SOCIETY

MNRAS **505,** 4048–4085 (2021) https://doi.org/10.1093/mnras/stab1537
Advance Access publication 2021 May 27

WISDOM Project – IX. Giant molecular clouds in the lenticular galaxy NGC 4429: effects of shear and tidal forces on clouds

Lijie Liu [1]★ Martin Bureau,[1,2] Leo Blitz,[3] Timothy A. Davis [4] Kyoko Onishi,[5] Mark Smith [1] Eve North [3] and Satoru Iguchi [6,7]

[1]*Sub-department of Astrophysics, Department of Physics, University of Oxford, Keble Road, Oxford OX1 3RH, UK*
[2]*Yonsei Frontier Lab and Department of Astronomy, Yonsei University, 50 Yonsei-ro, Seodaemun-gu, Seoul 03722, Republic of Korea*
[3]*Department of Astronomy and Radio Astronomy Laboratory, University of California, Berkeley, CA 94720, USA*
[4]*School of Physics & Astronomy, Cardiff University, Queens Buildings, The Parade, Cardiff CF24 3AA, UK*
[5]*Research Center for Space and Cosmic Evolution, Ehime University, Matsuyama, Ehime 790-8577, Japan*
[6]*Department of Astronomical Science, SOKENDAI (The Graduate University of Advanced Studies), Mitaka, Tokyo 181-8588, Japan*
[7]*National Astronomical Observatory of Japan, National Institutes of Natural Sciences, Mitaka, Tokyo 181-8588, Japan*

Accepted 2021 May 14. Received 2021 May 1; in original form 2019 October 22

ABSTRACT

We present high spatial resolution (≈12 pc) Atacama Large Millimeter/submillimeter Array ^{12}CO(J = 3–2) observations of the nearby lenticular galaxy NGC 4429. We identify 217 giant molecular clouds within the 450 pc radius molecular gas disc. The clouds generally have smaller sizes and masses but higher surface densities and observed linewidths than those of Milky Way disc clouds. An unusually steep size–linewidth relation ($\sigma \propto R_{\rm c}^{0.8}$) and large cloud internal velocity gradients (0.05–0.91 km s^{-1} pc^{-1}) and observed virial parameters ($\langle\alpha_{\rm obs,vir}\rangle \approx 4.0$) are found, which appear due to internal rotation driven by the background galactic gravitational potential. Removing this rotation, an internal virial equilibrium appears to be established between the self-gravitational ($U_{\rm sg}$) and turbulent kinetic ($E_{\rm turb}$) energies of each cloud, i.e. $\langle\alpha_{\rm sg,vir} \equiv \frac{2E_{\rm turb}}{|U_{\rm sg}|}\rangle \approx 1.3$. However, to properly account for both self and external gravity (shear and tidal forces), we formulate a modified virial theorem and define an effective virial parameter $\alpha_{\rm eff,vir} \equiv \alpha_{\rm sg,vir} + \frac{E_{\rm ext}}{|U_{\rm sg}|}$ (and associated effective velocity dispersion). The NGC 4429 clouds then appear to be in a critical state in which the self-gravitational energy and the contribution of external gravity to the cloud's energy budget ($E_{\rm ext}$) are approximately equal, i.e. $\frac{E_{\rm ext}}{|U_{\rm sg}|} \approx 1$. As such, $\langle\alpha_{\rm eff,vir}\rangle \approx 2.2$ and most clouds are not virialized but remain marginally gravitationally bound. We show this is consistent with the clouds having sizes similar to their tidal radii and being generally radially elongated. External gravity is thus as important as self-gravity to regulate the clouds of NGC 4429.

Key words: ISM: clouds – galaxies: elliptical and lenticular, cD – galaxies: individual: NGC 4429 – galaxies: ISM – galaxies: nuclei – submillimetre: ISM.

1 INTRODUCTION

It is well known that giant molecular clouds (GMCs) are the major gas reservoirs for star formation (SF) and the sites where essentially all stars are born. Understanding the properties of GMCs is thus key to unravelling the interplay between gas and stars within galaxies. Early GMC studies were restricted to our own Milky Way (MW) and the late-type galaxies (LTGs) in our Galactic neighbourhood (e.g. Engargiola et al. 2003; Rosolowsky 2005, 2007; Rosolowsky et al. 2007; Gratier et al. 2012; Colombo et al. 2014; Wu, Sakamoto & Pan 2017; Faesi, Lada & Forbrich 2018), where GMCs have relatively uniform properties and generally follow the so-called Larson relations (between size, velocity dispersion, and luminosity; e.g. Blitz et al. 2007; Bolatto et al. 2008). However, more recent studies of other local galaxies have raised doubts on the universality of cloud properties. The cloud properties in some LTGs (such as M51 and NGC 253) vary with galactic environment and do not universally obey the usual scaling relations (e.g. Hughes et al. 2013; Leroy et al. 2015; Schruba, Kruijssen & Leroy 2019). The first study of individual GMCs in an early-type galaxy (ETG; NGC 4526) has also clearly shown that the clouds in that galaxy do not follow the usual size–linewidth correlation and tend to be more luminous, denser and to have larger velocity dispersions than the GMCs in the MW and other Local Group galaxies (Utomo et al. 2015). The differences in NGC 4526 may be due to a higher interstellar radiation field (and/or cloud extinctions), a different external pressure relative to each cloud's self-gravity, and/or different galactic dynamics. GMCs in ETGs seem to have shorter orbital periods and be subjected to stronger shear/tidal forces, analogous to the highly dynamic environment in the MW central molecular zone (CMZ; e.g. Dale, Kruijssen & Longmore 2019; Henshaw et al. 2019; Kruijssen et al. 2019). Although we are entering an era of large surveys of GMC populations (e.g. Sun et al. 2018), current samples of ETGs are still very limited. More studies of GMCs in varied LTGs and ETGs are thus required to provide a comprehensive census of GMC properties across different galaxy environments.

A model introduced by Meidt et al. (2018) suggests that gas motions at the cloud scale combine the effects of gas self-gravity

★ E-mail: ljliu.astro@gmail.com

and the gas response to the forces exerted by the background host galaxy. In the ETG NGC 4526, the gas motions at cloud scales appear to be driven by the galactic potential. The measured linewidths of the GMCs are much larger than their virial linewidths (the linewidths predicted by assuming the clouds' virial masses are equal to their gaseous masses), an effect that appears to be due to dominant gas motions associated with the background galactic potential. Cloud-scale velocity gradients aligned with the large-scale velocity field indeed suggest a dominance of rotational motions due to the galactic potential (Utomo et al. 2015). It is thus important to investigate whether cloud-scale gas motions are generally dominated by motions due to self-gravity (generally random) or motions due to the galactic potential (generally circular), as this has implications for the observed size–linewidth relation, the virial parameter, cloud morphologies, and the processes governing SF (Meidt et al. 2018).

The dynamical state of a molecular cloud provides important insights into its evolution. It also plays an important role to determine its ability to form stars and stellar clusters (e.g. Hennebelle & Chabrier 2013; Padoan et al. 2017). In most virial balance analyses of molecular clouds, the gravitational term entering the virial theorem includes only the cloud's own self-gravitational energy. However, in some galactic environments (e.g. in galactic nuclei), the external (i.e. galactic) gravitational potential could also play an important role to regulate the cloud dynamics (e.g. Rosolowsky & Blitz 2005; Thilliez et al. 2014; Yusef-Zadeh et al. 2016). To analyse the virial balance of GMCs in such environments, one thus needs to add another gravitational term related to the background gravitational field (e.g. Ballesteros-Paredes et al. 2009; Chen, Amaro-Seoane & Cuadra 2016).

The net effect of the external gravitational potential on the dynamics of GMCs should, however, also include an additional kinetic energy term related to the gas motions driven by the galactic potential, as they provide another source of support against the cloud's self-gravity. In this paper, we therefore revisit the virial theorem by adding two crucial terms that take into account the background galactic gravitational potential: an external gravitational energy term and a kinetic energy term associated with the gas motions due to galactic potential. Although an extended virial theorem including a background tidal field has been formulated before (see e.g. Chen et al. 2016), our resulting virial equation contains new terms that were previously missing and is thus more general.

Early studies of GMCs suggested they are long-lived, quasi-equilibrium entities, isolated from their interstellar environment (e.g. Solomon et al. 1987; Elmegreen 1989; Blitz 1993). However, recent findings that the properties of GMCs vary with galactic environment imply that the clouds are not decoupled from their surroundings (e.g. Hughes et al. 2013; Colombo et al. 2014; Faesi et al. 2018). The main physical factors determining cloud properties include (1) the interstellar radiation field (e.g. McKee 1989), (2) large-scale dynamics (e.g. galactic tides and shear due to differential galactic rotation; Dib et al. 2012; Meidt et al. 2015; Melchior & Combes 2017), (3) interstellar gas pressure (e.g. Heyer et al. 2009; Hughes et al. 2013; Meidt 2016), and (4) the large-scale atomic gas distribution and H I column density (e.g. Engargiola et al. 2003; Blitz et al. 2007; Rosolowsky et al. 2007). In this work, we will focus on the roles of galactic tide/shear to regulate the properties of GMCs. One of our main purposes is indeed to quantitatively investigate the effects of galactic tidal and shear forces on the physical properties and dynamical states of the clouds.

We note an important conceptual point. We will not assume here that the clouds are in dynamical equilibrium, to then infer the clouds' gravitational motions due to the external (i.e. galactic) potential. Instead, we will attempt to directly estimate the clouds' gravitational motions due to the external potential, to then infer whether the clouds are indeed in dynamical equilibrium or not. The question of whether GMCs are in dynamical equilibrium (and thus long-lived) or out of equilibrium (and thus transient) has remained unanswered for decades. We thus believe this approach is not only well justified and worthwhile, but ultimately desirable.

The mm-Wave Interferometric Survey of Dark Object Masses (WISDOM) aims to use the high angular resolution of the Atacama Large Millimeter/submillimeter Array (ALMA) to study (1) the masses and properties of the supermassive black holes (SMBHs) lurking at the centres of galaxies (e.g. Davis et al. 2017, 2018; Onishi et al. 2017; North et al. 2019; Smith et al. 2019; Smith et al. 2021a,b) and (2) the physical properties and dynamics of GMCs in the central parts of the same galaxies. As part of WISDOM, we analyse here the properties and dynamics of individual GMCs in the bulge of NGC 4429, an SA0-type galaxy located in the centre of the Virgo cluster. This paper is the first of a series studying the GMCs in WISDOM galaxies, and it introduces many of the methods and tools we will use to identify GMCs and analyse their properties and dynamics. The paper is structured as follows. In Section 2, we describe the data and the methodology used to identify GMCs in NGC 4429. We use a modified version of the code `CPROPSTOO`, which is more robust and efficient at identifying clouds in complex and crowded environments. The cloud properties, their probability distribution functions, and their mass distribution functions are reported in Section 3. Our analysis of the kinematics of individual GMCs is presented in Section 4. We investigate the dynamical states of the GMCs utilizing our modified virial theorem (MVT; taking into account the background galactic gravitational potential) in Section 5. The shear motions within clouds, the effects of self-gravity, and the cloud morphologies are discussed in Section 6. We conclude briefly in Section 7.

2 DATA AND CLOUD IDENTIFICATION

2.1 Target

NGC 4429 is a lenticular galaxy located in the centre of the Virgo cluster, with a bar and stellar inner ring morphology (Alatalo et al. 2013). It contains a nuclear dust disc visible in extinction against the stellar continuum in *Hubble Space Telescope* (*HST*) imaging (Fig. 1 and Davis et al. 2018). NGC 4429 has a total stellar mass of $\approx 1.5 \times 10^{11}\,\mathrm{M}_{\odot}$, a luminosity-weighted stellar velocity dispersion within one effective radius $\sigma_{\mathrm{e}} = 177\,\mathrm{km\,s^{-1}}$ (Cappellari et al. 2013),

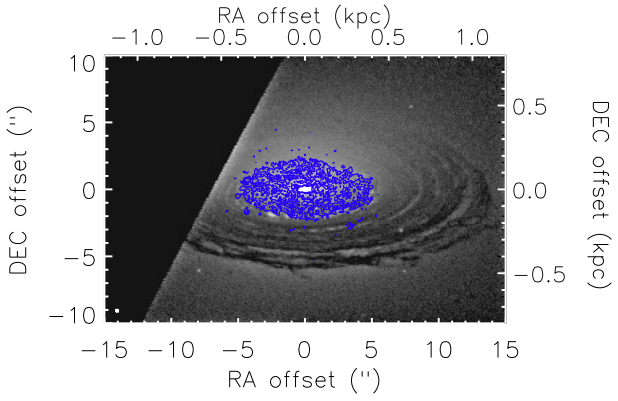

Figure 1. ^{12}CO(3−2) molecular gas distribution of NGC 4429 from our ALMA observations (the blue contours; Davis et al. 2018), overlaid on a *HST* Wide-Field Planetary Camera 2 (WFPC2) *F606W* image of a 2.8 × 2.8 kpc^2 region around its nucleus.

and is a fast rotator (specific angular momentum within one effective radius $\lambda_{R_e} = 0.4$; Emsellem et al. 2011).

The total molecular gas mass of NGC 4429 detected via ^{12}CO(1−0) single-dish observations is $(1.1 \pm 0.08) \times 10^8\,M_\odot$ (Young et al. 2011). The ^{12}CO(1−0) Combined Array for Research in Millimeter-wave Astronomy interferometric map shows the molecular gas is co-spatial with the nuclear dust disc and regularly rotates in the galaxy mid-plane (Davis et al. 2011, 2013, 2018), with an inclination angle of 68° (Davis et al. 2011; Alatalo et al. 2013). The ^{12}CO(3−2) distribution is more compact than that of ^{12}CO(1−0), the ^{12}CO(3−2) gas being present only in the inner parts of the nuclear dust disc visible in *HST* images (see Fig. 1). The star formation rate within this molecular gas disc has been estimated at $0.1\,M_\odot\,yr^{-1}$ using mid-infrared and far-ultraviolet emission (Davis 2014). The spatially unresolved (sub-arcsecond) radio continuum emission from the central regions of NGC 4429 implies the presence of a low-luminosity active galactic nucleus (Nyland et al. 2016). The kinematics of the central CO gas, as probed by the same data set as used here, imply the presence of a $(1.5 \pm 0.1) \times 10^8\,M_\odot$ SMBH (Davis et al. 2018). Throughout this paper, we assume a distance D of 16.5 ± 1.6 Mpc for NGC 4429 (Cappellari et al. 2011). One arcsecond then corresponds to a physical scale of ≈80 pc.

2.2 Data

NGC 4429 was observed in the ^{12}CO(3−2) line (345 GHz) using ALMA as part of the WISDOM project. The data were calibrated and reduced in a standard manner (Davis et al. 2018), and the final ^{12}CO(3–2) data cube we adopt has a synthesized beam of 0.18 arcsec × 0.14 arcsec (14 × 11 pc^2) at a position angle of 311° and a channel width of 2 km s^{-1}. It covers a region of 17.5 arcsec × 17.5 arcsec (1400 × 1400 pc^2), thus comprising the entire nuclear dust and molecular gas disc. Pixels of 0.05 arcsec were chosen as a compromise between spatial sampling and cube size, resulting in approximately 3.5 × 2.8 pixels^2 across the synthesized beam (Davis et al. 2018). Our spatial and spectral resolutions allow for reliable estimates of the radii and velocity dispersions of individual GMCs, which have a typical size of ≈50 pc (Blitz 1993) and a typical linewidth of several km s^{-1} (e.g. Solomon et al. 1987). The root-mean-square (RMS) noise in line-free channels of the cube is $\sigma_{\rm rms} = 1.34$ mJy beam^{-1} (≈0.5 K) in 2 km s^{-1} channels. The integrated ^{12}CO(3−2) spectrum of NGC 4429 exhibits the classic double-horn shape of a rotating disc, with a total flux of 75.5 ± 7.6 Jy km s^{-1}.

As shown in Davis et al. (2018), the molecular gas disc of NGC 4429 is flocculent. Our ALMA observations reveal that the CO(3−2) gas surface density does not decrease smoothly to our detection limit, but instead appears to be truncated at an inner radius of 48 ± 3 pc and an outer radius of 406 ± 10 pc (Davis et al. 2018). As mentioned above, the ^{12}CO(3−2) disc thus lies only in the inner parts of the nuclear dust disc visible in *HST* images (see Fig. 1), and it has an extent smaller than that of the ^{12}CO(1−0) emission (which extends to the edge of the nuclear dust disc; Davis et al. 2013). As CO(3−2) is excited in denser and warmer gas than CO(1−0; with critical densities of ≈7 × 10^4 and ≈1.4 × 10^3 cm^{-3} and excitation temperatures of ≈15 and 5.5 K, respectively), we are likely to identify a cloud population that is associated with H II regions and thus ongoing SF at the centre of NGC 4429 only. High-resolution observations of lower J CO transitions may be required to conduct a study of the NGC 4429 GMC population over the entire molecular gas disc [if indeed additional clouds exist beyond the CO(3−2) extent probed here].

Continuum 345 GHz emission was also detected in NGC 4429, with a centre of RA (J2000) = 12$^{\rm h}$27$^{\rm m}$26$^{\rm s}$.504 ± 0$^{\rm s}$.013 and Dec. (J2000) = 11°06′27″.57 ± 0″.01 derived by Gaussian fitting. This position is consistent with the optical centre of NGC 4429 (Adelman-McCarthy et al. 2008) and will be used as the centre of the galaxy in this work.

2.3 Cloud identification

We use our own modified version of the CPROPSTOO algorithms (Leroy et al. 2015) to identify cloud structures. CPROPSTOO is an updated version of CPROPS (Rosolowsky & Leroy 2006), one of the cloud identification algorithms most widely used in the literature. The key modifications of CPROPSTOO compared to CPROPS were noted by Leroy et al. (2015): CPROPSTOO (1) deconvolves the beam in two dimensions; (2) employs a larger suite of size and linewidth measures, including measuring the area of and fitting an ellipse at the half maximum flux level (in addition to measuring the second moment); and (3) introduces additional extrapolation (aperture correction) approaches, which essentially assume a Gaussian distribution to extrapolate the ellipse fits. In this work, we have further modified CPROPSTOO, to make it more robust when decomposing clouds in complex and crowded environments.

The cloud identification algorithm first calculates a spatially varying estimate of the noise in the data cube, and then uses the noise cube generated to create a 3D mask of bright emission. The mask initially includes only pixels where two adjacent channels (at the same position) both have intensities above $3\,\sigma_{\rm rms}$. It is then expanded to include all neighbouring emission above a lower threshold – two adjacent channels above $2\,\sigma_{\rm rms}$. The regions thus identified are referred to as 'islands'. If an island has a projected area of less than two synthesized beams, it is assumed to be a noise peak and is removed from the mask. The resulting mask contains ≈ 60 per cent of the integrated flux of the galaxy, consistent with the fractions yielded by CPROPS in other studies of extragalactic clouds (50–70 per cent; Wong et al. 2011, 2019; Donovan Meyer et al. 2013; Hughes et al. 2013; Colombo et al. 2014; Leroy et al. 2015; Pan & Kuno 2017; Faesi et al. 2018; Miura et al. 2018; Imara & Faesi 2019). We checked the stringency of the mask by applying the same criteria to the inverted data set (scaled by −1) and found no false positive, so the masking criteria are likely robust.

Once regions of significant emission (i.e. islands) have been identified, these islands are further decomposed into individual 'cloud' structures. Clouds are identified as local maxima within a moving 3D box of area 3 × 3 spaxels^2 (≈12 × 12 pc^2) and velocity width of three channels (6 km s^{-1}). In our modified version of CPROPSTOO, we add another criterion to find local maxima, checking whether the (3 × 3 × 3 pixels^3) box centred on a local maximum also represents a local maximum on a larger scale, as suggested by Yang & Ahuja (2014). This is to eliminate the impact of noisy pixels or outliers, as a noise peak can easily become a local maximum within a single box, but much less so on a larger scale. We thus consider a (3 × 3 × 3 pixels^3) box centred on each local maximum, and require the sum of the flux densities in that box to be larger than that in all eight spatially adjacent (3 × 3 × 3 pixels^3) boxes. The detection of local maxima in this way is much more robust and efficient.

For each local maximum, the original CPROPSTOO algorithm requires all emission uniquely associated with that maximum (i.e. all emission within the faintest intensity isosurface uniquely associated with that maximum) to have a minimum area (*minarea*), minimum number of pixels (*minpix*), and minimum number of

velocity channels (*minvchan*). It also requires the local maximum's brightness temperature to lie at least $\Delta T_{\rm max}$ above the merger level with any other maximum (i.e. the brightest contour level enclosing another local maximum). However, this decomposition algorithm often leads to cloud size and velocity dispersion distributions that peak around the chosen *minarea*, *minpix*, and *minvchan*. This is a well-known bias that reflects the hierarchical structure of the ISM from parsec to kiloparsec scales (e.g. Verschuur 1993; Hughes et al. 2013; Leroy et al. 2016). It becomes especially problematic for complex and crowded environments where the emission has low contrast and extends over a range of scales (e.g. the centre of M51; Hughes et al. 2013; Colombo et al. 2014). Small *minarea* and *minpix* tend to identify the substructures of a cloud (overdecompositon), whereas large *minarea* and *minpix* tend to miss out small structures (underdecomposition).

To remove this bias and identify cloud structures across multiple scales, we modified CPROPSTOO by setting each of *minarea* and *minpix* to a range of values rather than a single value. In our work, we assign *minarea* a range of 100–10 spaxels (the synthesized beam area) with a step of 5 spaxels (half the beam area), similarly in pixels for *minpix*. We start by searching for the largest cloud structures using the largest *minarea* (100 spaxels) and *minpix* (100 pixels), and then repeat the search process to identify increasingly small clouds in the volume of the cube not yet assigned to any cloud. We use a *minarea* (respectively *minpix*) 5 spaxels (respectively 5 pixels) smaller than the previous one at each step, until all the cloud structures larger than the beam size (10 spaxels) are identified. As long as *minarea* and *minpix* cover large ranges, the final results hardly depend on the specified ranges. We are therefore able to remove two free parameters in the algorithm, making our results less arbitrary and more robust. A schematic of our modified CPROPSTOO technique is shown in Fig. 2 for a 1D line profile.

The main concern about our newly developed approach, however, is that we may identify large clouds while ignoring potentially significant substructures. To solve this problem, we introduce a new parameter, *convexity*, inspired by an analogous quantity in studies of biological structures (Lin et al. 2007), which describes how significant the substructure of a cloud is. The parameter *convexity* is defined as the ratio of the volume of the cloud (i.e. the volume of its 3D intensity distribution) to the volume of the smallest convex hull encompassing all of its flux (i.e. the volume of the smallest convex envelope enclosing all of the cloud's 3D intensity distribution; see the top right-hand panel of Fig. 2, for example, with a 1D line profile, i.e. a 2D intensity distribution). The *convexity* of a cloud should thus be close to 1 if the cloud has only one intensity peak and no substructure, and be less than 1 if the cloud has some substructures. The lower the value of *convexity*, the more significant the substructure of a cloud. Our modified CPROPSTOO code requires all clouds to have a minimum *convexity* (*minconvexity*). Typical useful values are 0.5–0.7, as determined by visual inspection, to ensure clouds are not overdecomposed or underdecomposed. In this work, we set *minconvexity* to 0.55. Overall, our new refinements allows CPROPSTOO to identify structures over multiple scales, with less arbitrariness than previously.

We set the parameters *minvchan* and $\Delta T_{\rm max}$ based on physical priors described by Rosolowsky & Leroy (2006), which suggest a cloud has a minimum velocity dispersion $\Delta V_{\rm max} = 2\,{\rm km\,s^{-1}}$ ($minvchan = 2\sqrt{2\ln 2}\,\Delta V_{\rm max} \approx 4$ km s^{-1}) and $\Delta T_{\rm max} = 1$ K, motivated by the properties of Galactic GMCs. A factor of $2\sqrt{2\ln 2}$ is applied to $\Delta V_{\rm max}$ to convert the velocity dispersion to a full width at half-maximum. We set the parameters in physical units (km s^{-1} and K) rather than data units (channel, $\sigma_{\rm rms}$) to reduce possible biases when comparing cloud properties from different observations. Our excellent spectral resolution (channel width of $2\,{\rm km\,s^{-1}}$) and sensitivity ($\sigma_{\rm rms} \approx 0.5$ K) allow us to reach and thus use those physical parameters.

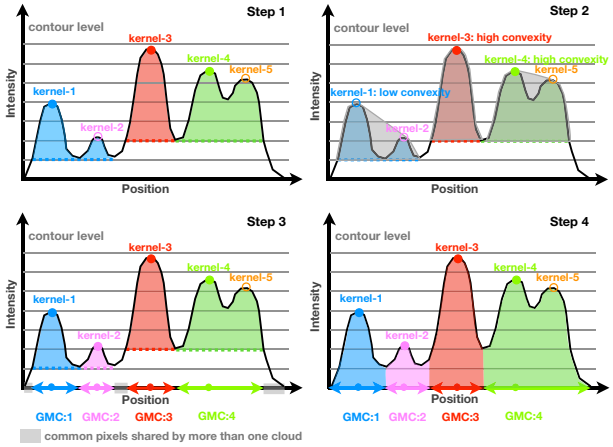

Figure 2. Schematic diagram of the cloud identification process using our modified CPROPSTOO algorithm. Each panel shows a different step in the decomposition of a 1D line profile with five distinct kernels, each kernel corresponding to a local maximum and being identified by a different colour. The circles in matching colours indicate the kernels that are preserved or selected (the solid circles) and rejected (the open circles) at each step. The grey horizontal lines indicate characteristic brightness levels through the data. Each coloured dotted line indicates the unique level of the kernel in matching colour (i.e. the faintest level that is uniquely associated with that kernel), while each coloured region shows the emission uniquely associated with that kernel. **Step 1:** removal of kernels that do not meet the selection criteria given by $\Delta T_{\rm max}$, *minvchan*, and *minpix*/*minarea* (here kernels 2 and 5). **Step 2:** removal of kernels that do not meet the selection criterion given by *minconvexity* (here kernel 1). The *convexity* parameter is defined as the ratio of the volume (or area in this 1D example) of the cloud (i.e. the coloured region of each kernel in matching colour) to the volume (or area) of the smallest convex hull encompassing the cloud (i.e. the associated grey regions). Only kernels 3 and 4 are preserved in this step. **Step 3:** Repeat of steps 1 and 2 adopting increasingly smaller *minpix* and *minarea* (here kernels 1 and 2 are reselected due to the lower cloud size threshold; both have sufficient *convexity*). **Step 4:** assigment of remaining emission (e.g. grey regions in the bottom left-hand panel) to the preserved kernels (using a friends-of-friends algorithm ensuring any pair of pixels in a kernel is connected by a continuous path).

According to our algorithm, each surviving local maximum corresponds to a cloud. CPROPSTOO assigns the emission that is uniquely associated with each local maximum (i.e. the emission within the faintest intensity isosurface uniquely associated with that maximum) to that cloud. The remaining emission shared among clouds is then assigned to the 'nearest' local maximum (i.e. the local maximum with the shortest path through the data cube from a given pixel). In our work, however, we apply a 'friends-of-friends' algorithm to assign all remaining emission, as for the CLUMPFIND algorithm (Williams, de Geus & Blitz 1994) and the original CPROPS code (Rosolowsky & Leroy 2006). This friends-of-friends paradigm connects pixels according to the brightnesses of neighbouring pixels, without assuming a particular shape for the objects to decompose (Rosolowsky & Leroy 2006). This method conserves flux, so that all the flux within the island regions is assigned to a particular cloud (Tasker & Tan 2009). As each pair of pixels in a cloud can then be connected by a continuous path through that cloud, we avoid assigning disconnected pixels to the same cloud.

The resulting sample of GMCs in NGC 4429 contains 217 GMCs, 141 of which are spatially resolved, shown in Fig. 3. The majority

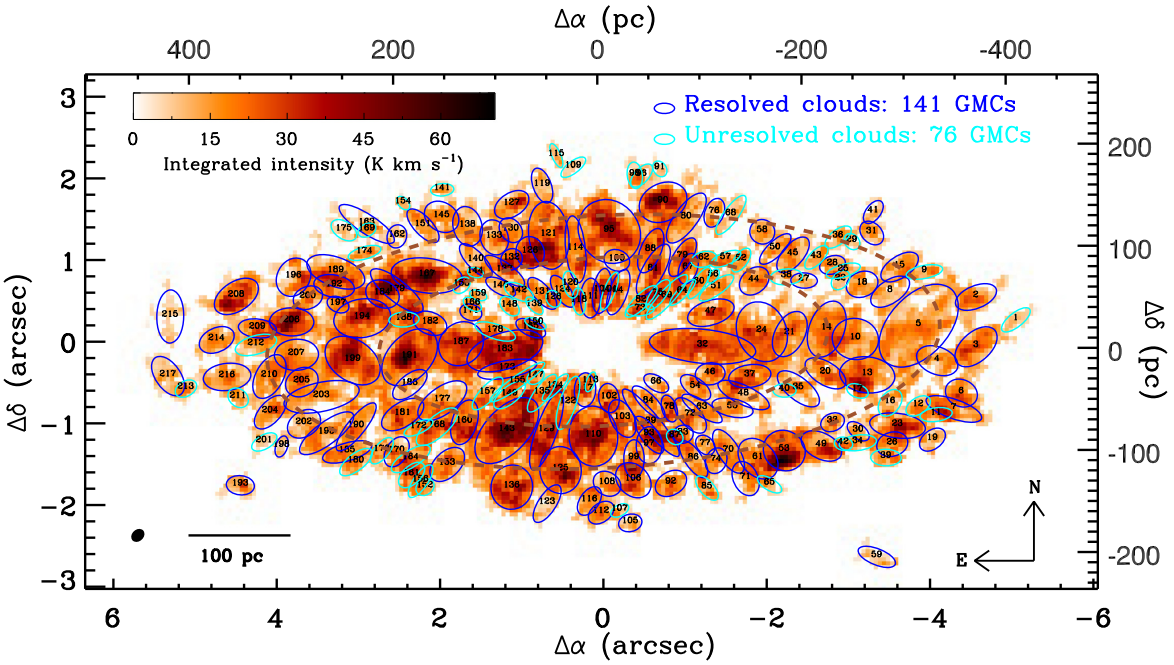

Figure 3. Molecular gas distribution of NGC 4429 with GMCs identified. The integrated intensity map is shown (colour scale), blanking out non-signal areas using the mask generated by CPROPSTOO. The mask covers pixels with connected emission above 2 $\sigma_{\rm rms}$ and at least two adjacent channels above 3 $\sigma_{\rm rms}$, where $\sigma_{\rm rms}$ is the RMS noise in the cube. The ellipses displayed, each corresponding to one labelled cloud, have been extrapolated to the limit of perfect sensitivity but have not been corrected for the finite spatial resolution. The dark blue (resp. cyan) ellipses indicate spatially resolved (resp. unresolved) clouds. The two brown-dashed ellipses at galactocentric distances of 220 and 330 pc define the three regions (inner, intermediate, and outer) discussed in the text. The synthesized beam (0.18 arcsec × 0.14 arcsec or 14 × 11 pc^2) is shown in the bottom left-hand corner along with a scale bar.

of the resolved clouds have a single-peaked Gaussian-like spatially integrated line profile, although a few do reveal a double-peaked line profile possibly indicating significant rotation. Most line profiles are symmetric but a few are asymmetric, with significant skewness (blue or red wing). The clouds identified with our new refinements are 15 per cent fewer (217 versus 254 clouds), 18 per cent larger (median cloud size ≈13 versus ≈11 pc), 18 per cent more massive (median gaseous mass ≈2.0 × 10^4 versus 1.7 × 10^4 M$_\odot$), and have velocity dispersions 30 per cent larger (median velocity dispersion 5.2 versus 4.0 km s^{-1}) than those derived using the original CPROPSTOO code. They also span a larger range of sizes. A Gaussian fit to the size distribution yields a mean of 16 ± 0.5 pc and a standard deviation of ≈6 pc for our spatially resolved clouds (see Section 3.3), but 14 ± 0.5 and ≈3.5 pc, respectively, for those identified using the original CPROPSTOO. The resolved clouds identified here also seem to have more regular morphologies, with a mean ⟨*convexity*⟩ = 0.57 (*convexity* > 0.55 by construction) compared to ⟨*convexity*⟩ ≈ 0.45 (and ≈ 54 per cent of resolved clouds with *convexity* < 0.55) for CPROPSTOO-identified clouds. This confirms that our approach and modified CPROPSTOO code have great potential to identify clouds over large spatial scales in crowded and complex environments (e.g. galactic centres and spiral arms).

3 CLOUD PROPERTIES

3.1 Definition of GMC properties

Once all the pixels of every cloud have been identified, we calculate the physical properties of the clouds by following the standard CPROPSTOO/CPROPS definitions (Rosolowsky & Leroy 2006). The CPROPSTOO algorithm applies moment methods to derive the size, linewidth, and flux of a cloud from its distribution within a position–position–velocity data cube. One advantage of CPROPSTOO over other GMC identification algorithms is that it attempts to correct the measured cloud properties for the finite sensitivity and instrumental resolution (Rosolowsky & Leroy 2006). To reduce the sensitivity bias, the algorithm measures the size, velocity width, and luminosity as a function of the boundary intensity isosurface ($T_{\rm edge}$) and extrapolates them to the case of infinite signal-to-noise ratio (*S*/*N*; i.e. $T_{\rm edge} = 0$ K). The size and linewidth are extrapolated linearly, while the luminosity is extrapolated quadratically. To correct for the resolution bias, CPROPSTOO 'deconvolves' the synthesized beam size from the measured extrapolated cloud size in two dimensions. Rosolowsky & Leroy (2006) argued that moment measurements combined with beam deconvolution and extrapolation represent a robust way to compare heterogeneous observations of molecular clouds.

3.1.1 Cloud centre

The central position ($x_{\rm c}$, $y_{\rm c}$) and velocity ($v_{\rm c}$) of each cloud are obtained directly from the intensity-weighted first spatial and velocity moment:

$$\begin{cases} x_{\rm c} \equiv \frac{\sum_i^{\rm cloud} T_i x_i}{\sum_i^{\rm cloud} T_i}, \\ y_{\rm c} \equiv \frac{\sum_i^{\rm cloud} T_i y_i}{\sum_i^{\rm cloud} T_i}, \\ v_{\rm c} \equiv \frac{\sum_i^{\rm cloud} T_i v_i}{\sum_i^{\rm cloud} T_i}, \end{cases} \quad (1)$$

where (x_i, y_i) is the position of a given pixel, v_i its velocity, and T_i its flux (brightness temperature), and the sums are over all pixels *i* of each cloud.

3.1.2 Cloud size

The radius R_c of each cloud is calculated as the geometric mean of the second spatial moment of the intensity distribution along the major and the minor axis:

$$R_c \equiv \eta\sqrt{\sigma_{maj,dc}\ \sigma_{min,dc}} = 1.91\sqrt{\sigma_{maj,dc}\ \sigma_{min,dc}}, \quad (2)$$

where $\sigma_{maj,dc}$ and $\sigma_{min,dc}$ are the deconvolved RMS spatial extent along the major and the minor axis, respectively, extrapolated to the $T_{edge} = 0$ K isosurface, and η is a factor relating the 1D RMS extent to the radius of a cloud. While η formally depends on the shape and density profile of the cloud, we follow Solomon et al. (1987) and common practice and adopt $\eta = 1.91$ whenever we need to evaluate expressions containing R_c. The major and minor axes are thus defined as the principal axes of the moment of inertia tensor of the cloud (see equation 1 in Rosolowsky & Leroy 2006).

3.1.3 Cloud velocity dispersion

The observed (i.e. 1D) linewidth or velocity dispersion $\sigma_{obs,los}$ of each cloud is measured from the second moment of the intensity distribution along the velocity axis, extrapolated to $T_{edge} = 0$ K. To account for the potential bias towards a higher velocity dispersion due to the finite spectral resolution, we perform a deconvolution as suggested by Rosolowsky & Leroy (2006):

$$\sigma_{obs,los} \equiv \sqrt{\sigma_v^2 - \frac{\Delta V_{chan}^2}{2\pi}}, \quad (3)$$

where σ_v is the extrapolated second moment along the velocity axis, ΔV_{chan} is the channel width, and $\frac{\Delta V_{chan}}{\sqrt{2\pi}}$ is the standard deviation of a Gaussian that has an integrated area equal to a spectral channel of width ΔV_{chan}.

The observed velocity dispersion $\sigma_{obs,los}$ includes the effects of turbulent motions, intrinsic rotation of the cloud, and shear motions due to the large-scale kinematics of the galactic disc (such as galactic rotation and streaming motions).

In our work, we introduce another measured velocity dispersion, $\sigma_{gs,los}$, as defined by Utomo et al. (2015), although we adopt the notation of Henshaw et al. (2019). We first calculate the intensity-weighted mean velocity at each line of sight through a cloud ($\bar{v}(x_i, y_i)$), and measure its offset with respect to the mean velocity at the cloud centre ($\bar{v}(x_0, y_0)$). We assume that this offset ($\bar{v}(x_i, y_j) - \bar{v}(x_0, y_0)$) is produced by both intrinsic motions within the cloud and/or large-scale galactic disc motions, and thereby shift the velocities at each line of sight to match their mean velocity to that of the cloud centre ($\bar{v}(x_0, y_0)$). We then measure the second moment of the shifted emission distribution along the velocity axis and extrapolate it to $T_{edge} = 0$ K. The final derived gradient-subtracted velocity dispersion, $\sigma_{gs,los}$, is also deconvolved for the channel width as above. We thus obtain a measure of the turbulent (random) motions within the cloud only, free of any bulk motion.

3.1.4 Cloud luminosity

The CO(3−2) luminosity of each cloud is given by

$$\frac{L_{CO(3-2)}}{\mathrm{K\ km\ s^{-1}\ pc^2}} = \frac{F_{CO(3-2)}}{\mathrm{K\ km\ s^{-1}\ arcsec^2}} \left(\frac{D}{\mathrm{pc}}\right)^2 \left(\frac{\pi}{180 \times 3600}\right)^2, \quad (4)$$

where $F_{CO(3-2)}$ is the zeroth moment (total flux) of the cloud extrapolated to $T_{edge} = 0$ K using a quadratic extrapolation and D is the distance to NGC 4429.

3.1.5 Cloud gaseous mass

The CO luminosity-based mass of each cloud is obtained from $L_{CO(3-2)}$ using

$$\frac{M_{gas}}{\mathrm{M_\odot}} = 4.4\ \frac{L_{CO}}{\mathrm{K\ km\ s^{-1}\ pc^2}}\ \frac{X_{CO}}{2 \times 10^{20}\ \mathrm{cm^{-2}\ (K\ km\ s^{-1})^{-1}}}, \quad (5)$$

where L_{CO} is the cloud's CO(1−0) luminosity (see equation 4 above) and X_{CO} is the assumed CO-to-H_2 conversion factor. The CO(3−2)/CO(1−0) intensity ratio was measured to be 1.06 ± 0.15 (in beam temperature units) overall in NGC 4429 (Davis et al. 2018), and we assume that value for all the clouds here. We further adopt a standard Galactic conversion factor $X_{CO} = 2.3 \times 10^{20}$ cm^{-2} (K km s^{-1})$^{-1}$ (including the mass contribution from helium; Strong et al. 1988; Bolatto, Wolfire & Leroy 2013), commonly used in previous extragalactic studies (e.g. Hughes et al. 2013; Colombo et al. 2014; Utomo et al. 2015; Sun et al. 2018), although it has been suggested that this conversion factor depends on the environment of each molecular cloud, e.g. metallicity and radiation field (see Bolatto et al. 2013 for a review). The final gaseous mass of each cloud is thus obtained from

$$\frac{M_{gas}}{\mathrm{M_\odot}} = 4.7\ \frac{L_{CO(3-2)}}{\mathrm{K\ km\ s^{-1}\ pc^2}}. \quad (6)$$

3.1.6 Cloud virial mass

The virial (i.e. dynamical) mass of each cloud is calculated with the formula

$$M_{vir} = \frac{\sigma^2 R_c}{b_s G} = \frac{5\sigma^2 R_c}{G} \quad (7)$$

(MacLaren, Richardson & Wolfendale 1988), where G is the gravitational constant, σ the observed (i.e. 1D) cloud velocity dispersion, R_c the cloud radius (see equation 2), and b_s is a geometrical factor that quantifies the effects of inhomogeneities and/or non-sphericity of the cloud mass distribution on its self-gravitational energy. For a cloud in which the isodensity contours are homoeoidal ellipsoids, $b_s = b_{s_1} b_{s_2}$, where b_{s_1} quantifies the effects of the inhomogeneities and b_{s_2} those of the ellipticity (see Appendix A for more details on b_{s_1} and b_{s_2}). We adopt $b_s = \frac{1}{5}$ for a spherical homogeneous (i.e. constant density) cloud whenever we need to evaluate M_{vir}. The virial mass obtained from equation (7) assumes that each cloud is spherical and virialized (with isotropic velocity dispersions), with no magnetic support or pressure confinement. We note that, to investigate the dynamical state of each cloud in the presence of strong tidal/shear forces, in the sections that follow we will define different M_{vir} using velocity dispersions σ calculated in different ways. These will be clearly labelled when used to avoid confusion.

3.1.7 Cloud distance from the centre

The deprojected distance (R_{gal}) of a cloud from the centre of the galaxy (RA (J2000) = $12^h27^m26\overset{s}{.}504 \pm 0\overset{s}{.}013$ and Dec. (J2000) = $11°06'27\overset{''}{.}57 \pm 0\overset{''}{.}01$ is calculated assuming the clouds are located in an infinitely thin molecular gas disc with a position angle of 93° and an inclination angle of 68° (i.e. an axial ratio of 0.37; see Davis et al. 2018).

3.1.8 Uncertainties

The uncertainties of our measured cloud properties are estimated via a bootstrapping technique. For each cloud, we generate 1000

Table 1. Observed properties of the clouds in NGC 4429.

ID	RA(2000) (h:m:s)	Dec.(2000) (°:′:″)	$V_{\rm LSR}$ (km s^{-1})	$R_{\rm c}$ (pc)	$\sigma_{\rm obs,los}$ (km s^{-1})	$\sigma_{\rm gs,los}$ (km s^{-1})	$L_{\rm CO(3-2)}$ (10^4 K km s^{-1} pc^2)	$M_{\rm gas}$ (10^5 M$_\odot$)	$T_{\rm max}$ (K)	ω (km s^{-1} pc^{-1})	$\phi_{\rm rot}$ (°)	$R_{\rm gal}$ (pc)
1	12:27:26.2	11:06:27.9	853.8	–	1.50 ± 1.06	1.25 ± 1.12	0.92 ± 0.26	0.43 ± 0.12	3.8	–	–	404
2	12:27:26.2	11:06:28.2	864.4	16.69 ± 5.27	4.81 ± 1.45	2.81 ± 1.02	3.01 ± 0.56	1.40 ± 0.26	3.3	0.43 ± 0.14	139 ± 25	372
3	12:27:26.2	11:06:27.6	864.6	23.45 ± 3.63	6.69 ± 1.00	3.79 ± 0.74	4.99 ± 0.71	2.32 ± 0.33	3.8	0.27 ± 0.04	175 ± 14	370
4	12:27:26.2	11:06:27.4	872.4	20.18 ± 4.12	4.47 ± 0.92	2.95 ± 0.85	2.59 ± 0.44	1.21 ± 0.21	3.4	0.23 ± 0.09	290 ± 19	339
5	12:27:26.2	11:06:27.8	875.9	46.89 ± 3.03	5.53 ± 0.54	2.35 ± 0.33	11.49 ± 1.01	5.35 ± 0.47	4.2	0.20 ± 0.01	163 ± 3	309
6	12:27:26.2	11:06:27.0	876.9	17.79 ± 3.15	4.51 ± 0.99	2.86 ± 0.90	2.34 ± 0.50	1.09 ± 0.23	3.4	0.28 ± 0.09	222 ± 24	394
7	12:27:26.2	11:06:26.8	883.7	17.76 ± 4.90	5.10 ± 1.05	2.93 ± 0.80	2.96 ± 0.50	1.38 ± 0.23	3.9	0.13 ± 0.04	149 ± 25	407
8	12:27:26.3	11:06:28.3	887.3	18.99 ± 4.82	3.58 ± 1.18	1.83 ± 1.07	1.50 ± 0.28	0.70 ± 0.13	3.8	0.16 ± 0.10	138 ± 49	296
9	12:27:26.2	11:06:28.5	885.2	–	3.62 ± 1.11	3.08 ± 1.27	1.27 ± 0.30	0.59 ± 0.14	3.7	–	–	345
10	12:27:26.3	11:06:27.7	888.2	29.40 ± 3.14	4.81 ± 0.75	2.97 ± 0.70	4.69 ± 0.59	2.18 ± 0.28	3.8	0.16 ± 0.03	230 ± 13	248
11	12:27:26.2	11:06:26.7	892.8	–	2.84 ± 0.74	2.52 ± 0.81	0.99 ± 0.27	0.46 ± 0.13	4.2	–	–	400
12	12:27:26.2	11:06:26.9	894.8	–	5.49 ± 1.42	3.11 ± 1.24	1.38 ± 0.37	0.64 ± 0.17	3.5	–	–	371
13	12:27:26.3	11:06:27.2	892.9	26.18 ± 2.65	6.34 ± 0.86	3.22 ± 0.58	6.12 ± 0.60	2.85 ± 0.28	4.8	0.33 ± 0.03	213 ± 7	285
14	12:27:26.3	11:06:27.8	898.0	26.25 ± 2.73	5.14 ± 0.62	2.52 ± 0.42	5.33 ± 0.56	2.49 ± 0.26	4.4	0.27 ± 0.02	202 ± 6	219
15	12:27:26.2	11:06:28.6	898.4	14.93 ± 4.44	3.36 ± 0.87	2.46 ± 0.68	2.37 ± 0.52	1.11 ± 0.24	3.5	0.17 ± 0.07	72 ± 39	330
16	12:27:26.3	11:06:26.9	900.3	–	5.08 ± 1.80	2.57 ± 1.55	1.37 ± 0.41	0.64 ± 0.19	2.7	–	–	342
17	12:27:26.3	11:06:27.0	902.0	–	4.76 ± 1.75	4.20 ± 1.95	0.82 ± 0.19	0.38 ± 0.09	3.8	–	–	296
18	12:27:26.3	11:06:28.3	901.2	16.35 ± 3.67	5.70 ± 1.23	2.18 ± 0.81	1.75 ± 0.40	0.81 ± 0.19	3.3	0.52 ± 0.19	148 ± 28	279
19	12:27:26.2	11:06:26.4	906.3	14.16 ± 5.81	6.04 ± 2.54	4.16 ± 2.67	1.48 ± 0.46	0.69 ± 0.21	2.8	0.34 ± 0.92	260 ± 121	438
20	12:27:26.3	11:06:27.3	908.3	20.56 ± 4.42	3.33 ± 0.84	2.51 ± 0.82	2.57 ± 0.50	1.20 ± 0.23	3.6	0.10 ± 0.04	181 ± 55	244
–	–	–	–	–	–	–	–	–	–	–	–	–
217	12:27:26.9	11:06:27.2	1344.3	20.42 ± 3.92	2.23 ± 0.68	1.58 ± 0.89	1.94 ± 0.34	0.90 ± 0.16	3.8	0.01 ± 0.04	85 ± 138	428

Note. Measurements of $M_{\rm gas}$ assume a CO(3−2)/CO(1−0) line ratio of 1.06 ± 0.15 (in beam temperature units; Davis et al. 2018) and a standard Galactic conversion factor $X_{\rm CO} = 2 \times 10^{20}$ cm^{-2} (K km s^{-1})$^{-1}$ (including the mass contribution from helium). All uncertainties are quoted at the $1\,\sigma$ level. As noted in the text, the uncertainty of the adopted distance D to NGC 4429 was not propagated through the tabulated uncertainties of the measured quantities. This is because an error on the distance to NGC 4429 translates to a systematic (rather than random) scaling of some of the measured quantities (no effect on the others), i.e. $R_{\rm c} \propto D$, $L_{\rm CO(3-2)} \propto D^2$, $M_{\rm gas} \propto D^2$, $\omega \propto D^{-1}$, and $R_{\rm gal} \propto D$. Table 1 is available in its entirety in machine-readable form in the electronic edition.

realizations of the data by randomly sampling the initial distribution, with repetition allowed, to reach the same number of cloud pixels. The cloud properties are measured for each sampled structure, and the median absolute deviation is used to estimate the fractional uncertainty of each property. The final uncertainties are scaled by the square root of the number of spaxels per synthesized beam area to account for the fact that not all of the pixels are independent. Our bootstrap approach assumes the boundary of each cloud is fixed, and therefore does not take into account the uncertainties in defining the cloud themselves. Nevertheless, we have compared the uncertainties produced by our bootstrapping method to those derived from other techniques (e.g. Rosolowsky & Leroy 2006; Faesi, Lada & Forbrich 2016), demonstrating that they are similar and thus reliable. We note that the uncertainty of the gradient-subtracted velocity dispersion $\sigma_{\rm gs,los}$ is derived via the same bootstrapping technique, and thus includes the uncertainty of the adopted mean velocity at the cloud centre.

The uncertainty of the adopted distance D to NGC 4429 was not propagated through the uncertainties of the measured quantities. This is because an error on the distance to NGC 4429 translates to a systematic (rather than random) scaling of some of the measured quantities (no effect on the others), i.e. $R_{\rm c} \propto D$, $L_{\rm CO(3-2)} \propto D^2$, $M_{\rm gas} \propto D^2$, $\omega \propto D^{-1}$, and $R_{\rm gal} \propto D$.

3.2 Table of GMC properties

Table 1 lists the positions and properties of the 217 GMCs identified in our work. Around 65 per cent (141/217) of the GMCs identified are resolved spatially, i.e. with a deconvolved diameter larger than or equal to the synthesized beam size. All are resolved spectrally, i.e. with a deconvolved velocity width at least half of one (Hanning smoothed) velocity channel (Donovan Meyer et al. 2013). All masked CO flux has been assigned to a cloud, and the total flux of all clouds ($\approx$43 Jy km s^{-1}) is about 60 per cent of the integrated flux of the galaxy (75 Jy km s^{-1}). The diffuse emission below the adopted threshold of two times the RMS noise is not included in our analysis. As our primary beam covers all the CO emission in NGC 4429, our derived GMC catalogue is complete at ^{12}CO(3−2).

Table 1 lists each cloud's identification number, central position in both RA and Dec., local standard of rest velocity $V_{\rm LSR}$, radius $R_{\rm c}$, observed velocity dispersion $\sigma_{\rm obs,los}$ and gradient-subtracted velocity dispersion $\sigma_{\rm gs,los}$, total CO(3−2) luminosity $L_{\rm CO(3-2)}$, gaseous mass $M_{\rm gas}$, peak intensity $T_{\rm max}$, angular velocity ω and position angle of the rotation axis $\phi_{\rm rot}$ (see Section 4.1), and deprojected distance from the centre of the galaxy $R_{\rm gal}$.

3.3 Probability distribution functions of GMC properties

The number distributions of $R_{\rm c}$, $\log(M_{\rm gas}/{\rm M}_\odot)$, $\sigma_{\rm obs,los}$, and $\log(\Sigma_{\rm gas}/{\rm M}_\odot\,{\rm pc}^{-2})$; where $\Sigma_{\rm gas}$ is the characteristic gaseous mass surface density of each cloud, $\Sigma_{\rm gas} \equiv \frac{M_{\rm gas}}{\pi R_{\rm c}^2}$) for the 141 spatially resolved clouds of NGC 4429 are shown in Fig. 4. We divide the galaxy into three distinct regions (separated by the two brown-dashed ellipses in Fig. 3): inner ($R_{\rm gal} \leq 220$ pc), intermediate ($220 < R_{\rm gal} \leq 330$ pc), and outer ($R_{\rm gal} > 330$ pc) region. In each panel, the black histogram (data) and curve (Gaussian fit) show the full sample, while the blue, green, and red colours show only the clouds in the inner, intermediate, and outer region, respectively. The insets show the median $R_{\rm c}$, $\log(M_{\rm gas}/{\rm M}_\odot)$, $\sigma_{\rm obs,los}$, and $\log(\Sigma_{\rm gas}/{\rm M}_\odot\,{\rm pc}^{-2})$ as functions of the galactocentric distance $R_{\rm gal}$.

The spatially resolved clouds of NGC 4429 have sizes $R_{\rm c}$ ranging from 7 to about 50 pc (see Fig. 4, top left-hand panel). A Gaussian fit

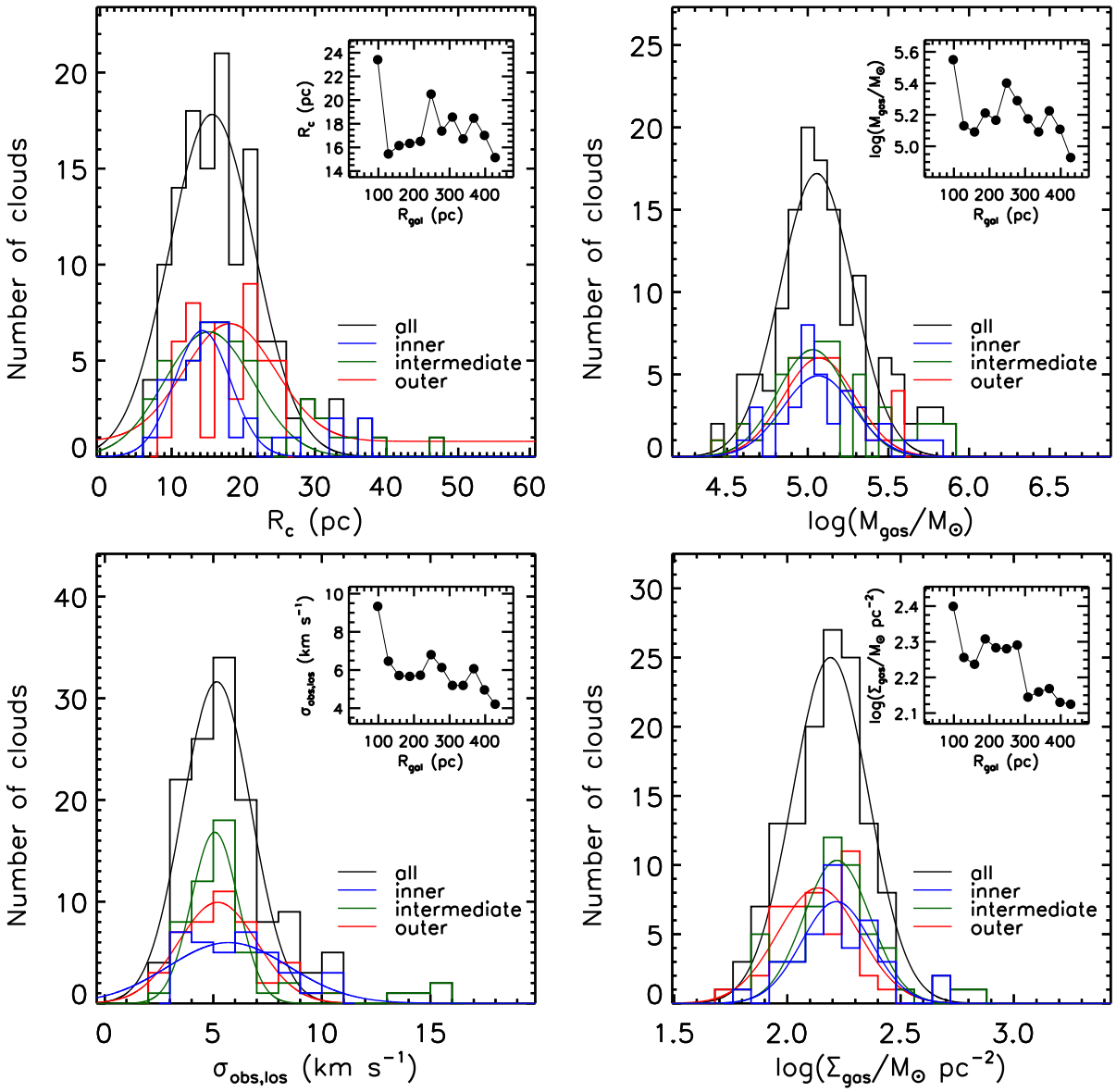

Figure 4. Distributions of R_c, $\log(M_{gas}/M_\odot)$, $\sigma_{obs,los}$, and $\log(\Sigma_{gas}/M_\odot\ pc^{-2})$ with their Gaussian fits for the 141 spatially resolved clouds identified in NGC 4429 (the black histograms), and for only the clouds in the inner (the blue histograms), intermediate (the green histograms), and outer (the red histograms) region of the galaxy, respectively. The insets show the median R_c, $\log(M_{gas}/M_\odot)$, $\sigma_{obs,los}$, and $\log(\Sigma_{gas}/M_\odot\ pc^{-2})$ in elliptical annuli of constant R_{gal} (and equal width $\Delta R_{gal} = 30$ pc).

to the size distribution yields a mean of 16 ± 0.5 pc and a standard deviation of ≈6 pc. The clouds in NGC 4429 appear to have sizes smaller than those of clouds in the MW disc (typical sizes ≈30–50 pc; Miville-Deschênes, Murray & Lee 2017b), Local Group galaxies (typical sizes ≈20–70 pc; Rosolowsky et al. 2003, 2007; Rosolowsky 2007; Hirota et al. 2011), and most LTGs (typical sizes ≈20–200 pc; Donovan Meyer et al. 2012; Hughes et al. 2013; Rebolledo et al. 2015), but slightly larger than those of clouds in the Galactic centre (typical sizes ≈5–15 pc; Oka et al. 2001; Kauffmann et al. 2017) and the ETG NGC 4526 (typical sizes ≈5–30 pc; Utomo et al. 2015). We note, however, that the CO J = 3–2 transition used in our work traces the warm molecular medium (10–50 K) around active SF regions, and has a higher characteristic density than the J = 1−0 transition (≈7×10^4 versus ≈1.4×10^3 cm^{-3}). The CO(3−2) line could therefore potentially trace more compact structures than CO(1−0; Miville-Deschenes, Murray & Lee 2017a; Colombo et al. 2018). The inset in the top left-hand panel presents the median cloud size as a function of galactocentric distance. We note that the three innermost resolved clouds (clouds No. 32, 165, and 183; $R_{gal} \leq 100$ pc), which all lie along the major axis, have exceptionally large masses and/or surface densities. Except for these three innermost resolved clouds, the clouds in the inner region generally have slightly smaller sizes than the clouds at larger radii (i.e. in the intermediate and outer regions). The sizes of the clouds appear to slightly increase with galactocentric distance but drop at the outer edge of the molecular disc ($R_{gal} \gtrsim 375$ pc).

The gaseous masses M_{gas} of the spatially resolved clouds of NGC 4429 range from 2.8×10^4 to 8×10^5 M$_\odot$ (see Fig. 4, top right-hand panel). The median cloud gaseous mass of the sample is ≈1.6×10^5 M$_\odot$. More than one-third (54/141) of the resolved

clouds are light ($M_{\rm gas} \leq 10^5$ M$_\odot$), but they overall contribute only $\approx$ 16 per cent of the total molecular gas mass in clouds. There is no cloud more massive than $M_{\rm gas} = 10^6$ M$_\odot$ in NGC 4429. The clouds in NGC 4429 have gaseous masses slightly smaller than those of clouds in the MW disc ($\approx 10^{4.5}$–$10^{7.0}$ M$_\odot$; Rice et al. 2016), NGC 4826 ($\approx 10^{6.0}$–$10^{7.2}$ M$_\odot$; Rosolowsky & Blitz 2005), NGC 1068 ($\approx 10^{4.2}$–$10^{7.6}$ M$_\odot$; Tosaki et al. 2017), M51 ($\approx 10^{5.0}$–$10^{7.5}$ M$_\odot$; Colombo et al. 2014), NGC 253 ($\approx 10^{6.3}$–$10^{7.8}$ M$_\odot$; Leroy et al. 2015), and the Large Magellanic Cloud (LMC; $\approx 10^{4.2}$–$10^{6.8}$ M$_\odot$; Hughes et al. 2010), but similar to those of clouds in M31 ($\approx 10^4$–10^6 M$_\odot$; Rosolowsky 2007), M33 ($\approx 10^4$–10^6 M$_\odot$; Rosolowsky et al. 2003, 2007), the SMC ($\approx 10^4$–10^6 M$_\odot$; Muller et al. 2010), and the ETG NGC 4526 ($\approx 10^{4.7}$–$10^{6.6}$ M$_\odot$; Utomo et al. 2015). The clouds in the intermediate region tend to be more massive than the clouds in the inner and outer regions (see the inset in the top right-hand panel). The median cloud mass also appears to drop abruptly in the outermost region of the molecular disc ($R_{\rm gal} \gtrsim 375$ pc).

The spatially resolved clouds of NGC 4429 have observed velocity dispersions (linewidths) $\sigma_{\rm obs,los}$ between 2 and 16 km s^{-1} (see Fig. 4, bottom left-hand panel). A Gaussian fit to the velocity dispersion distribution yields a mean of 5.2 $\pm$ 0.2 km s^{-1}. The clouds in NGC 4429 have observed velocity dispersions higher than those of clouds with the same sizes in the MW and Local Group galaxies (where $\sigma_{\rm obs,los}$ is typically 2–3 km s^{-1}; Rosolowsky et al. 2003, 2007; Rosolowsky 2007; Fukui et al. 2008; Muller et al. 2010), but similar to those of the clouds in the ETG NGC 4526 ($\sigma_{\rm obs,los} \approx$ 5–16 km s^{-1}; Utomo et al. 2015). Almost all clouds with high velocity dispersions ($\sigma_{\rm obs,los} \geq 10$ km s^{-1}) are located in the inner and intermediate regions. We find a general trend of slightly decreasing velocity dispersion with galatocentric radius (see the inset in the bottom left-hand panel).

The gaseous mass surface densities $\Sigma_{\rm gas}$ of spatially resolved clouds in NGC 4429 have a range of $\approx$40–650 M$_\odot$ pc^{-2} (see Fig. 4, bottom right-hand panel). A Gaussian fit to the distribution of $\log(\Sigma_{\rm gas}/{\rm M}_\odot\,{\rm pc}^{-2})$ yields a mean of 2.2 $\pm$ 0.17 dex. The clouds in NGC 4429 have an average gaseous mass surface density that is lower than that of the clouds in the ETG NGC 4526 ($\langle\Sigma_{\rm gas}\rangle \approx$ 1000 M$_\odot$ pc^{-2}; Utomo et al. 2015), but is comparable to that of the clouds in M33 and M64 ($\langle\Sigma_{\rm gas}\rangle \approx 100$ M$_\odot$ pc^{-2}; Rosolowsky et al. 2003; Rosolowsky & Blitz 2005) and is larger than that of the clouds in the MW disc and the LMC ($\langle\Sigma_{\rm gas}\rangle \approx 50$ M$_\odot$ pc^{-2}; Heyer et al. 2009; Hughes et al. 2010; Lombardi, Alves & Lada 2010; Miville-Deschênes et al. 2017b). The gaseous mass surface densities of individual clouds in NGC 4429 vary by more than an order of magnitude. We find that the clouds in the inner region tend to have a slightly larger minimum gaseous mass surface density ($\Sigma_{\rm gas} \geq$ 70 M$_\odot$ pc^{-2}) than the clouds in the intermediate ($\Sigma_{\rm gas} \geq 60$ M$_\odot$ pc^{-2}) and outer ($\Sigma_{\rm gas} \geq 40$ M$_\odot$ pc^{-2}) region. The general trend is that the clouds at smaller radii have higher gaseous mass surface densities (see the inset in the bottom right-hand panel).

3.4 GMC mass spectra

The distribution of GMCs by mass is a critical diagnostic of a GMC population and provides important clues to GMC formation and destruction (Rosolowsky 2005; Colombo et al. 2014). We choose the gaseous mass over the viral mass to determine the mass function because gas mass does not require assumptions about the dynamical state of the GMCs and is well defined even for spatially unresolved clouds. We fit the cumulative mass distribution (see Fig. 5) instead of the differential mass distribution, as Rosolowsky (2005) argues

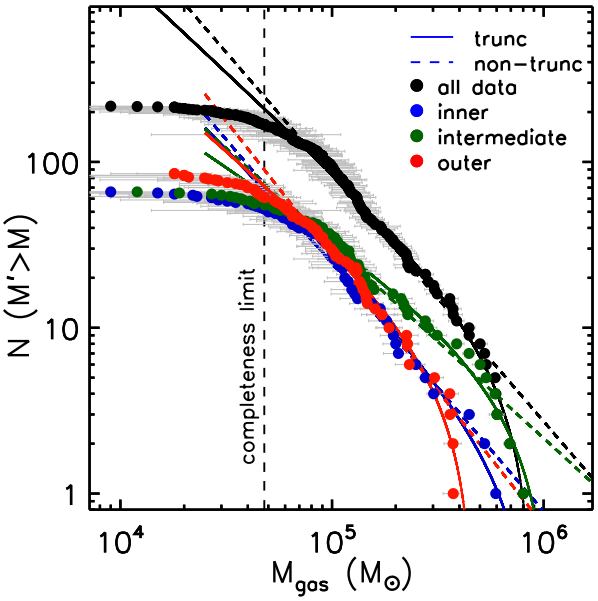

Figure 5. Cumulative gaseous mass distribution of all the clouds of NGC 4429 (the black data points) and only the clouds in the inner (the blue data points), intermediate (the green data points), and outer (the red data points) region, respectively. Truncated (the solid curve) and non-truncated (the dashed curves) power-law fits are overlaid in matching colours. Our mass completeness limit is indicated by the black vertical dashed line.

that the former is more reliable than the latter as it is not affected by biases related to binning and it can account for uncertainties of the cloud masses.

Cumulative mass distribution functions can be characterized quantitatively by a power-law function:

$$N(M' > M) = \left(\frac{M}{M_0}\right)^{\gamma+1}, \tag{8}$$

where $N(M' > M)$ is the number of clouds with a mass greater than M, M_0 sets the normalization, and γ is the power-law index. Alternatively, a truncated power-law function can be used:

$$N(M' > M) = N_0\left[\left(\frac{M}{M_0}\right)^{\gamma+1} - 1\right], \tag{9}$$

where M_0 is now the cut-off mass of the distribution and N_0 is the number of clouds with a mass $M > 2^{1/(\gamma+1)}M_0$, the cut-off point of the distribution (for a meaningful truncation to exist, one expects $N_0 \gg 1$).

We fit the cumulative mass spectra by applying the 'error in variables' method developed by Rosolowsky (2005), which adopts an iterative maximum-likelihood approach to estimate the best-fitting parameters and accounts for uncertainties of both the cloud mass and the number distribution. Fitting is only performed above the completeness limit of $M_{\rm com} = 4 \times 10^4$ M$_\odot$, shown as a black vertical dashed line in Fig. 5. We estimate the mass completeness limit based on the minimum spatially resolved cloud (gaseous) mass ($M_{\rm min}$) and the observational sensitivity, i.e. $M_{\rm com} \equiv M_{\rm min} + 10\delta_{\rm M}$, where the contribution to the mass due to noise, $\delta_{\rm M}$, is estimated by multiplying our RMS column density sensitivity limit of 10 M$_\odot$ pc^{-2} by the synthesized beam area of $\approx$180 pc^2. The parameters of the best-fitting truncated power laws to the cumulative (gaseous) mass distributions of the clouds in NGC 4429 are listed in Table 2.

Table 2. Parameters of the truncated power laws best fitting the cumulative gaseous mass distributions of the clouds in NGC 4429.

Region	Distance (pc)	γ	M_0 (10^5 M$_\odot$)	N_0
All	$0 < R_{\rm gal} \leq 450$	-2.18 ± 0.21	8.8 ± 1.3	6.9 ± 4.4
Inner	$0 < R_{\rm gal} \leq 220$	-2.32 ± 0.24	9.2 ± 2.5	1.4 ± 1.9
Intermediate	$220 < R_{\rm gal} \leq 330$	-1.83 ± 0.33	10.6 ± 1.6	5.2 ± 5.5
Outer	$330 < R_{\rm gal} \leq 450$	-2.08 ± 0.32	4.6 ± 0.4	6.6 ± 5.4

Note. All uncertainties are quoted at the 1σ level.

We find strong evidence for a curtailment of very massive GMCs in NGC 4429, as a truncated power-law function (the black solid line in Fig. 5) with a high value of N_0 (6.9 ± 4.4) fits the gaseous mass distribution much better than a pure power-law function (the black-dashed line). This implies that NGC 4429 lacks the processes that actively accumulate molecular gas clumps into high-mass GMCs. The best truncated fit yields a slope $\gamma = -2.18 \pm 0.21$, a slope steeper than -2 implying that most of the molecular gas mass of NGC 4429 is in low-mass clouds and there should thus be a significant amount of gas below our completeness limit. This is consistent with the fact that only ≈ 60 per cent of the emission is decomposed into clouds at our resolution (see Section 3.2). However, there must also be a lower gaseous mass limit for the molecular clouds or a turnover at low mass for the total mass to remain finite.

Our derived slope γ is similar to that measured for the clouds in the outer Galaxy (-2.2 ± 0.1; Rice et al. 2016), the ETG NGC 4526 (-2.39 ± 0.03; Utomo et al. 2015), M51 (-2.3 ± 1; Colombo et al. 2014), and the outer regions of M33 (-2.1 ± 1; Rosolowsky et al. 2007), but is steeper than that for the clouds in the inner Galaxy (-1.6 ± 0.1; Rice et al. 2016), the spiral arms of M51 (-1.79 ± 0.09; Colombo et al. 2014), NGC 1068 (-1.25 ± 0.07; Tosaki et al. 2017), the inner regions of M33 (-1.8 ± 1; Rosolowsky et al. 2007), NGC 300 (-1.80 ± 0.07; Faesi et al. 2016), and the overall mass spectrum of Local Group galaxies (≈ -1.7; Blitz et al. 2007).

The best-fitting cut-off gaseous mass M_0 of our truncated distribution [$(8.8 \pm 1.3) \times 10^5$ M$_\odot$] is comparable to that for the clouds in the outer Galaxy [$(1.5 \pm 0.5) \times 10^6$ M$_\odot$; Rice et al. 2016] and the inner regions of M33 [$(7.4 \pm 0.5) \times 10^5$ M$_\odot$; Rosolowsky et al. 2007], but is much lower than that for the clouds in most other galaxies such as the inner Galaxy [$(1.0 \pm 0.2) \times 10^7$ M$_\odot$; Rice et al. 2016], the ETG NGC 4526 [$(4.12 \pm 0.08) \times 10^6$ M$_\odot$; Utomo et al. 2015], M51 [$(1.8 \pm 0.3) \times 10^6$ M$_\odot$; Colombo et al. 2014], NGC 1068 [$(5.9 \pm 0.6) \times 10^7$ M$_\odot$; Tosaki et al. 2017], and the outer regions of M33 [$(3.4 \pm 1.2) \times 10^6$ M$_\odot$; Rosolowsky et al. 2007].

Variations of the GMC gaseous mass distribution as a function of galactocentric distance can also be quantified. We find the cloud cumulative gaseous mass functions of the three regions to be slightly different, with a best-fitting truncated slope γ of -2.32 ± 0.24, -1.83 ± 0.33, and -2.08 ± 0.32 and a cut-off gaseous mass M_0 of $(9.2 \pm 2.5) \times 10^5$, $(10.6 \pm 1.6) \times 10^5$, and $(4.6 \pm 0.4) \times 10^5$ M$_\odot$ in the inner, intermediate, and outer region, respectively. The distributions of the clouds in the inner and outer regions appear to be similar at gaseous masses below 2×10^5 M$_\odot$, but the latter shows a truncation, while the former seems to be better fit by a pure power law even at the high-mass end. Massive clouds appear to be suppressed at the galaxy centre and especially in the outer regions of the disc. Indeed, the distribution of clouds with gaseous masses greater than the completeness limit cuts off abruptly inside 40 pc and beyond 450 pc (see Fig. 3). More than half of the most massive clouds ($>2.5 \times 10^5$ M$_\odot$) are located in the intermediate region, implying that the survival of massive clouds is more favoured in this region. Overall, the environmental dependence of the gaseous mass spectrum indicates that the formation and destruction mechanisms of GMCs are (slightly) different at different galactocentric distances.

4 CLOUD KINEMATICS

4.1 Velocity gradients of individual clouds

We observe strong velocity gradients within individual GMCs. Many authors argue that these gradients are the signature of cloud rotation (e.g. Blitz 1993; Phillips 1999; Rosolowsky et al. 2003; Rosolowsky 2007; Utomo et al. 2015). The observed velocity gradient of each cloud can be quantified by fitting a plane to its intensity-weighted first moment (i.e. mean line-of-sight velocity) map $\bar{v}(x, y)$:

$$\bar{v}(x, y) = ax + by + c, \tag{10}$$

where a and b are the projected velocity gradient along, respectively, the x- and the y-axis on the sky (selected here in the standard/intuitive manner, i.e. reversely proportional to the right ascension and proportional to the declination, respectively). We adopt the code `lts_planefit` to perform the fits. This code combines least-trimmed-squares robust techniques (Rousseeuw & Driessen 2006) into a least-squares fitting algorithm, and allows for intrinsic scatter, uncertainties, possible large outliers and weighting of each pixel by its flux (i.e. gaseous mass surface density). The projected angular velocity $\omega_{\rm obs}$ (i.e. the magnitude of the projected velocity gradient) and position angle of the rotation axis $\phi_{\rm rot}$ are then given by the best-fitting coefficients:

$$\omega_{\rm obs} = \sqrt{a^2 + b^2}, \tag{11}$$

$$\phi_{\rm rot} = \tan^{-1}(b/a). \tag{12}$$

The uncertainties of $\omega_{\rm obs}$ and $\phi_{\rm rot}$ are estimated from the uncertainties of the parameters a and b using standard error propagation rules. We note that these derived projected angular velocities $\omega_{\rm obs}$ are underestimated by a factor $1 - \cos(\varphi)$ compared to the intrinsic ones [i.e. $\omega_{\rm obs} = \cos(\varphi)\omega_{\rm int}$], where φ is the angle between the cloud rotation axis and the plane of the sky. This is, however, inconsequential for all following analyses and discussions, as all modelled quantities will themselves be projected on to the sky (according to the model assumptions) before comparison.

Fitting a plane to the mean line-of-sight velocity map of each cloud implicitly assumes cloud solid-body rotation. While this may not be intrinsically true (i.e. the angular velocity may depend on the radius within each cloud), because our clouds are generally relatively poorly spatially resolved, $\omega_{\rm obs}$ as defined above nevertheless provides a useful single quantity to quantify the bulk (projected) rotation of each cloud.

Fig. 6 provides one example of our plane fitting to the mean line-of-sight velocity map of a cloud of NGC 4429. The left-hand panel shows the intensity-weighted first moment map with the best-fitting rotation axis (the black line) and centre (the black solid circle) overplotted. For illustrative purposes only, the right-hand panel shows the mean velocity of each pixel within the cloud ($\bar{v}(x, y)$) against the perpendicular distance of the pixel from the best-fitting cloud rotation axis. A cloud with solid-body rotation should have all its data points well fit by a straight line, as is the case here. Overall, we find that planes are reasonable fits to the velocity maps of most of the clouds in NGC 4429, and the median value of the reduced χ^2 for the 141 spatially resolved clouds is $\chi^2_{\rm r} = 0.8$. More than half (82) of the resolved clouds are well fit by solid-body rotation ($\chi^2_{\rm r} \leq 1$).

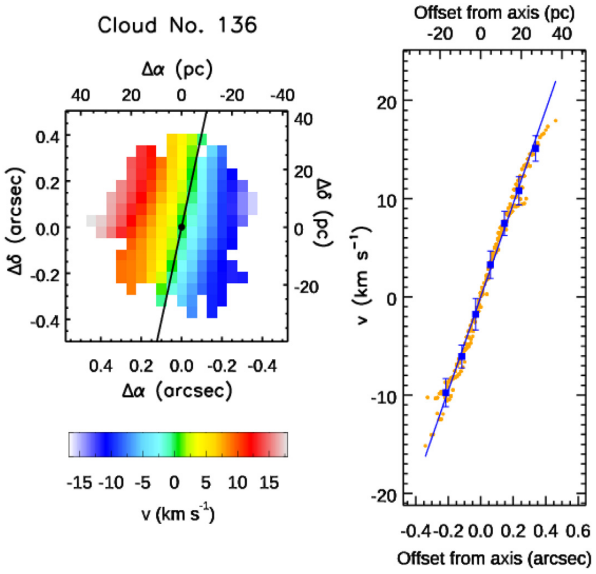

Figure 6. One example of plane fitting to the intensity-weighted first moment (i.e. mean line-of-sight velocity) map of a cloud of NGC 4429 (here cloud no. 136). The left-hand panel shows the cloud's mean velocity map with the best-fitting rotation axis (the black line) and centre (the black solid circle) overplotted. The right-hand panel shows the mean line-of-sight velocity of each pixel within the cloud against the perpendicular distance of the pixel from the best-fitting rotation axis (the orange data points). The blue squares are means of the velocity in bins of perpendicular distance from the rotation axis. For illustrative purposes only, the blue line shows the best-fitting straight line to the data, indicating that solid-body rotation is a good description of the cloud's kinematics.

The best-fitting results are listed in Table 1. The projected velocity gradients $\omega_{\rm obs}$ of the 141 spatially resolved clouds range from 0.05 to 0.91 km s^{-1} pc^{-1}, with an average of ≈0.33 km s^{-1} pc^{-1}. Our derived velocity gradients are significantly larger than those inferred for MW clouds (∼0.1 km s^{-1} pc^{-1}; Blitz 1993; Phillips 1999; Imara & Blitz 2011), M33 (≈0.15 km s^{-1} pc^{-1}; Rosolowsky et al. 2003; Imara, Bigiel & Blitz 2011), and M31 (0–0.2 km s^{-1} pc^{-1}; Rosolowsky 2007), but they are comparable to those inferred for the clouds of the ETG NGC 4526 (0–1.0 km s^{-1} pc^{-1}; Utomo et al. 2015).

4.2 Origin of the clouds' velocity gradients

The observed velocity gradients of the clouds can arise from turbulent motions, the clouds' intrinsic rotation and/or galaxy rotation. Burkert & Bodenheimer (2000) suggested that turbulent velocity fields can produce observed linear gradients that were estimated to be of order 0.08 km s^{-1} pc^{-1} for their median cloud radius of 20 pc. As our measured (i.e. projected) velocity gradients are generally much larger than this, we suggest turbulence is not important to account for them.

The observed velocity gradients of the clouds in NGC 4429 are more likely produced by the intrinsic rotation of the clouds and/or galaxy rotation. Galaxy rotation can produce velocity gradients across the small areas occupied by GMCs, especially at small galactocentric distances corresponding to the steep part of the rotation curve. To identify the origin of the observed velocity gradients of the clouds of NGC 4429, we overplot the rotation axes of the individual clouds (i.e. the projected directions of their angular momentum vectors) on the isovelocity contours of the galaxy in Fig. 7. If the velocity gradients of the clouds are produced by the clouds' intrinsic rotation, their rotation axes should be randomly distributed. On the other hand, if the velocity gradients of the clouds are produced by the galaxy rotation, their rotation axes should show a strong alignment with the galaxy isovelocity contours.

As shown in Fig. 7, we do find a strong tendency for the projected angular momentum vectors of the clouds to be tangential to the isovelocity contours of NGC 4429, implying that the observed velocity gradients of the clouds are primarily a consequence of galactic rotation. This is similar to the trend in NGC 4526 (Utomo et al. 2015), but different from that in the MW (Koda et al. 2006) and M31 (Rosolowsky 2007), where the distributions of position angles are random.

Here, the isovelocity contours due to the galaxy rotation were derived by creating a gas dynamical model using the `Kinematic Molecular Simulation` (`KinMS`) package of Davis et al. (2013). Inputs to the model include the stellar mass distribution, stellar mass-to-light ratio, SMBH mass, as well as the disc orientation (position angle and inclination), and position (spatially and spectrally). The stellar mass distribution is parametrized by a multi-Gaussian expansion (MGE; Emsellem, Monnet & Bacon 1994) fit to a *V*-band image from *HST* (Davis et al. 2018). The free parameters are derived by fitting to the observed gas kinematics, assuming the object is axisymmetric (in the central parts where CO is located) and the gas in circular rotation (see Davis et al. 2018 for details of the fitting procedures and the best-fitting parameters). The dark matter and gas masses are not included in our model, as they are small compared to those of the SMBH and stars. We note that a variable mass-to-light ratio has been adopted, as required by the data, with a piecewise linear form as a function of radius. An inclination angle of 68° and a kinematic position angle of 93° (as measured in that work) are adopted to calculate the line-of-sight projection of the gas circular velocities.

To further quantify the effects of the galaxy rotation on our observed velocity gradients, we compare the measured angular velocities and position angles of the rotation axes of the clouds in NGC 4429 to those expected from a pure galaxy rotation model. We measure the projected angular velocities and rotation axes of the model over the same areas as for the observed clouds, using the methods described in Section 4.1. We assume that the motion of the gas within each cloud (i.e. each fluid element of each cloud) follows perfectly circular orbits defined by our kinetic model above. We find a strong correlation between the modelled and observed position angles (with a median angle difference of ≈19°), supporting the idea that the observed cloud-scale velocity gradients are aligned with the large-scale velocity field, as suggested by Fig. 7.

A general correlation between the modelled and observed angular velocities is also found. Our model overestimates the observed angular velocities $\omega_{\rm obs}$ by a median factor of 2, much smaller than the $\omega_{\rm mod}/\omega_{\rm obs}$ ratios found for clouds in WISDOM LTGs ($\omega_{\rm mod}/\omega_{\rm obs} \gtrsim 10$; Shu et al., in preparation; Choi et al., in preparation). This discrepancy between the amplitudes of the observed and modelled angular velocities is unlikely to be due to the clouds' own rotations, as the observed position angles $\phi_{\rm rot}$ of the clouds would then be expected to deviate from the modelled ones randomly. A possible explanation is that the self-gravity of the clouds is also important, so that the clouds do not follow pure galaxy rotation (see Section 6.2 for more discussion of this). The discrepancy could also partly be due to the limitation of `CPROPS` to isolate individual clouds in highly crowded environments. To reduce the ambiguities due to cloud blending, we fit both the data and model again without including the outermost boundary pixels of each cloud. In this case, a strong correlation between the modelled and observed position angles is again present (see the right-hand panel of Fig. 8), with a median angle difference

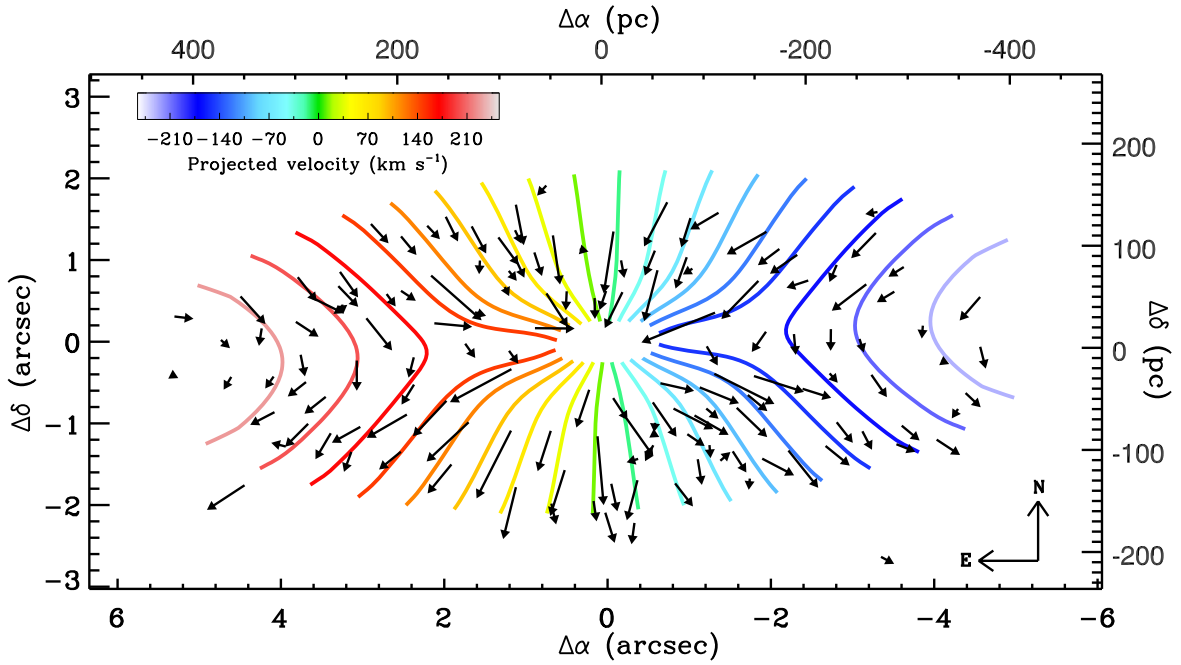

Figure 7. Projected directions of the angular momentum vectors of individual spatially resolved GMCs in NGC 4429 (the black arrows), overplotted on the isovelocity contours of the molecular gas (colour coded by the projected velocities). The length of the arrows represents the magnitudes of the velocity gradients (i.e. $\omega_{\rm obs}$). The projected velocities are derived from our gas dynamical model assuming pure rotation (see text).

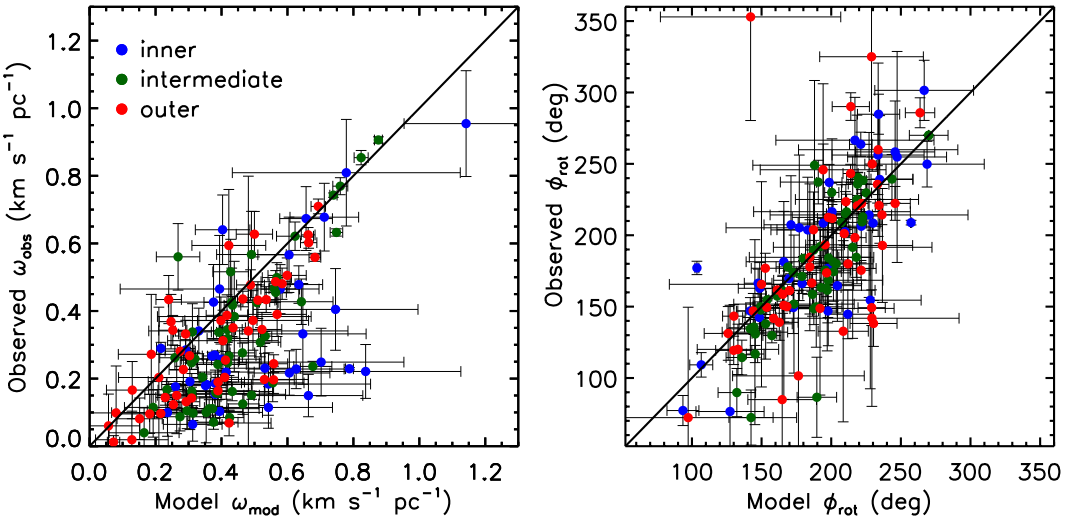

Figure 8. Correlations between the modelled and observed projected angular velocities $\omega_{\rm obs}$ (left-hand panel) and position angles of the rotation axes $\phi_{\rm rot}$ (right-hand panel) for the 141 spatially resolved clouds of NGC 4429. The data points are colour-coded by region and the black solid lines show the 1:1 relations.

of ≈16°, but the model overestimates the observed angular velocities by a reduced median factor of 1.5 only (left-hand panel of Fig. 8). In the inner region, where the clouds are more blended in both space and velocity, the discrepancies between the modelled and observed angular velocities is worse (with a median factor of 2), and the angle difference is larger (with a median value of ≈20°). In the outer region, where clouds are less blended, the model shows a much better agreement with the observations (with a median angular velocity discrepancy factor of only 1.2 and a median angle difference of only ≈14°)

In summary, a comparison of the observed and modelled projected angular velocities and rotation axes of individual clouds suggests that the observed velocity gradients of the clouds in NGC 4429 are primarily caused by the local circular orbital motions, themselves due to the galaxy potential. We note that the good match between our observations and model suggests that the motion of the gas within each cloud of NGC 4429 mainly follows gravitational orbital (and thus shear) motions rather than epicyclic motions (see Section 6.1 for more discussion of this issue).

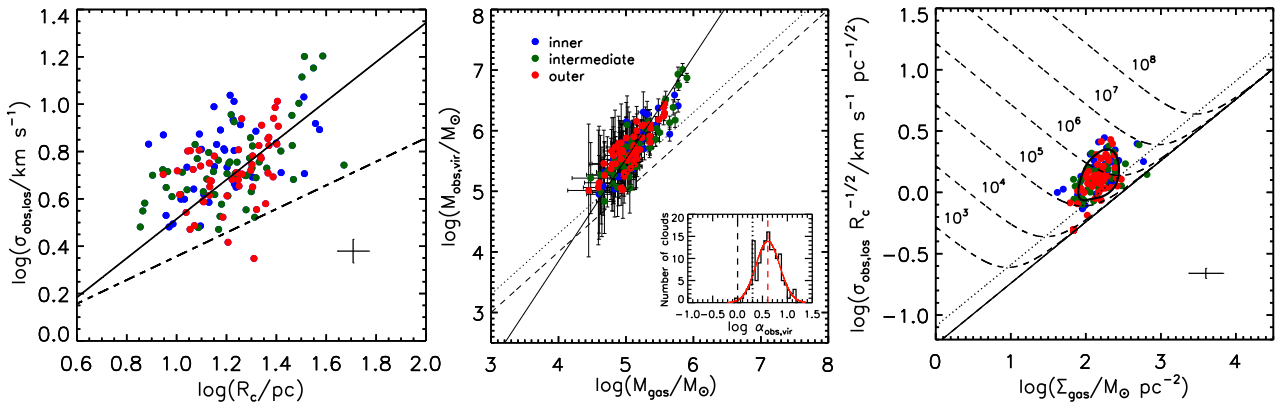

Figure 9. Left: Size–linewidth relation of the 141 spatially resolved clouds of NGC 4429, using the observed velocity dispersion $\sigma_{\rm obs,los}$. The black solid line shows the best-fitting relation, while the black-dashed line shows Larson's relation for the Milky Way disc (Solomon et al. 1987). Middle: Correlation between virial mass and gaseous mass for the same spatially resolved clouds. The black solid line shows the best-fitting relation, while the black-dashed and dotted diagonal lines show the 1:1 and 2:1 relations, respectively. The distribution of $\log(\alpha_{\rm obs,vir})$ (the black histogram) with a lognormal fit overlaid (the red solid line) is shown in an inset. The red-dashed line in the inset indicates the mean of the lognormal fit, while the black-dashed and dotted lines indicate $\alpha_{\rm vir} = 1$ and $\alpha_{\rm vir} = 2$, respectively. Right: Correlation between $\sigma_{\rm obs,los} R^{-1/2}$ and gaseous mass surface density ($\Sigma_{\rm gas}$) for the same spatially resolved clouds. The black solid contour encloses 68 per cent of the data points. The black solid and dotted diagonal lines show the solution for simple (i.e. $\alpha_{\rm vir} = 1$) and marginal (i.e. $\alpha_{\rm vir} = 2$) virial equilibria, respectively. The V-shaped black-dashed curves show solutions for pressure-bound clouds at different pressures ($P_{\rm ext}/k_{\rm B} = 10^3$, 10^4, ⋯, 10^8 K cm^{-3}). Data points are colour-coded by region in all three panels. Typical uncertainties are shown as a black cross in the bottom right corner of the left-hand and right-hand panels.

5 DYNAMICAL STATE OF CLOUDS

5.1 Cloud scaling relations using the observed velocity dispersion

The scaling relations between the physical properties of molecular clouds have become a standard tool for assessing the clouds' physical states and dynamical conditions (e.g. Blitz et al. 2007; Hughes et al. 2013). The most fundamental relation is the size–linewidth relation, a.k.a. Larson's first relation (e.g. Larson 1981; Solomon et al. 1987), which has become the yardstick for GMC studies in the MW and external galaxies (e.g. Bolatto et al. 2008). The size–linewidth relationship is usually interpreted as a signature of the turbulent motions within clouds (e.g. Falgarone, Phillips & Walker 1991; Elmegreen & Falgarone 1996; Lequeux 2005), and it provides a unique probe of the dynamical state of the turbulent molecular gas in extragalactic star-forming systems.

Another important scaling relation providing crucial insights is the correlation between the clouds' dynamical (i.e. virial) masses $M_{\rm vir}$ and their true masses M (here taken to be the gaseous masses $M_{\rm gas}$). The comparison of the virial and gaseous masses provides an important clue to the dynamical state of the clouds according to the virial theorem. Indeed, the virial parameter

$$\begin{aligned}\alpha_{\rm vir} &\equiv \frac{M_{\rm vir}}{M} \\ &= \frac{\sigma^2 R_{\rm c}}{b_{\rm s} G M} \\ &= \frac{2\,\frac{1}{2} M \sigma^2}{b_{\rm s} G M^2 / R_{\rm c}}\end{aligned} \tag{13}$$

(see equation 7) is equal to the ratio of two times the turbulent kinetic energy to the (absolute value of the) self-gravitational energy of a cloud, quantifying the degree of gravitational boundedness of the cloud. If the virial parameter of a cloud $\alpha_{\rm vir} \approx 1$, the cloud is gravitationally bound and in virial equilibrium. If its virial mass is much larger than its gaseous mass ($\alpha_{\rm vir} \gg 1$), the cloud has to be confined by external pressure (it would otherwise disperse) and it is unlikely to be bound (i.e. it is a transient feature of the ISM). If $\alpha_{\rm vir} \lesssim 1$, the molecular cloud is likely unstable to gravitational collapse. We note that a critical parameter $\alpha_{\rm crit} \approx 2$ is often regarded as the threshold between gravitationally bound and unbound objects (Kauffmann, Pillai & Zhang 2013; Kauffmann et al. 2017).

A third important scaling relation is the correlation between the clouds' mass surface densities Σ (again taken here to be the gaseous mass surface densities $\Sigma_{\rm gas}$) and the quantities $\sigma R_{\rm c}^{-1/2}$ (where as before σ and $R_{\rm c}$ are a measure of the observed/1D velocity dispersion and size of each cloud, respectively). The $\sigma R_{\rm c}^{-1/2}$–$\Sigma_{\rm gas}$ plot provides a necessary modification to Larson's scaling relations. It implies an additional constraint to the velocity dispersion, whereby the velocity dispersion of a cloud depends on both its spatial extent and its gaseous mass surface density (Field, Blackman & Keto 2011). If clouds are virialized (and do not necessarily obey Larson's first relation), observations should cluster around the line $\sigma R_{\rm c}^{-1/2} = \sqrt{\pi G b_{\rm s} \Sigma_{\rm gas}}$ ($b_{\rm s} = 1/5$ for a homogeneous spherical cloud; see the black solid diagonal line in the right-hand panel of, e.g. Fig. 9). If clouds are not virialized but are marginally gravitationally bound (i.e. $\alpha_{\rm vir} \approx \alpha_{\rm vir,crit} = 2$), the data points should cluster around the line $\sigma R_{\rm c}^{-1/2} = \sqrt{2\pi G b_{\rm s} \Sigma_{\rm gas}}$ (see the black-dotted diagonal line in the right-hand panel of, e.g. Fig. 9). If clouds are not gravitationally bound, external pressure ($P_{\rm ext}$) must play an important role to confine the clouds, and the clouds should be distributed along the black V-shaped dashed curves in the right-hand panel of Fig. 9: $\sigma R_{\rm c}^{-1/2} = \sqrt{\pi G b_{\rm s} \Sigma_{\rm gas} + \frac{4 P_{\rm ext}}{3 \Sigma_{\rm gas}}}$ (Field et al. 2011). We note that for the largest $\Sigma_{\rm gas}$ of each V-shaped curve, the clouds are dominated by self-gravity and the equilibrium curve is asymptotic to the solution of the simple virial equilibrium (SVE; i.e. the black solid diagonal line; Field et al. 2011).

For consistency with GMC studies in the MW and external galaxies in the literature, we first adopt the observed velocity dispersion $\sigma_{\rm obs,los}$ (see Section 3.1) to explore the above three scaling relations. As seen in the left-hand panel of Fig. 9 (data points and the black solid line), there is a strong correlation between size and

linewidth (with a Spearman rank correlation coefficient of 0.5) for the 141 clouds of NGC 4429 that are spatially resolved, the only clouds where a reliable measurement of the size R_c is possible (see Table 1). However, the relation departs from the traditional one derived for clouds in the MW disc (the black-dashed line in the left-hand panel of Fig. 9; Solomon et al. 1987; Dame, Hartmann & Thaddeus 2001; Rice et al. 2016). The observed tendency is for clouds to exhibit a higher velocity dispersion at a given size. Our results also reveal a steep size–linewidth relation,

$$\log\left(\frac{\sigma_{\rm obs,los}}{\rm km\ s^{-1}}\right) = (-0.30 \pm 0.17) + (0.82 \pm 0.13)\log\left(\frac{R_c}{\rm pc}\right), \quad (14)$$

steeper than that of clouds in the MW disc (0.5 ± 0.05; Solomon et al. 1987). The slope is also marginally steeper than that derived for CMZ clouds (0.66 ± 0.18; Kauffmann et al. 2017), but the zero-point is much smaller (5.5 ± 1.0 for CMZ clouds; Kauffmann et al. 2017), and the velocity dispersions of CMZ clouds are indeed higher than those of the NGC 4429 clouds at any given size.

The virial masses of the spatially resolved clouds of NGC 4429 calculated from their observed velocity dispersions,

$$M_{\rm obs,vir} \equiv \frac{\sigma^2_{\rm obs,los} R_c}{b_s G} \quad (15)$$

(see equation 7), are compared to their gaseous masses $M_{\rm gas}$ in the middle panel of Fig. 9, where as always we have assumed $b_s = \frac{1}{5}$ (spherical homogeneous clouds). We find virial masses significantly larger than the gaseous masses. A linear fit yields (the black solid line in the middle panel of Fig. 9)

$$\log\left(\frac{M_{\rm obs,vir}}{\rm M_\odot}\right) = (-2.91 \pm 0.43) + (1.69 \pm 0.08)\ \log\left(\frac{M_{\rm gas}}{\rm M_\odot}\right). \quad (16)$$

A lognormal fit to the distribution of the resulting virial parameters,

$$\alpha_{\rm obs,vir} \equiv \frac{M_{\rm obs,vir}}{M} = \frac{M_{\rm obs,vir}}{M_{\rm gas}}, \quad (17)$$

shown as an inset in the middle panel of Fig. 9, yields a mean $\langle\alpha_{\rm obs,vir}\rangle = 4.04 \pm 0.22$ and a standard deviation of 0.24 dex. In particular, all resolved clouds have $\alpha_{\rm obs,vir} > 1$.

The derived $\sigma_{\rm obs,los} R_c^{-1/2}$–$\Sigma_{\rm gas}$ relation is presented in the right-hand panel of Fig. 9 for the spatially resolved clouds of NGC 4429. The gaseous mass surface densities $\Sigma_{\rm gas}$ of the GMCs vary by one order of magnitude, and the size–linewidth coefficient ($\sigma_{\rm obs,los} R_c^{-1/2}$) increases with increasing $\Sigma_{\rm gas}$. The data points do not lie along the solid diagonal line of the SVE, but are instead offset from it and distributed across the V-shaped curves. If pressure is important to the dynamical state of the clouds, the clouds in NGC 4429 seem to experience a wide range of considerable external pressures ($P_{\rm ext}/k_B \approx 10^5$–$10^7$ K cm^{-3}, where k_B is Boltzmann's constant). Overall, Fig. 9 thus seems to suggest that the kinetic energy of the clouds in NGC 4429 is more important than their gravitational energy, hence the clouds are either not bound or tend towards pressure equilibria.

However, a major concern about the use of the above relations to assess the dynamical states of clouds in NGC 4429 is the applicability of the observed velocity dispersion $\sigma_{\rm obs,los}$. The difference of the derived size–linewidth relation with respect to the Solomon et al. (1987) trend seems to imply that the measured linewidths of the clouds are not set purely by their internal virialized motions and/or turbulence (Meidt et al. 2013; Kauffmann et al. 2017). Recent works suggest that, in the centre of galaxies where strong shear and tidal forces are present, a considerable part of the cloud-scale gas motions is due to these external galactic forces (e.g. Meidt et al. 2018; Utreras et al. 2020). We have already demonstrated that the observed strong velocity gradients of the clouds in NGC 4429, which reflect the velocity gradients in the plane of the galaxy, are mainly a consequence of local orbital motions defined by the background galactic gravitational potential (i.e. the galaxy circular velocity curve; see Section 4.2). In this case, the steep slope of the size–linewidth relation (see the left-hand panel of Fig. 9) can be explained as resulting from the decay of fast orbit-induced large-scale motions to transonic conditions on small spatial scales (Kauffmann et al. 2017).

The question then is whether gas motions associated with the background galactic potential should also be involved in assessing the dynamical states and stability of the clouds. Intuitively, gas motions due to external galactic forces should be considered when calculating a cloud's kinetic energy that is meant to balance its self-gravitational energy (Chen et al. 2016; Meidt et al. 2018). Conversely, in the presence of strong galactic forces, self-gravity is no longer the only force binding a cloud. Therefore, to verify whether clouds are virialized in a galactic environment where tidal/shear forces are strong, one needs to modify the conventional virial theorem to include (1) external forces arising from the background galactic potential and (2) the gas motions induced by these forces. We do exactly that in the next sub-sections.

5.2 Basic framework

We recall here a key conceptual point emphasized in Section 1. We will not assume here that the clouds of NGC 4429 are in dynamical equilibrium, and then deduce the clouds' gravitational motions due to the external (i.e. galactic) potential. Rather, we will measure and quantify the clouds' gravitational motions due to the external potential, and then deduce whether the clouds are indeed in dynamical equilibrium. This is the only way to reliably assess whether GMCs are in dynamical equilibrium (and thus long-lived) or out of equilibrium (and thus transient), arguably the most important question in the field.

As described in detail in Appendix A, we envision each cloud as a continuous structure with well-defined borders in position- and velocity-space, located in a rotating gas disc with a circular velocity determined by the shape of the background galactic gravitational potential. Each cloud's centre of mass (CoM) is assumed to be in the mid-plane of the disc. We assume that each fluid element of a cloud experiences two kinds of motions: (1) random turbulent motions arising from self-gravity (cloud gravitational potential $\Phi_{\rm sg}$), which have a velocity dispersion $\sigma_{\rm sg}$, and (2) bulk gravitational motions associated with the external (i.e. galactic) potential ($\Phi_{\rm gal}$), which have an RMS velocity $\sigma_{\rm gal}$ ($\sigma_{\rm gal} \equiv \frac{\int v^2_{\rm gal}\,{\rm d}m}{M}$, where $v_{\rm gal}$ is the velocity of each fluid element due to gravitational motions relative to the CoM, the integral is over all fluid elements dm, and $\int {\rm d}m = M$). Thermal motions are ignored, as they are often small compared to turbulent motions in a cold gas cloud (e.g. Fleck 1980). We assume the motions due to self-gravity ($\sigma_{\rm sg}$) and the background galactic potential ($\sigma_{\rm gal}$) to be uncorrelated, and the cloud's own gravitational potential $\Phi_{\rm sg}$ to be (statistically) independent of the local external gravitational potential defined by the galaxy $\Phi_{\rm gal}$. The turbulent motions due to self-gravity are expected to be quasi-isotropic in three dimensions (Field, Blackman & Keto 2008; Ballesteros-Paredes et al. 2011), while the gas motions induced by the external gravitational potential are often non-isotropic (Meidt et al. 2018). Gravitational motions in the plane are assumed to be separable from those in the vertical

direction. We consider only the effects of gravitational forces and ignore external pressure and magnetic fields.

With those considerations, the resulting MVT can be split into two independent parts:

$$\frac{\ddot{I}}{2} \approx \underbrace{\left[3M\sigma^2_{\rm sg,los} - 3b_{\rm s}GM^2/R_{\rm c}\right]}_{\text{self gravity}} + \Bigg[\underbrace{M\left(\sigma^2_{\rm gal,z} - b_{\rm e}\nu_0^2 Z_{\rm c}^2\right)}_{\text{external, vertical direction}} + \underbrace{M\left(\sigma^2_{\rm gal,r} + \sigma^2_{\rm gal,t} + b_{\rm e}\left(T_0 - 2\Omega_0^2\right)R_{\rm c}^2\right)}_{\text{external, plane}}\Bigg], \quad (18)$$

where I, M, $R_{\rm c}$, and $Z_{\rm c}$ are, respectively, the cloud's moment of inertia, the mass, the radius, and the scale height, $\nu_0^2 \equiv 4\pi G\rho_{*,0}$ (formally the total mass volume density evaluated at the cloud's CoM, but we use here $\rho_{*,0}$, the stellar mass volume density ρ_* evaluated at the cloud's CoM using our MGE model, as it is accurately constrained; see Appendix C), $b_{\rm s}$ is the aforementioned geometrical factor that quantifies the effects of inhomogeneities and/or non-sphericity associated with self-gravity, $b_{\rm e}$ is a geometrical factor that quantifies the effects of inhomogeneities (only) associated with external gravity ($b_{\rm e} = \frac{(1-\psi/3)}{(5-\psi)}$ for a spherical cloud with a radial mass volume density profile $\rho(r) \propto r^{-\psi}$, thus $b_{\rm e} = b_{\rm s} = \frac{1}{5}$ for a spherical homogeneous cloud as before; see Appendix A for more details on $b_{\rm e}$), $\sigma_{\rm sg,los}$ is the cloud's 1D turbulent velocity dispersion due to self-gravity, $\sigma_{\rm gal,r}$, $\sigma_{\rm gal,t}$, and $\sigma_{\rm gal,z}$ are the RMS velocity of gas motions due to external gravity in, respectively, the radial (i.e. the direction pointing from the galaxy centre to the cloud's CoM), azimuthal (i.e. the direction along the orbital rotation), and vertical (i.e. the direction perpendicular to the cloud's orbital plane) direction (as measured in an inertial frame, i.e. by a distant observer; see Appendix A for a more detailed discussion of $\sigma_{\rm gal,r}$ and $\sigma_{\rm gal,t}$), Ω_0 is the circular orbital angular velocity Ω at the cloud's CoM, and $T_0 \equiv -R\frac{{\rm d}\Omega^2(R)}{{\rm d}R}|_{R=R_0}$ is the tidal acceleration per unit length in the radial direction T (e.g. Stark & Blitz 1978) evaluated at the cloud's CoM (R is the galactocentric distance in the plane of the disc and R_0 that of the cloud's CoM). We note that here and throughout, $\Omega(R)$ is the theoretical quantity $\Omega(R) \equiv \sqrt{\frac{1}{R}\frac{{\rm d}\Phi_{\rm gal}(R)}{{\rm d}R}}$ defined by the galaxy potential $\Phi_{\rm gal}$, i.e. it is the angular velocity of a fluid element moving in perfect circular motion [$\Omega(R) = V_{\rm circ}(R)/R$, where $V_{\rm circ}(R)$ is the circular velocity curve] rather than the observed angular velocity of the fluid element [$V_{\rm rot}(R)/R$, where $V_{\rm rot}$ is the observed rotation curve]. The first term in square brackets on the right-hand side of equation (18) comprises the energy terms regulated by self-gravity, while the second term in square brackets contains the contributions of external gravity to the cloud's energy budget ($E_{\rm ext}$) in, respectively, the vertical direction ($E_{\rm ext,z}$) and the plane ($E_{\rm ext,plane}$). The detailed derivation of equation (18) and its more general form for a homogeneous ellipsoidal cloud (equation A14) is provided in Appendix A.

For reference, we show in Fig. 10 the dependence of Ω, Oort's constants A and B, T and $T - 2\Omega^2$ on galactocentric distance R in NGC 4429. The functions Ω, A, and T are always positive, B is always negative, while $T - 2\Omega^2$ is generally negative except in the very centre. We note that $T = 4A\Omega = 4\Omega(B + \Omega)$. The rotational shear (i.e. Oort's constant A) in NGC 4429 is much larger ($\geq$0.2 km s^{-1} pc^{-1} at galactocentric distances $R \lesssim 450$ pc, where the clouds are located) than that in the bulk of the Galactic disc ($\approx$0.02 km s^{-1} pc^{-1} at $R \geq 3$ kpc; Dib et al. 2012) and the LMC ($\approx$0.018 km s^{-1} pc^{-1} at $R \geq 1$ kpc; Thilliez et al. 2014).

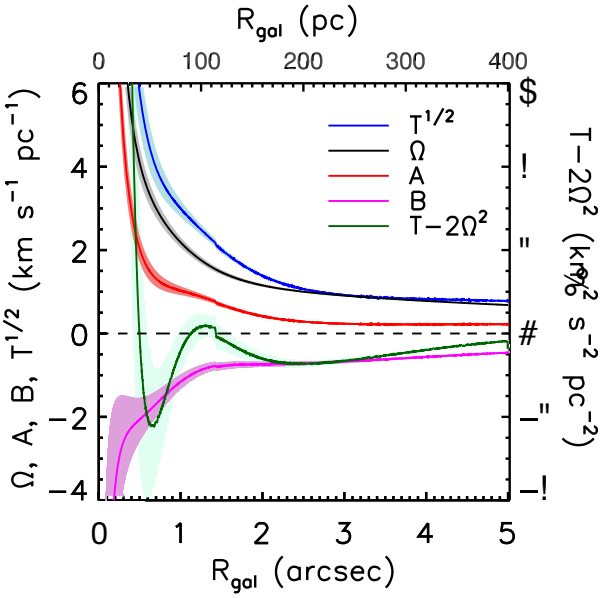

Figure 10. Galactocentric distance ($R_{\rm gal}$) dependence of the orbital angular velocity Ω, Oort's constants A and B, the tidal acceleration per unit length in the radial direction T, and the function $T - 2\Omega^2$ in NGC 4429, as calculated from our gas dynamical model. The black-dashed horizontal line indicates an ordinate of 0. The coloured envelopes around each curve indicate the $\pm1\,\sigma$ uncertainties. We note that the slight discontinuity in the radial profiles of A, B, T, and $T - 2\Omega^2$ at $R_{\rm gal} \approx 1\farcs4$ is caused by our adopted piecewise linear mass-to-light ratio radial profile $M/L(R)$ (see Davis et al. 2018), so that while $M/L(R)$ is continuous $\frac{{\rm d}M/L(R)}{{\rm d}R}$ is not.

5.3 Role of self-gravity

The first term in square brackets on the right-hand side of equation (18) describes an internal equilibrium regulated by self-gravity. For a cloud that attains virial balance between its internal turbulent kinetic energy ($\frac{3}{2}M\sigma^2_{\rm sg,los}$) and its self-gravitational energy ($U_{\rm sg} \equiv -3b_{\rm s}GM^2/R_{\rm c}$), such as an isolated self-gravitating cloud, these two terms should cancel out. To investigate the role of self-gravity, one thus needs to measure the cloud's turbulent velocity dispersion due to self-gravity only ($\sigma_{\rm sg,los}$). However, the observed velocity dispersion $\sigma_{\rm obs,los}$ is not necessarily equal to $\sigma_{\rm sg,los}$, as there are potentially significant contributions from bulk (galaxy-driven) gravitational motions. Indeed, the observed velocity dispersion $\sigma_{\rm obs,los}$ of a cloud can be expressed as

$$\sigma^2_{\rm obs,los} \approx \sigma^2_{\rm sg,los} + \left(\sigma^2_{\rm gal,r}\sin^2\theta + \sigma^2_{\rm gal,t}\cos^2\theta\right)\sin^2 i + \sigma^2_{\rm gal,z}\cos^2 i, \quad (19)$$

where i is the inclination of the galactic disc with respect to the line of sight, and θ is the (deprojected) azimuthal angle of the cloud's CoM with respect to the kinematic major axis of the disc (see equation 32 of Meidt et al. 2018).

We therefore need to reduce the contamination of our measured velocity dispersions by bulk gravitational motions. This is why we introduced a new measure of the velocity dispersion, $\sigma_{\rm gs,los}$, in Section 3.1, where we first shifted each line-of-sight velocity spectrum to match its centroid velocity ($\bar{v}(x, y)$) to that of the cloud's CoM ($\bar{v}(0, 0)$), and then measured the velocity dispersion (i.e. the second moment along the velocity axis) of the shifted emission distribution and extrapolated it to $T_{\rm edge} = 0$ K. The derived gradient-subtracted velocity dispersion $\sigma_{\rm gs,los}$ was then deconvolved by the

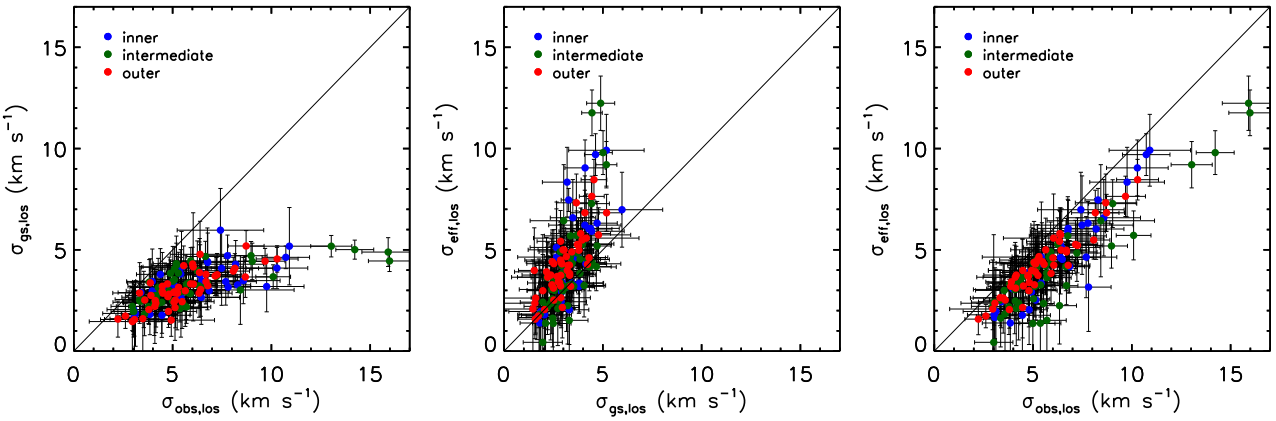

Figure 11. Comparisons of our observed ($\sigma_{\rm obs,los}$), gradient-subtracted ($\sigma_{\rm gs,los}$), and effective ($\sigma_{\rm eff,los}$) cloud velocity dispersion measures for the 141 spatially resolved clouds of NGC 4429. Data points are colour-coded by region in all three panels.

channel width ($\Delta V_{\rm chan}/\sqrt{2\pi}$), yielding our final adopted measure. Table 1 lists the derived $\sigma_{\rm gs,los}$ of all spatially resolved clouds and the left-hand panel of Fig. 11 shows a comparison of $\sigma_{\rm gs,los}$ and $\sigma_{\rm obs,los}$. As expected, $\sigma_{\rm gs,los} < \sigma_{\rm obs,los}$, and all particularly large $\sigma_{\rm obs,los}$ measurements have been corrected to $\lesssim$5 km s^{-1}.

The observed velocity gradient of a cloud is due to bulk motions within the cloud only. Assuming that the vertical gravitational motions can be treated as random motions that balance the weight of the disc (i.e. no bulk motion in the vertical direction), analogously to turbulent motions due to self-gravity, the only bulk motions will originate from in-plane gravitational motions. Our newly derived gradient-subtracted velocity dispersion $\sigma_{\rm gs,los}$ can therefore be written as

$$\sigma^2_{\rm gs,los} \approx \sigma^2_{\rm sg,los} + \sigma^2_{\rm gal,z}\cos^2 i, \tag{20}$$

minimizing contamination from bulk gas motions in the plane. Our gradient-subtracted velocity dispersion $\sigma_{\rm gs,los}$ thus removed the second term (in-plane bulk gravitational motions) but kept the first term (turbulent self-gravitational motions) and last term (vertical random gravitational motions) on the right-hand side of equation (19). However, as we will demonstrate below, the $\sigma^2_{\rm gal,z}\cos^2 i$ term is negligible compared to $\sigma^2_{\rm sg,los}$ in NGC 4429 and can thus safely be ignored, so that $\sigma_{\rm gs,los} \approx \sigma_{\rm sg,los}$ in NGC 4429. Using our newly derived $\sigma_{\rm gs,los}$ measure, we thus revisit the scaling relations of Fig. 9 in Fig. 12.

5.4 Cloud scaling relations using the gradient-subtracted velocity dispersion

The left-hand panel of Fig. 12 (data points and the black solid line) presents the size–linewidth relation based on our $\sigma_{\rm gs,los}$ measure for the 141 spatially resolved clouds of NGC 4429. We now find the size–$\sigma_{\rm gs,los}$ correlation to be rather weak, with a Spearman rank coefficient of 0.25. However, compared with the size–linewidth relation using $\sigma_{\rm obs,los}$, it appears to better follow the relation of the MW disc clouds (the black-dashed line in the left-hand panel of Fig. 12). Indeed, the data points seem to cluster around the MW disc scaling law (Solomon et al. 1987), although there is a large scatter. A weak size–linewidth relation has also been inferred in other galaxies (e.g. Hughes et al. 2013; Utomo et al. 2015), but a small dynamic range and the relatively large uncertainties of our $\sigma_{\rm gs,los}$ measurements probably at least partially explain the poor correlation.

We find a nearly linear correlation between the $\sigma_{\rm gs,los}$-derived virial masses,

$$M_{\rm gs,vir} \equiv \frac{\sigma^2_{\rm gs,los} R_{\rm c}}{b_{\rm s} G} \tag{21}$$

(see equation 7), and the CO-derived gaseous masses $M_{\rm gas}$ of the spatially resolved clouds (the black solid line in the middle panel of Fig. 12), where we have again assumed $b_{\rm s} = \frac{1}{5}$ (spherical homogeneous clouds):

$$\log\left(\frac{M_{\rm gs,vir}}{\rm M_\odot}\right) = (-1.36 \pm 0.28) + (1.28 \pm 0.06)\,\log\left(\frac{M_{\rm gas}}{\rm M_\odot}\right). \tag{22}$$

A lognormal fit to the distribution of the resulting virial parameters,

$$\alpha_{\rm gs,vir} \equiv \frac{M_{\rm gs,vir}}{M} = \frac{M_{\rm gs,vir}}{M_{\rm gas}}, \tag{23}$$

shown as an inset in the middle panel of Fig. 12, yields a mean $\langle\alpha_{\rm gs,vir}\rangle = 1.28 \pm 0.04$ and a standard deviation of 0.15 dex. No systematic variation is observed in the virial parameter $\alpha_{\rm gs,vir}$ for clouds over a wide range of galactocentric distances.

The right-hand panel of Fig. 12 shows the comparison between $\sigma_{\rm gs,los} R_{\rm c}^{-1/2}$ and the gaseous mass surface density $\Sigma_{\rm gas}$ for the spatially resolved clouds. The data points are distributed along the black solid diagonal line, suggesting an SVE. Therefore, when the contamination of in-plane bulk motions is removed, the clouds in NGC 4429 do seem to reach a state of virial equilibrium.

A full determination of the internal equilibrium state of clouds regulated by self-gravity (i.e. the first term in brackets on the right-hand side of equation 18) requires a knowledge of $\sigma_{\rm sg,los}$ rather than $\sigma_{\rm gs,los}$. However, we can still gain important insights from Fig. 12. First, our measured $\sigma^2_{\rm gs,los}$ should be strongly dominated by $\sigma^2_{\rm sg,los}$, i.e. $\sigma^2_{\rm sg,los} \gg \sigma^2_{\rm gal,z}\cos^2 i$ and thus $\sigma^2_{\rm gs,los} \approx \sigma^2_{\rm sg,los}$ (see equation 20), otherwise (if $\sigma^2_{\rm gal,z}\cos^2 i$ were to contribute significantly to $\sigma^2_{\rm gs,los}$) the scaling relations presented in Fig. 12 would depend on the galaxy's inclination angle and the trend seen in Fig. 12 (suggesting a state of gravitational equilibrium) would turn out to be merely a coincidence. But we note that a similar result was obtained in another ETG. Indeed, NGC 4526 revealed a good agreement between the $\sigma_{\rm gs,los}$-derived virial masses and the CO-derived gaseous masses ($\langle\alpha_{\rm gs,vir}\rangle = 0.99 \pm 0.02$), and similarly a $\sigma_{\rm gs,los} R_{\rm c}^{-1/2}$–$\Sigma_{\rm gas}$ correlation as expected from virial equilibrium (Utomo et al. 2015). We thereby consider that the most likely explanation of our results in Fig. 12

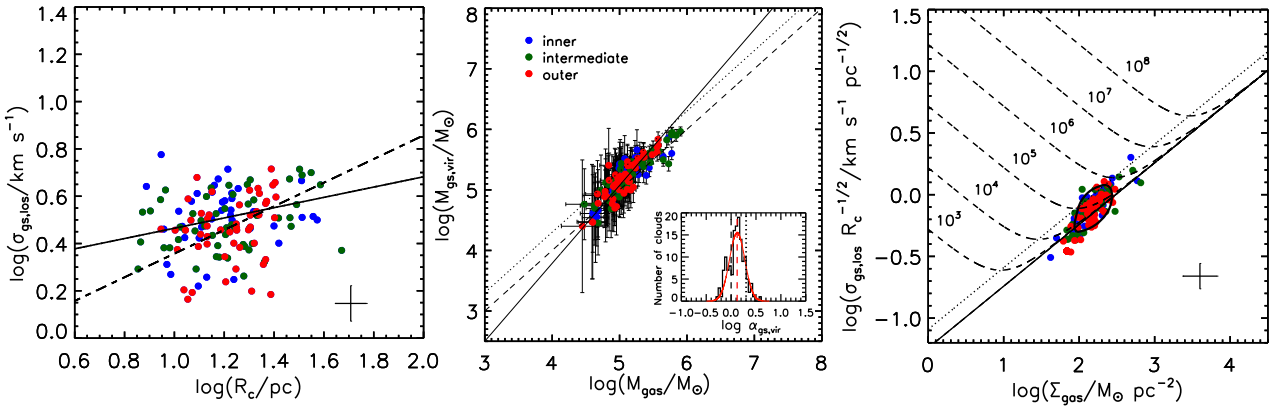

Figure 12. Same as Fig. 9, but using our gradient-subtracted measure of velocity dispersion $\sigma_{\rm gs,los}$.

(and the results of Utomo et al. 2015) is that $\sigma^2_{\rm gs,los}$ is dominated by $\sigma^2_{\rm sg,los}$ (which is assumed isotropic and thus independent of the galaxy inclination angle) and that an internal gravitational equilibrium has been achieved through self-gravity. This assumption is particularly reasonable in NGC 4429, as in any case only a very small part of $\sigma^2_{\rm gal,z}$ can contribute to $\sigma^2_{\rm gs,los}$ considering its high disc inclination ($i = 68^\circ$ so $\cos^2 i \approx 0.1$).

If $\sigma^2_{\rm gs,los} \approx \sigma^2_{\rm sg,los}$, then the left-hand panel of Fig. 12 seems to suggest that the clouds' internal turbulent motions associated with self-gravity follow the classical size–linewidth relation of MW clouds, despite a large scatter. This supports the traditional interpretation of turbulent motions as the origin of the size–linewidth relation (e.g. Mac Low & Klessen 2004; Ballesteros-Paredes et al. 2006, 2007, and references therein) that emerges entirely as a consequence of the gas self-gravity (Camacho et al. 2016; Ibáñez-Mejía et al. 2016). The middle panel of Fig. 12 then implies that $M_{\rm gas} \approx M_{\rm sg,vir}$, i.e. that GMCs attain approximate virial balance between their internal turbulent kinetic energies and their self-gravitational energies. The fact that the mean $\alpha_{\rm gs,vir}$ is slightly larger than one ($\langle\alpha_{\rm gs,vir}\rangle = 1.28 \pm 0.04$) may be due to contamination of $\sigma^2_{\rm gs,los}$ by the $\sigma^2_{\rm gal,z}\cos^2 i$ term. Indeed, in Section 6.4 we will show that the motions induced by (external) gravity contribute around 20 per cent of the total $\sigma^2_{\rm gs,los}$. The right-hand panel of Fig. 12 then further indicates that an internal virialization has been roughly achieved by self-gravity. In other words, the gravitational potential defined by the mass of a cloud is matched by the kinetic energy induced by self-gravity. In this case ($M_{\rm gas} \approx M_{\rm sg,vir}$), we have

$$\sigma^2_{\rm sg,los} \approx \pi b_{\rm s} R_{\rm c} G \Sigma_{\rm gas} \tag{24}$$

(see equation 7), and $\alpha_{\rm sg,vir} \equiv \frac{M_{\rm sg,vir}}{M_{\rm gas}} \approx 1$ (where $\alpha_{\rm sg,vir}$ is the virial parameter set purely by a cloud's self-gravity), as has been suggested by many previous studies of self-gravitating clouds (e.g. equation 10 in Heyer et al. 2009).

We note that this internal virial equilibrium is established by self-gravity despite the presence of an external galactic potential, which seems to support our previous assumption that the motions due to self-gravity emerge independently of the background galactic potential. For more discussion of how a virial equilibrium is established through the balance of turbulent kinetic and self-gravitational energy, see Meidt et al. (2018).

5.5 Role of external gravity

The contribution of external gravity to a cloud's gravitational energy budget ($E_{\rm ext}$) is given by the second term in brackets on the right-hand side of equation 18:

$$E_{\rm ext} \approx \underbrace{M\left(\sigma^2_{\rm gal,z} - b_{\rm e}\nu_0^2 Z_{\rm c}^2\right)}_{\text{external, vertical direction}} + \underbrace{M\left(\sigma^2_{\rm gal,r} + \sigma^2_{\rm gal,t} + b_{\rm e}\left(T_0 - 2\Omega_0^2\right)R_{\rm c}^2\right)}_{\text{external, plane}}. \tag{25}$$

If $E_{\rm ext} > 0$, external gravity acts against self-gravity and makes the cloud less bound. If $E_{\rm ext} < 0$, external gravity acts with self-gravity and contributes to the collapse of the cloud. If $E_{\rm ext} \approx 0$, the effect of external gravity can be ignored. A more general form of $E_{\rm ext}$ for a homogeneous ellipsoidal cloud is provided in Appendix A (equation A12). We can split $E_{\rm ext}$ into two independent parts, one in the vertical direction ($E_{\rm ext,z}$) and one in the plane ($E_{\rm ext,plane}$), and consider them in turn.

5.5.1 Vertical direction

The contribution of the external potential to the gravitational energy budget of the cloud in the vertical direction is

$$E_{\rm ext,z} \approx M\left(\sigma^2_{\rm gal,z} - b_{\rm e}\nu_0^2 Z_{\rm c}^2\right). \tag{26}$$

It is similar to the vertical hydrostatic equilibrium equation of a gaseous disc (e.g. equation 3 in Koyama & Ostriker 2009). If it is positive, the cloud will be disrupted in the vertical direction, but if it is negative, the cloud will collapse in the vertical direction. However, as neither $\sigma_{\rm gal,z}$ nor $Z_{\rm c}$ can be measured directly from our observations, we cannot really assess the vertical equilibrium state of the clouds. But if we make the common assumption that vertical equilibrium is satisfied on a cloud scale, i.e. that the vertical contribution of external gravity to the net energy budget of a cloud is negligible [i.e. $M(\sigma^2_{\rm gal,z} - b_{\rm e}\nu_0^2 Z_{\rm c}^2) \approx 0$], then we can derive a relation between $\sigma_{\rm gal,z}$ and $Z_{\rm c}$:

$$\sigma^2_{\rm gal,z} \approx b_{\rm e}\nu_0^2 Z_{\rm c}^2. \tag{27}$$

The measured scale heights $Z_{\rm c}$ of clouds in edge-on disc galaxies can thus be used to determine their unobservable vertical velocity dispersions $\sigma_{\rm gal,z}$, or conversely the measured line-of-sight velocity dispersions $\sigma_{\rm gal,z}$ of clouds in face-on galaxies can be used to determine the unobservable scale heights $Z_{\rm c}$, as suggested by Koyama

& Ostriker (2009). In our work, we can estimate the value of $\sigma_{\rm gal,z}$ from the deviation of $\sigma_{\rm gs,los}$ from $\sigma_{\rm sg,los}$, and then infer a cloud's scale height (combining equations 20 and 27; see Section 6.4). We note that our derived $\sigma_{\rm gal,z}$–$Z_{\rm c}$ correlation is different from the one derived via the epicyclic approximation by Meidt et al. (2018), by a factor of $b_{\rm e}$ ($\sigma^2_{\rm gal,z} \approx \nu_0^2 Z_{\rm c}^2$ in Meidt et al. 2018). This is because we assumed a spherical cloud with a radial mass volume density distribution [i.e. $\rho(r) \propto r^{-\psi}$] while Meidt et al. (2018) assumed a cloud with an exponential vertical mass volume density distribution [i.e. $\rho(z) \propto \exp(-z)$]. Overall, to retain vertical hydrostatic equilibrium on a cloud scale, the gravitationally induced vertical motions ($\sigma_{\rm gal,z}$) need to balance the vertical weight of the background galaxy.

We note here that assuming vertical equilibrium for the clouds goes against our stated aim of *inferring* whether the clouds are indeed in equilibrium directly from measurements. However, galaxies are highly symmetric vertically and there is no bulk motion in the vertical direction, and we will show below that we do not need to assume the clouds are in equilibrium in the plane. We therefore keep moving forward with our plan, even if it can only be partially achieved.

5.5.2 Plane

The contribution of the external potential to the gravitational energy budget of a cloud in the plane is

$$E_{\rm ext,plane} \approx M\left(\sigma^2_{\rm gal,r} + \sigma^2_{\rm gal,t} + b_{\rm e}\left(T_0 - 2\Omega_0^2\right)R_{\rm c}^2\right). \tag{28}$$

The orbital angular velocity Ω_0 and the tidal acceleration parameter T_0 at the cloud's CoM can be derived from our gas dynamical model (see Section 4.2 and Fig. 10) and they are listed for each cloud in Table 3. A more general form of $E_{\rm ext,plane}$ for a homogeneous ellipsoidal cloud is provided in Appendix A (equation A10). The term $b_{\rm e}(T_0 - 2\Omega_0^2)R_{\rm c}^2$ indicates the effective potential energy of galactic gravity and the centrifugal force (see Appendix A for more details). We find that galactic gravity and the centrifugal force act as a binding force overall, as the corresponding energy $b_{\rm e}(T_0 - 2\Omega_0^2)MR_{\rm c}^2$ is negative in all cases (the function $T - 2\Omega^2$ is generally negative except in the very centre, $R_{\rm gal} \lesssim 40$ pc, where there is no cloud; see Fig. 10). On the other hand, clouds are supported against collapse by the gravitationally induced gas motions in the plane, whose kinetic energy is $\frac{1}{2}M(\sigma^2_{\rm gal,r} + \sigma^2_{\rm gal,t})$. The question then is which of the binding energy of galactic gravity plus the centrifugal force or the kinetic energy of gravitational motions is more important, i.e. whether $E_{\rm ext,plane} < 0$ or $E_{\rm ext,plane} > 0$ (or $E_{\rm ext,plane} = 0$).

As suggested by equation (28), a full derivation of $E_{\rm ext,plane}$ requires knowledge of $\sigma_{\rm gal,r}$ and $\sigma_{\rm gal,t}$, the RMS velocities of gravitationally induced motions in the plane. Although $\sigma_{\rm gal,r}$ and $\sigma_{\rm gal,t}$ cannot be obtained directly from observations, we can nevertheless glean some information about them from the observed quantities $\sigma_{\rm obs,los}$ and $\sigma_{\rm gs,los}$. Indeed, if we assume the gas motions induced by the galactic potential to be isotropic in the plane (i.e. $\sigma_{\rm gal,r} = \sigma_{\rm gal,t}$), the RMS velocities of the in-plane gas motions due to external gravity can easily be derived by combining equations (19) and (20):

$$\sigma^2_{\rm gal,r} = \sigma^2_{\rm gal,t} \approx \frac{\sigma^2_{\rm obs,los} - \sigma^2_{\rm gs,los}}{\sin^2 i}. \tag{29}$$

Substituting equation (29) into equation (28), we find the net contribution of external gravity to the gravitational budget of the clouds in NGC 4429 to be positive in most cases (i.e. $E_{\rm ext,plane} > 0$). Therefore, the main effect of the external gravity on the clouds of NGC 4429 is to make them less bound (in the plane).

Table 3. Derived properties of the clouds in NGC 4429.

ID	Ω_0 (km s^{-1} pc^{-1})	T_0 (km s^{-1} pc^{-1})^2	$\sigma_{\rm eff,los}$ (km s^{-1})	$\log\left(\frac{\rho_{*,0}}{\rm M_\odot\ pc^{-3}}\right)$
1	0.68 ± 0.01	0.75 ± 0.04	...	1.26
2	0.71 ± 0.01	0.57 ± 0.05	3.38 ± 1.79	1.33
3	0.72 ± 0.01	0.67 ± 0.05	4.98 ± 1.13	1.34
4	0.76 ± 0.02	0.67 ± 0.06	2.15 ± 1.93	1.41
5	0.80 ± 0.02	0.67 ± 0.08	2.35 ± 2.63	1.47
6	0.69 ± 0.01	0.60 ± 0.04	3.22 ± 1.16	1.29
7	0.67 ± 0.01	0.74 ± 0.04	4.31 ± 1.00	1.26
8	0.81 ± 0.02	0.69 ± 0.09	1.83 ± 2.79	1.50
9	0.75 ± 0.02	0.65 ± 0.06	...	1.39
10	0.89 ± 0.03	0.81 ± 0.14	2.97 ± 1.89	1.59
11	0.68 ± 0.01	0.71 ± 0.04	...	1.27
12	0.72 ± 0.01	0.59 ± 0.05	...	1.34
13	0.83 ± 0.02	0.76 ± 0.10	2.24 ± 2.29	1.52
14	0.95 ± 0.04	0.95 ± 0.20	2.52 ± 1.93	1.64
15	0.77 ± 0.02	0.67 ± 0.06	1.62 ± 1.97	1.43
16	0.75 ± 0.02	0.66 ± 0.06	...	1.40
17	0.81 ± 0.02	0.69 ± 0.09	...	1.50
18	0.84 ± 0.02	0.68 ± 0.10	3.63 ± 1.71	1.53
19	0.63 ± 0.01	0.72 ± 0.03	5.58 ± 2.18	1.18
20	0.90 ± 0.03	0.83 ± 0.15	2.51 ± 2.10	1.60
...	...	...	...	...
217	0.65 ± 0.01	0.67 ± 0.03	1.58 ± 0.94	1.21

Note. Clouds with no $\sigma_{\rm eff,los}$ entry are unresolved spatially. Calculations of $\sigma_{\rm eff,los}$ assume $b_{\rm e} = \frac{1}{5}$ (spherical homogeneous clouds). All uncertainties are quoted at the 1σ level, and those of $\sigma_{\rm eff,los}$ have been propagated from the uncertainties of both observed and modelled quantities (see equation 38). As noted in the text, the uncertainty of the adopted distance D to NGC 4429 was not propagated through the tabulated uncertainties of the quantity $\sigma_{\rm eff,los}$. This is because an error on the distance to NGC 4429 translates to a systematic (rather than random) scaling of some of the measured quantities (no effect on the others), here $R_{\rm c} \propto D$, $\Omega_0 \propto D^{-1}$ and $T_0 \propto D^{-2}$ in equation (38). Oort's constants A and B can be derived using respectively $A = \frac{T}{4\Omega}$ and $B = \frac{T}{4\Omega} - \Omega$. Table 3 is available in its entirety in machine-readable form in the electronic edition.

5.5.3 Effective parameters

Our MVT (equation 18) can be written simply as

$$\begin{aligned}\frac{\ddot{I}}{2} &\approx \left(3M\sigma^2_{\rm sg,los} - 3b_{\rm s}GM^2/R_{\rm c}\right) + E_{\rm ext}\\ &\approx \frac{3b_{\rm s}GM^2}{R_{\rm c}}\left(\frac{\sigma^2_{\rm sg,los}R_{\rm c}}{b_{\rm s}GM} + \frac{E_{\rm ext}}{3b_{\rm s}GM^2/R_{\rm c}} - 1\right)\end{aligned} \tag{30}$$

(see equation 25). However,

$$\alpha_{\rm sg,vir} \equiv \frac{\sigma^2_{\rm sg,los}R_{\rm c}}{b_{\rm s}GM} \tag{31}$$

(see equation 13), the traditional virial parameter regulated by self-gravity only, and we define

$$\beta \equiv \frac{E_{\rm ext}}{3b_{\rm s}GM^2/R_{\rm c}}, \tag{32}$$

the ratio between the contribution of external gravity and the (absolute value of the) cloud's self-gravitational energy ($|U_{\rm sg}| = 3b_{\rm s}GM^2/R_{\rm c}$), so that

$$\frac{\ddot{I}}{2} \approx \frac{3b_{\rm s}GM^2}{R_{\rm c}}(\alpha_{\rm sg,vir} + \beta - 1). \tag{33}$$

This naturally leads us to define an effective virial parameter

$$\alpha_{\rm eff,vir} \equiv \alpha_{\rm sg,vir} + \beta \tag{34}$$

such that

$$\frac{\ddot{I}}{2} \approx \frac{3b_s GM^2}{R_c}(\alpha_{\rm eff,vir} - 1). \quad (35)$$

Thus, just like the standard virial parameter, this effective virial parameter informs on the dynamical stability of a cloud. If $\alpha_{\rm eff,vir} \approx 1$, the cloud is gravitationally bound and in virial equilibrium even in the presence of the external (i.e. galactic) gravitational potential. If $\alpha_{\rm eff,vir} \gg 1$, the cloud is unlikely to be bound (i.e. it is transient unless confined by other forces). If $\alpha_{\rm eff,vir} \lesssim 1$, the molecular cloud is likely to collapse. For clouds that are (marginally) gravitationally bound, we again require $\alpha_{\rm eff,vir} \leq \alpha_{\rm vir,crit} = 2$ (Kauffmann et al. 2013, 2017), or equivalently $\beta \leq 1$ if an internal virial equilibrium is established by self-gravity (i.e. if $\alpha_{\rm sg,vir} \approx 1$; see equation 34).

Equivalently, from equation (13), we can define an effective velocity dispersion

$$\sigma^2_{\rm eff,los} = \alpha_{\rm eff,vir}\, b_s GM/R_c, \quad (36)$$

and thus our modified virial equation (equation 18) can be simplified to

$$\frac{\ddot{I}}{2} \approx \left(3M\sigma^2_{\rm eff,los} - 3b_s GM^2/R_c\right). \quad (37)$$

The parameters $\alpha_{\rm eff,vir}$ (via equation 35) or equivalently $\sigma_{\rm eff,los}$ (via equation 37) thus embody our MVT and offer a straightforward method to test the gravitational boundedness of a cloud in the presence of an external (i.e. galactic) gravitational field.

Of course, our expressions are of no use in practice if the external contribution $E_{\rm ext}$ cannot be evaluated (see equation 25). Indeed, without knowledge of $\sigma_{\rm gal,z}$, $\sigma_{\rm gal,r}$, and $\sigma_{\rm gal,t}$, none of β, $\alpha_{\rm eff,vir}$, or $\sigma_{\rm eff,los}$ can be evaluated. However, by making increasingly stringent assumptions, we show in Appendix B that it is possible to evaluate all these quantities from observable quantities alone. We thus briefly summarize those assumptions and their consequences here, but refer to Appendix B for detailed calculations.

First, we assume clouds are in vertical hydrostatic equilibria, i.e. $\sigma^2_{\rm gal,z} \approx b_e \nu_0^2 Z_c^2$ (equation 27), so that the contribution of the external potential to the gravitational energy budget of each cloud in the vertical direction vanishes, i.e. $E_{\rm ext,z} \approx 0$ (see equation 26). Secondly, we assume the motions associated with external gravity to be isotropic in the plane, i.e. $\sigma^2_{\rm gal,r} = \sigma^2_{\rm gal,t} \approx \frac{\sigma^2_{\rm obs,los} - \sigma^2_{\rm gs,los}}{\sin^2 i}$ (equation 29). Thirdly, we assume $\sigma^2_{\rm sg,los} \approx \sigma^2_{\rm gs,los}$ (or equivalently $\sigma^2_{\rm sg,los} \gg \sigma^2_{\rm gal,z}\cos^2 i$; see equation 20) and thus $\alpha_{\rm sg,vir} \approx \alpha_{\rm gs,vir}$. As shown in Appendix B, all three assumptions taken together lead to

$$E_{\rm ext} \approx M\left[\frac{2\left(\sigma^2_{\rm obs,los} - \sigma^2_{\rm gs,los}\right)}{\sin^2 i} + b_e\left(T_0 - 2\Omega_0^2\right)R_c^2\right],$$

$$\sigma^2_{\rm eff,los} \approx \sigma^2_{\rm gs,los} + \frac{1}{3}\left[\frac{2\left(\sigma^2_{\rm obs,los} - \sigma^2_{\rm gs,los}\right)}{\sin^2 i} + b_e\left(T_0 - 2\Omega_0^2\right)R_c^2\right], \text{ and}$$

$$\alpha_{\rm eff,vir} \approx \frac{\sigma^2_{\rm gs,los} R_c}{b_s GM} + \frac{R_c}{3b_s GM}\left[\frac{2\left(\sigma^2_{\rm obs,los} - \sigma^2_{\rm gs,los}\right)}{\sin^2 i} + b_e\left(T_0 - 2\Omega_0^2\right)R_c^2\right] \quad (38)$$

(see equations 25, 36, 34, 23, 21, and 32). More general forms for a homogeneous ellipsoidal cloud are provided in Appendix B. These equations (38) represent our final MVT, whose power lies in the fact that all of $E_{\rm ext}$, $\sigma_{\rm eff,los}$, and $\alpha_{\rm eff,vir}$ can be evaluated directly from observations. Indeed, as mentioned previously, the measured M ($M_{\rm gas}$), R_c, $\sigma_{\rm obs,los}$, and $\sigma_{\rm gs,los}$ are listed for each spatially resolved cloud in Table 1, while Ω_0, T_0, and the resulting $\sigma_{\rm eff,los}$ (and thus $\alpha_{\rm eff,vir}$; see equation 36) are listed in Table 3.

The first term on the right-hand side of equation (38; except for $E_{\rm ext}$) comprises the gas turbulent motions associated with a cloud's self-gravity, the second term denotes the gravitational motions associated with external gravity in the plane, and the last term encompasses the external/galactic forces on the cloud.

An extended virial theorem including the background tidal field was formulated by Chen et al. (2016), but they only evaluated two representative cases, namely a non-rotating cloud ($\sigma^2_{\rm eff,los} = \sigma^2 + b_e(T_0 - 2\Omega_0^2)R_c^2/3$; equation 17 in their paper) and a tidally locked cloud ($\sigma^2_{\rm eff,los} = \sigma^2 + b_e T_0 R_c^2/3$; equation 18 in their paper). Our derived MVT is valid for more general cases. In fact, we obtain the same results as Chen et al. (2016) for their two particular cases. For a non-rotating cloud, $\sigma_{\rm gal,r} = \sigma_{\rm gal,t} = 0$, and we derive $\sigma^2_{\rm eff,los} = \sigma^2_{\rm sg,los} + b_e(T_0 - 2\Omega_0^2)R_c^2/3$. For a tidally locked cloud (i.e. Oort's constants $A = 0$ and $B = \Omega$), $(\sigma^2_{\rm gal,r} + \sigma^2_{\rm gal,t}) \approx 2b_e\Omega_0^2 R_c^2$ [as $\sigma^2_{\rm gal,r} \approx \sigma^2_{\rm gal,r} \approx b_e\Omega_0^2 R_c^2$; see equation (B23) in Appendix B], and we derive $\sigma^2_{\rm eff,los} = \sigma^2_{\rm sg,los} + b_e T_0 R_c^2/3$. We note that the velocity dispersion σ^2 used by the extended virial theorem of Chen et al. (2016) should be the internal turbulent velocity dispersion rather than the observed (i.e. total) velocity dispersion.

Overall, to take into account the influence of external gravity on the dynamical state of a cloud, one should use the effective virial parameter $\alpha_{\rm vir,eff}$ and effective velocity dispersion $\sigma_{\rm eff,los}$. The latter quantifies the net kinetic energy that balances the cloud's (self-)gravitational potential energy. The kinetic energy obtained using $\sigma_{\rm eff,los}$ includes the cloud's internal turbulent kinetic energy due to self-gravity as well as the contributions from the external gravity. If $\alpha_{\rm eff,vir} > \alpha_{\rm sg,vir}$ or $\sigma^2_{\rm eff,los} > \sigma^2_{\rm sg,los}$, external gravity acts against self-gravity and makes the cloud less bound (i.e. $E_{\rm ext} > 0$). If $\alpha_{\rm eff,vir} < \alpha_{\rm sg,vir}$ or $\sigma^2_{\rm eff,los} < \sigma^2_{\rm sg,los}$, external gravity acts with self-gravity and contributes to the cloud's confinement and/or collapse (i.e. $E_{\rm ext} < 0$). If $\alpha_{\rm eff,vir} = \alpha_{\rm sg,vir}$ or $\sigma^2_{\rm eff,los} = \sigma^2_{\rm sg,los}$, then external gravity has no effects on the cloud's dynamical state (i.e. $E_{\rm ext} = 0$). Therefore, the results presented in Figs 9 and 12, which, respectively, adopt $\sigma_{\rm obs,los}$ and $\sigma_{\rm gs,los}$, do not reflect the real dynamical states of the NGC 4429 clouds. Specifically, $\sigma_{\rm obs,los}$ embodies gas motions associated with self-gravity and external gravity, but it ignores the extra binding energy provided by galactic forces and the centrifugal force [i.e. the term $b_e(T_0 - 2\Omega_0^2)M R_c^2$ in equations (18), (25), and (28) that is negative in almost all cases], so it overestimates the effect of external gravity on the clouds. Conversely, $\sigma_{\rm gs,los}$ only reflects gas motions associated with self-gravity, so it does not include the contribution of external gravity to a cloud's gravitational energy budget.

5.6 Cloud scaling relations using the effective velocity dispersion

In consequence, we revisit yet again the three scaling relations that describe the dynamical states of the clouds in NGC 4429, this time using the effective velocity dispersion $\sigma_{\rm eff,los}$ defined in equations (38). In most cases, our derived $\sigma_{\rm eff,los}$ is larger than the gradient-subtracted velocity dispersion $\sigma_{\rm gs,los}$, and in all cases it is smaller than the observed velocity dispersion $\sigma_{\rm obs,los}$ (see Fig. 11). This implies that external gravity generally makes the clouds less bound. We nevertheless note that we find a few clouds where $\sigma_{\rm eff,los}$ is smaller than $\sigma_{\rm gs,los}$, suggesting external gravity contributes to the cloud's confinement and/or collapse in these few cases. As expected in equation (38), these clouds all have $\sigma_{\rm gs,los}$ nearly equal to $\sigma_{\rm obs,los}$, and thus low velocity gradients of 0.1–0.2 km s^{-1} pc^{-1}.

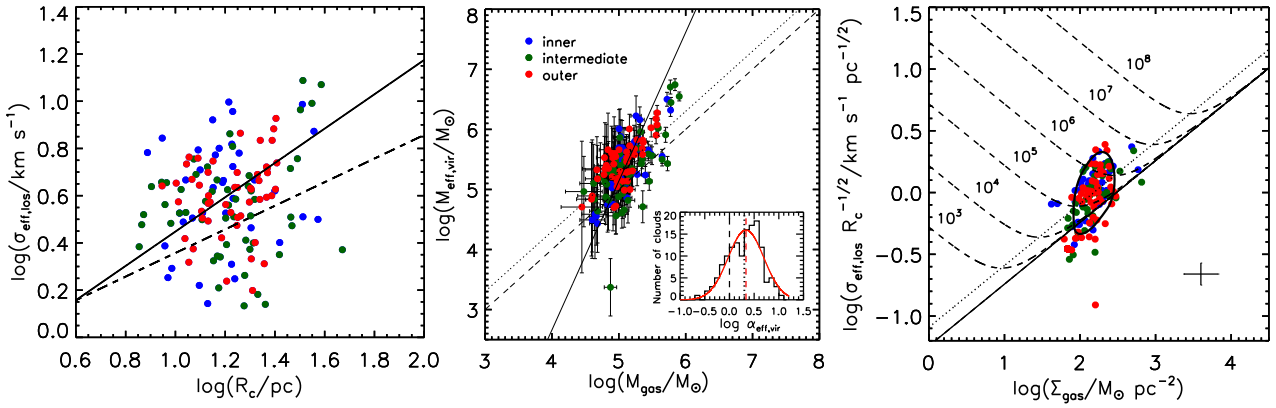

Figure 13. Same as Figs 9 and 12, but using our effective measure of velocity dispersion $\sigma_{\rm eff,los}$ for axisymmetric clouds.

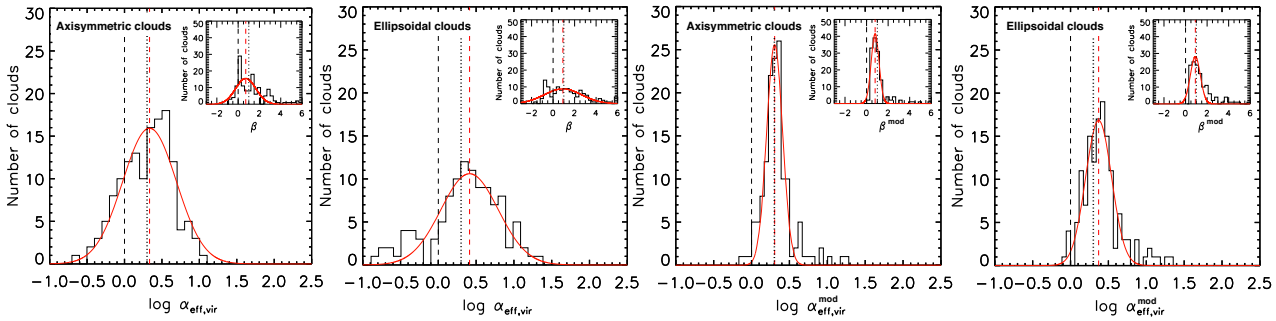

Figure 14. Distributions of the effective virial parameter $\alpha_{\rm vir,eff}$ and the external energy parameter β (insets) of the 141 spatially resolved clouds of NGC 4429, calculated from both observations (first and second panels; see Section 5.5) and our shear model (third and fourth panels; see Section 6.1), assuming both axisymmetric (first and third panels) and ellipsoidal (second and fourth panels) clouds. Lognormal ($\alpha_{\rm vir,eff}$) and normal (β) fits are overlaid (the red solid lines). The vertical red-dashed lines indicate the means of the fits, while the vertical black-dashed and dotted lines indicate $\alpha_{\rm vir} = 1$ and 2 ($\beta = 0$ and 1), respectively.

The left-hand panel of Fig. 13 (data points and the black solid line) presents the $\sigma_{\rm eff,los}$–$R_{\rm c}$ relation for the 141 spatially resolved clouds of NGC 4429, where we have assumed $b_{\rm e} = \frac{1}{5}$ (homogeneous clouds). The relation appears to have a slightly steeper slope (0.72 ± 0.18) than that of MW clouds (0.5 ± 0.05; Solomon et al. 1987), but the correlation is very weak (with a Spearman rank correlation coefficient of 0.13).

The virial masses of the spatially resolved clouds derived using $\sigma_{\rm eff,los}$, referred to as effective virial masses

$$M_{\rm eff,vir} \equiv \frac{\sigma^2_{\rm eff,los} R_{\rm c}}{b_{\rm s} G} \tag{39}$$

(see equation 7), are compared to the CO-derived gaseous masses $M_{\rm gas}$ in the middle panel of Fig. 13, where we have again assumed $b_{\rm s} = \frac{1}{5}$ (spherical homogeneous clouds). A linear fit between effective virial and gaseous mass yields (the black solid line in the middle panel of Fig. 13)

$$\log\left(\frac{M_{\rm eff,vir}}{\rm M_\odot}\right) = (-7.25 \pm 1.54) + (2.47 \pm 0.30) \log\left(\frac{M_{\rm gas}}{\rm M_\odot}\right). \tag{40}$$

A lognormal fit to the distribution of the resulting effective virial parameters,

$$\alpha_{\rm eff,vir} \equiv \frac{M_{\rm eff,vir}}{M} = \frac{M_{\rm eff,vir}}{M_{\rm gas}} \tag{41}$$

(see also equation 36), shown in the first panel of Fig. 14, yields a mean $\langle \alpha_{\rm eff,vir} \rangle = 2.15 \pm 0.12$ and a standard deviation of 0.35 dex. This mean is higher than $\langle \alpha_{\rm sg,vir} \rangle \approx \langle \alpha_{\rm gs,vir} \rangle = 1.28 \pm 0.04$ (see Section 5.4), suggesting that the main effect of external gravity on the clouds is to make them less bound. However, since many NGC 4429 clouds have a mean effective virial parameter close to the critical value regarded as the boundary between gravitationally bound and unbound clouds (Kauffmann et al. 2013, 2017), i.e. $\langle \alpha_{\rm eff,vir} \rangle \approx \alpha_{\rm vir,crit} = 2$, the clouds should still be marginally gravitationally bound.

The inset in the first panel of Fig. 14 shows the distribution of the measured β (equation 32). A Gaussian fit yields a mean $\langle \beta \rangle = 0.71 \pm 0.33$ and a standard deviation of 1.05. Given these $\beta \approx 1$, the contribution of external gravity to each clouds' energy budget is generally significant, on average of the order of (and frequently exceeding) the self-gravitational energy (see also equation 34). We will discuss this aspect further in Section 6.2. However, we note immediately that a noticeable fraction of spatially resolved clouds (25/141 or $\approx$ 18 per cent) have $\beta \leq 0$. These negative β could be due to observational uncertainties, and thus inaccuracies when estimating $\alpha_{\rm eff,vir}$ (or $E_{\rm ext}$), but some clouds may well have their gas motions decoupled from global galaxy rotation. Indeed, we found that clouds with $\beta \leq 0$ have larger discrepancies between their observed and modelled angular momenta (with a median projected angular velocity discrepancy factor of $\approx$1.9 and a median position angle difference of $\approx 24^\circ$; see Section 4.2) than clouds with $\beta > 0$ (with a median projected angular velocity discrepancy factor of $\approx$1.3 and a median position angle difference of $\approx 13^\circ$). It thus seems that clouds with $\beta \leq 0$ only weakly follow the galaxy orbital rotation. These clouds are therefore presumably not as strongly affected by galactic shear and

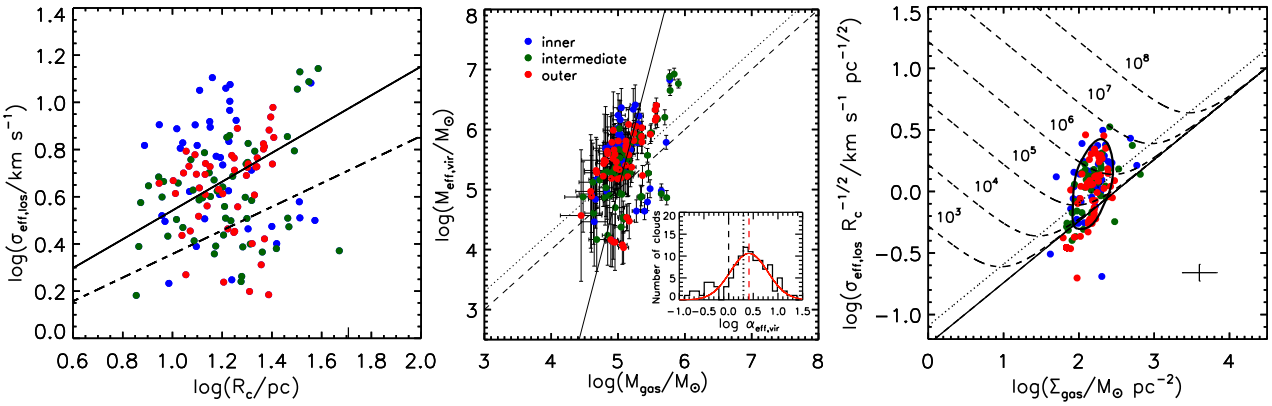

Figure 15. Same as Figs 9, 12, and 13, but using our effective measure of velocity dispersion $\sigma_{\rm eff,los}$ for ellipsoidal clouds.

tidal forces, and they can become more virialized (with $\langle\alpha_{\rm eff,vir}\rangle \approx 0.9$).

The right-hand panel of Fig. 13 shows the $\sigma_{\rm eff,los}R_{\rm c}^{-1/2}$–$\Sigma_{\rm gas}$ relation for the 141 spatially resolved clouds of NGC 4429. The data points are mostly distributed away from the black solid diagonal line (SVE), but they are clustered around the black-dotted diagonal line. This again suggests that, although the NGC 4429 clouds are not virialized, they could be marginally gravitationally bound.

5.7 Cloud scaling relations considering ellipsoidal clouds

By using a single measure of size for each cloud ($R_{\rm c}$; see Section 3.1), our analysis has so far implicitly assumed that each cloud is axisymmetric in the orbital plane. However, the effects of external gravity on a cloud (and its contribution $E_{\rm ext}$ to a cloud's energy budget) also formally depend on the actual shape and position angle of the cloud (see Appendices A and B). To assess the impacts of this assumption, we now assume instead that each cloud has an ellipsoidal geometry, with semi-axis $Z_{\rm c}$ perpendicular to the orbital plane and semimajor axis $X_{\rm c}$ (at a position angle $\phi_{\rm PA}$ with respect to the radial/galactocentric direction) and semiminor axis $Y_{\rm c}$ in the orbital plane.

If an ellipsoidal cloud is homogeneous, Appendices A and B show that equations (38; that assume vertical equilibrium, isotropy in the equatorial plane and $\sigma_{\rm sg,los} \approx \sigma_{\rm gs,los}$) become

$$
\begin{aligned}
E_{\rm ext} &\approx M\left[\frac{2\left(\sigma^2_{\rm obs,los}-\sigma^2_{\rm gs,los}\right)}{\sin^2 i}\right.\\
&\left.+\,b_{\rm e}T_0\left(X_{\rm c}^2\cos^2\phi_{\rm PA}+Y_{\rm c}^2\sin^2\phi_{\rm PA}\right)-b_{\rm e}\Omega_0^2\left(X_{\rm c}^2+Y_{\rm c}^2\right)\right],\\
\sigma^2_{\rm eff,los} &\approx \sigma^2_{\rm gs,los}+\frac{1}{3}\left[\frac{2\left(\sigma^2_{\rm obs,los}-\sigma^2_{\rm gs,los}\right)}{\sin^2 i}\right.\\
&+\,b_{\rm e}T_0\left(X_{\rm c}^2\cos^2\phi_{\rm PA}+Y_{\rm c}^2\sin^2\phi_{\rm PA}\right)\\
&\left.-\,b_{\rm e}\Omega_0^2\left(X_{\rm c}^2+Y_{\rm c}^2\right)\right],\ \text{and}\\
\alpha_{\rm eff,vir} &\approx \frac{\sigma^2_{\rm gs,los}R_{\rm c}}{b_{\rm s}GM}+\frac{R_{\rm c}}{3b_{\rm s}GM}\left[\frac{2\left(\sigma^2_{\rm obs,los}-\sigma^2_{\rm gs,los}\right)}{\sin^2 i}\right.\\
&\left.+\,b_{\rm e}T_0\left(X_{\rm c}^2\cos^2\phi_{\rm PA}+Y_{\rm c}^2\sin^2\phi_{\rm PA}\right)-b_{\rm e}\Omega_0^2\left(X_{\rm c}^2+Y_{\rm c}^2\right)\right].
\end{aligned}
\tag{42}
$$

These equations thus represent our final MVT (equations 38) for the case of a homogenous ellipsoidal cloud.

We note that $X_{\rm c}$, $Y_{\rm c}$, and $\phi_{\rm PA}$ in equations (42) should be measured in the cloud's orbital plane (i.e. the galaxy's equatorial plane) rather than the sky plane. To correct for the effects of inclination, we thus create an image of each cloud deprojected to a face-on view, from which we measure the semimajor and semiminor axes analogously to $R_{\rm c}$ in Section 3.1 and the position angle with respect to the radial/galactocentric direction.

The left-hand panel of Fig. 15 presents the $\sigma_{\rm eff,los}$–$R_{\rm c}$ relation for the 141 spatially resolved clouds of NGC 4429 assuming they are ellipsoidal and $b_{\rm e} = \frac{1}{5}$ (homogeneous clouds). The relation has a slope of 0.62 ± 0.21, consistent with that of axisymmetric clouds (0.72 ± 0.18; see Section 5.6), and is thus again slightly steeper than that of MW clouds (0.5 ± 0.05; Solomon et al. 1987), although the correlation is again very weak (with a Spearman rank correlation coefficient of 0.09).

The effective virial masses of the 141 spatially resolved clouds ($M_{\rm eff,vir} \equiv \sigma^2_{\rm eff,los}R_{\rm c}/b_{\rm s}G$) derived assuming ellipsoidal shapes (see equation 7; where $R_{\rm c}$ is defined as $\sqrt{X_{\rm c}Y_{\rm c}}$) are compared to the CO-derived gaseous masses $M_{\rm gas}$ in the middle panel of Fig. 15. We have again assumed $b_{\rm s_1} = \frac{1}{5}$ (homogeneous clouds), but calculated $b_{\rm s_2}$, that quantifies the effects of the ellipticity, separately for each cloud using the method provided by Bertoldi & McKee (1992; see Appendix A for more details). We find the exact cloud morphology has negligible effects on the quantities regarding the cloud's self-gravity (e.g. $U_{\rm sg}$ and $\alpha_{\rm sg}$), as $b_{\rm s_2}$ is approximately unity ($\langle b_{\rm s_2}\rangle \approx 0.95$). A linear fit between the effective virial and gaseous masses (the black solid line in the middle panel of Fig. 15) yields a slope of 4.27 ± 0.70. A lognormal fit to the distribution of the effective virial parameters ($\alpha_{\rm eff,vir}$) derived assuming ellpsoidal clouds (see equations 41 and 42), shown in the second panel of Fig. 14, yields a mean $\langle\alpha_{\rm eff,vir}\rangle = 2.59 \pm 0.19$ and a standard deviation of 0.38 dex, only slightly larger than that estimated assuming axisymmetric clouds ($\langle\alpha_{\rm eff,vir}\rangle = 2.15 \pm 0.12$; see Section 5.6), and again higher than $\langle\alpha_{\rm sg,vir}\rangle \approx \langle\alpha_{\rm gs,vir}\rangle = 1.28 \pm 0.04$ (see Section 5.4), suggesting that the main effect of external gravity on the clouds is to make them less bound irrespective of their exact shapes.

The inset in the second panel of Fig. 14 shows the distribution of the resulting β for the 141 spatially resolved clouds of NGC 4429, calculated assuming ellipsoidal clouds. A Gaussian fit to the distribution yields a mean $\langle\beta\rangle = 0.91 \pm 0.35$ and a standard deviation of 1.73, again slightly larger than that derived assuming axisymmetric clouds [$\langle\beta\rangle = 0.71 \pm 0.33$; see the first panel of Fig. 14 and

Section 5.6)]. As we shall discuss in Section 6.3, this is primarily due to the radially elongated shapes of the NGC 4429 clouds. The differences are, however, minor, and it is still true that $\langle \alpha_{\rm eff,vir} \rangle \approx \alpha_{\rm vir,crit} = 2$ and $\langle \beta \rangle \approx 1$ for ellipsoidal clouds. Therefore, the evidence remains that the NGC 4429 clouds appear to be marginally gravitationally bound.

The right-hand panel of Fig. 15 shows the $\sigma_{\rm eff,los} R_{\rm c}^{-1/2}$–$\Sigma_{\rm gas}$ relation for the 141 spatially resolved clouds, derived assuming ellipsoidal clouds and $b_{\rm e} = \frac{1}{5}$. Just as for axisymmetric clouds, the data points are generally above the black solid diagonal line (SVE) but are centred on the black-dotted diagonal line. This thus suggests again that, irrespective of their exact shapes, the NGC 4429 clouds are probably not virialized but are likely to be marginally gravitationally bound.

In summary, the dynamical states of the NGC 4429 clouds are regulated by both self-gravity and external (i.e. galactic) gravity. Internal virial equilibria between the clouds' turbulent kinetic energies and their own gravitational energies have been attained, regardless of the presence of external gravity. The additional contribution of external gravity to the clouds' gravitational energy budgets includes two parts: the supporting kinetic energy from gravitational motions ($\frac{1}{2} M \sigma_{\rm gal,z}^2$ in the vertical direction and $\frac{1}{2} M (\sigma_{\rm gal,r}^2 + \sigma_{\rm gal,t}^2)$ in the plane) and the effective potential energy of the galactic and centrifugal forces ($-b_{\rm e} M \nu_0^2 Z_{\rm c}^2$ in the vertical direction and $b_{\rm e}(T_0 - 2\Omega_0^2) M R_{\rm c}^2$ in the plane). If we assume the NGC 4429 clouds are in vertical hydrostatic equilibria (i.e. $E_{\rm ext,z} \approx M \sigma_{\rm gal,z}^2 - b_{\rm e} M \nu_0^2 Z_{\rm c}^2 = 0$), gravitational motions are isotropic in the orbital plane (i.e. $\sigma_{\rm gal,r} = \sigma_{\rm gal,t}$), and $\sigma_{\rm sg,los} \approx \sigma_{\rm gs,los}$, we can calculate the contributions of external gravity to the clouds' energy budgets ($E_{\rm ext}$) directly from the observations. These are positive in most cases and on average of the order of the clouds' self-gravitational energies (i.e. $\beta \equiv \frac{E_{\rm ext}}{|U_{\rm sg}|} \approx 1$). The derived effective virial parameters have a mean of $\approx$2, i.e. $\langle \alpha_{\rm eff,vir} \rangle \approx \alpha_{\rm vir,crit} = 2$. Both results are essentially independent of the exact cloud shapes (i.e. whether we assume axisymmetric or ellpsoidal clouds), suggesting that the NGC 4429 clouds are marginally gravitationally bound due to the combined effects of self-gravity and external gravity.

6 DISCUSSION

6.1 Shear motions and non-zero $E_{\rm ext}$

As gravitational motions appear to play an important role regulating the dynamics and boundedness of the clouds in NGC 4429, we discuss in more depth in this section the clouds' motions driven by the external (i.e. galactic) gravitational forces. As in Appendix A2, we adopt a local Cartesian coordinate system centred on the CoM of each cloud, which both orbits around the galaxy centre with the CoM (with azimuthal velocity $\Omega_0 R_0$) and rotates on itself (with angular velocity Ω_0), such that the $x^{'}$-axis always points in the direction of increasing galactocentric radius and the $y^{'}$-axis always points in the direction of orbital rotation (see Fig. A1). As shown in Appendix A2, in this rotating frame the equations of motions driven by external gravity can be written as

$$\begin{cases} a'_{\rm ext,x'} \approx T_0 x' + 2\Omega_0 v'_{\rm gal,y'}, \\ a'_{\rm ext,y'} \approx -2\Omega_0 v'_{\rm gal,x'}, \end{cases} \tag{43}$$

where $x^{'}$, $v'_{\rm gal,x'}$, and $a'_{\rm ext,x'}$ are the components of the position vector $\vec{d}'_{\rm plane}$, velocity vector $\vec{v}'_{\rm gal}$, and acceleration vector $\vec{a}'_{\rm ext}$ along the $\hat{x}'$-direction, respectively, similarly for $y^{'}$, $v'_{\rm gal,y'}$, and $a'_{\rm ext,y'}$. The $T_0 x^{'}$ term represents the tidal force, while the terms $2\Omega_0 v'_{\rm gal,y'}$ and $-2\Omega_0 v'_{\rm gal,x'}$ represent the Coriolis force.

As discussed in Appendix A2, this set of coupled differential equations has solution

$$\begin{cases} x' = {\rm S}_1 \sin(\kappa_0 t + \varphi) + {\rm S}_2, \\ y' = \dfrac{2\Omega_0}{\kappa_0} {\rm S}_1 \cos(\kappa_0 t + \varphi) - 2A_0 {\rm S}_2 t + {\rm S}_3, \end{cases} \tag{44}$$

where κ_0 is the epicyclic frequency evaluated at the cloud's CoM ($\kappa_0^2 \equiv (R \frac{{\rm d}\Omega^2(R)}{{\rm d}R} + 4\Omega^2(R))|_{R=R_0}$), A_0 is Oort's constant A quantifying shear evaluated at the cloud's CoM ($A_0 \equiv -\frac{R}{2} \frac{{\rm d}\Omega(R)}{{\rm d}R}|_{R=R_0}$), and $\rm S_1$, $\rm S_2$, and $\rm S_3$ (as well as the arbitrary phase φ) are constants that depend on the given boundary (e.g. initial) conditions. Equation (44) shows that the gravitational motions associated with external gravity have two contributions: epicyclic motions around the cloud's CoM (i.e. the 'guiding centre'; see e.g. Meidt et al. 2018), indicated by the trigonometric terms ${\rm S}_1 \sin(\kappa_0 t + \varphi)$ and $\frac{2\Omega_0}{\kappa_0} {\rm S}_1 \cos(\kappa_0 t + \varphi)$, and linear shear motion, indicated by the $-2A_0 {\rm S}_2 t$ term (e.g. Gammie, Ostriker & Jog 1991; Tan 2000; Binney 2020).

It is worth noting that, in a model where all fluid elements of a cloud move on perfectly circular orbits (around the galaxy centre) determined by the galactic potential, the epicyclic amplitudes vanish and the gravitational motions are completely dominated by the shear motions, i.e.

$$\begin{cases} x' = {\rm S}_2, \\ y' = -2A_0 {\rm S}_2 t + {\rm S}_3. \end{cases} \tag{45}$$

Hereafter, we name this model, where all fluid elements of a cloud are assumed to populate perfectly circular orbits determined by the galactic potential, the 'shear model'. We thus define a shear velocity

$$v_{\rm shear} \equiv -2A_0 {\rm S}_2, \tag{46}$$

where $\rm S_2$ is the distance of the fluid element from the cloud's centre along $\hat{x}'$ (see Fig. A1). Interestingly, as we shall demonstrate below, the bulk motions observed in the NGC 4429 clouds appear to be strongly dominated by gravitational shear motions, with little or no evidence of gravitational epicyclic motions, i.e. the fluid elements of the clouds seem to populate nearly circular orbits (around the galaxy centre) determined by the galactic potential.

First, the measured velocity gradients across the spatially resolved clouds of NGC 4429, and the position angles of the rotation axes of these clouds, are both consistent with those predicted by assuming purely circular orbital motions (see Fig. 8 and Section 4.2, where both the measured and modelled quantities are calculated in the sky plane). This provides strong evidence that the bulk motions of the NGC 4429 clouds are dominated by gravitational shear motions.

Secondly, if all fluid elements of a cloud indeed follow circular orbits determined by the galactic potential, then we can predict the RMS velocities of the clouds' gravitational motions in both the radial and azimuthal directions: $(\sigma_{\rm gal,r}^{\rm mod})^2 = b_{\rm e} \Omega_0^2 R_{\rm c}^2$ and $(\sigma_{\rm gal,t}^{\rm mod})^2 = b_{\rm e}(\Omega_0 - 2A_0)^2 R_{\rm c}^2$ (see equations B23 in Appendix B). We can thus also predict their line-of-sight velocity dispersions using equation (19):

$$\begin{aligned} \sigma_{\rm mod,los}^2 &\approx \sigma_{\rm sg,los}^2 + \left(\left(\sigma_{\rm gal,r}^{\rm mod}\right)^2 \sin^2\theta + \left(\sigma_{\rm gal,t}^{\rm mod}\right)^2 \cos^2\theta \right) \sin^2 i \\ &\quad + \sigma_{\rm gal,z}^2 \cos^2 i \\ &\approx \pi b_{\rm s} R_{\rm c} G \Sigma_{\rm gas} \\ &\quad + b_{\rm e} R_{\rm c}^2 \left(\Omega_0^2 \sin^2\theta + (\Omega_0 - 2A_0)^2 \cos^2\theta \right) \sin^2 i, \end{aligned} \tag{47}$$

where we have used $\alpha_{\rm sg,vir} \approx 1$ (and thus $\sigma_{\rm sg,los}^2 \approx \pi b_{\rm s} R_{\rm c} G \Sigma_{\rm gas}$; see equations 24 and 31) and $\sigma_{\rm gal,z}^2 \cos^2 i \approx 0$. We compare in Fig. 16 the observed line-of-sight velocity dispersions $\sigma_{\rm obs,los}$ of the 141 spatially

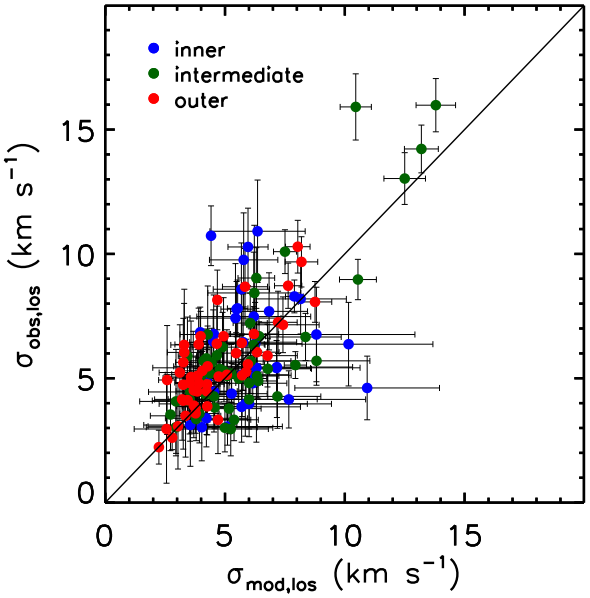

Figure 16. Comparison of the observed and modelled line-of-sight velocity dispersion of the 141 spatially resolved clouds of NGC 4429. Data points are colour-coded by region. The black solid diagonal line shows the 1:1 relation.

resolved clouds of NGC 4429 with those predicted from our shear model $\sigma_{\rm mod,\,los}$. We generally find a good agreement between the two, albeit with a few exceptions. This thus reinforces our inference that the bulk motions of the NGC 4429 clouds are dominated by gravitational shear motions.

Lastly, if all fluid elements of a cloud follow pure epicyclic motions described by the trigonometric terms in equations (44), the cloud is necessarily in virial equilibrium (Meidt et al. 2018) and thus the contribution of external gravity should vanish, i.e. $E_{\rm ext} = 0$ and $\alpha_{\rm eff,vir} \approx \alpha_{\rm sg,vir} \approx 1$. However, $E_{\rm ext}$ (or equivalently β) measured from our observations of spatially resolved clouds are clearly not zero (see Section 5.5), suggesting that the bulk motions within the NGC 4429 clouds cannot be dominated by gravitational epicyclic motions. In turn, we expect the measured $E_{\rm ext}$ (and β) to more closely match those predicted from gravitational shear motions only. As our shear model assumes that all fluid elements of a cloud move on perfectly circular orbits determined by the galactic potential, this model yields (cf. equations 38)

$$\begin{aligned} E_{\rm ext}^{\rm mod} &= 4b_{\rm e}A_0^2 M R_{\rm c}^2, \\ \left(\sigma_{\rm eff,los}^{\rm mod}\right)^2 &= \sigma_{\rm sg,los}^2 + \frac{4b_{\rm e}A_0^2R_{\rm c}^2}{3} \\ &\approx \sigma_{\rm gs,los}^2 + \frac{4b_{\rm e}A_0^2R_{\rm c}^2}{3} \quad \text{and} \\ \alpha_{\rm eff,vir}^{\rm mod} &= \frac{\sigma_{\rm sg,los}^2 R_{\rm c}}{b_{\rm s}GM} + \frac{4b_{\rm e}A_0^2R_{\rm c}^3}{3b_{\rm s}GM} \\ &\approx \frac{\sigma_{\rm gs,los}^2 R_{\rm c}}{b_{\rm s}GM} + \frac{4b_{\rm e}A_0^2R_{\rm c}^3}{3b_{\rm s}GM}, \end{aligned} \tag{48}$$

where we have again assumed vertical equilibrium, isotropy in the equatorial plane and $\sigma_{\rm sg,los} \approx \sigma_{\rm gs,los}$. The detailed derivations of these equations and their more general forms for a homogeneous ellipsoidal cloud are provided in Appendix B.

Unsurprisingly, in the shear model the overall effect of external gravity primarily depends on the shear arising from the differential rotation of the galaxy disc (i.e. Oort's constant A). We note that $E_{\rm ext}^{\rm mod}$ can be understood as the rotational kinetic energy of a cloud with angular velocity $\omega_{\rm shear} = -2A_0$, as generally the rotational kinetic energy $E_{\rm rot} = \frac{1}{2}I\omega^2$ and $I = 2b_{\rm e}MR_{\rm c}^2$ for a spherical cloud. Our derived $\omega_{\rm shear}$ is the same as that derived by Goldreich & Lynden-Bell (1965) and Fleck & Clark (1981), and it arises naturally when considering fluid element motions near the tidal radius (see Section 6.3). For a galaxy with a solid-body circular velocity curve, the external gravity has no effect on the cloud, i.e. $A = 0$ and thus $E_{\rm ext}^{\rm mod} = 0$. The distributions of $\alpha_{\rm vir,eff}^{\rm mod}$ and $\beta^{\rm mod} \equiv \frac{E_{\rm ext}^{\rm mod}}{|U_{\rm sg}|}$ for axisymmetric and ellipsoidal clouds are shown in the third and fourth panels of Fig 14, respectively, for the 141 spatially resolved clouds of NGC 4429. For clouds assumed to be axisymmetric, a lognormal fit to the distribution of $\alpha_{\rm vir,eff}^{\rm mod}$ yields a mean $\langle\alpha_{\rm eff,vir}^{\rm mod}\rangle = 2.02 \pm 0.03$ and a standard deviation of 0.10 dex, while a Gaussian fit to the distribution of $\beta^{\rm mod}$ yields a mean $\langle\beta^{\rm mod}\rangle = 0.79 \pm 0.37$ and a standard deviation of 0.36. For clouds assumed to be ellipsoidal, analogous fits yield $\langle\alpha_{\rm eff,vir}^{\rm mod}\rangle_{\rm ellipsoid} = 2.35 \pm 0.07$ and a standard deviation of 0.17 dex, and $\langle\beta^{\rm mod}\rangle_{\rm ellipsoid} = 0.90 \pm 0.28$ and a standard deviation of 0.46. Both sets of predictions therefore compare very well with our measurements ($\langle\alpha_{\rm eff,vir}\rangle = 2.15 \pm 0.12$ and $\langle\beta\rangle = 0.71 \pm 0.33$ for axisymmetric clouds and $\langle\alpha_{\rm eff,vir}\rangle_{\rm ellipsoid} = 2.59 \pm 0.19$ and $\langle\beta\rangle_{\rm ellipsoid} = 0.91 \pm 0.35$ for ellipsoidal clouds; see Sections 5.6 and 5.7, respectively), although with less scatter as expected (our model predictions do not take into account measurement errors). This thus supports yet again our conclusion that the bulk motions of the clouds in NGC 4429 are primally driven by shear motions. Indeed, our shear model provides good estimates of $E_{\rm ext}$, $\alpha_{\rm eff,vir}$, and β for the spatially resolved clouds of NGC 4429.

It is nevertheless worth noting that, while our shear model accounts for the observed bulk motions of the clouds well, there are also some discrepancies. Our shear model overestimate the angular velocities of the spatially resolved clouds of NGC 4429 by a median factor of ≈1.5–2.0, and the modelled and observed position angles have a median angle difference of ≈16°−19° (see Section 4.2). Moreover, there is considerable scatter about the 1:1 correlation between the observed velocity dispersions $\sigma_{\rm obs,los}$ and the modelled velocity dispersions $\sigma_{\rm mod,los}$ (Fig. 16). It therefore appears that, although the effects of external gravity are dominant, other factors also noticeably affect the dynamics of clouds, so that the clouds's fluid elements do not follow pure shear motions. We discuss one such factor, self-gravity, below.

6.2 Equilibrium between self-gravity and external-gravity

In previous sections, we established that the contributions of external gravity to the gravitational energy budgets of the NGC 4429 clouds (i.e. $E_{\rm ext}$) are clearly non-zero, this whether these contributions are calculated from observations (Section 5.5) or our shear model (Section 6.1). However, $E_{\rm ext}$ on its own does not determine whether a cloud is gravitationally bound or not. As a robust threshold between gravitationally bound and unbound objects, we have adopted a critical virial parameter $\alpha_{\rm vir,crit} = 2$ (Kauffmann et al. 2013, 2017). When the effective virial parameter $\alpha_{\rm eff,vir}$ is equal to this critical value, $2|U_{\rm sg}| = 2E_{\rm turb} + E_{\rm ext}$ ($U_{\rm sg} \equiv -\frac{3b_{\rm s}GM^2}{R_{\rm c}}$), where

$$E_{\rm turb} \equiv \frac{3}{2}M\sigma_{\rm sg,los}^2 \tag{49}$$

is the kinetic energy of the turbulent motions associated with self-gravity (see equations 34, 32, and 31). If a cloud is thus marginally gravitationally bound (i.e. $\alpha_{\rm eff,vir} = \alpha_{\rm vir,crit} = 2$) and an internal virial equilibrium is established by self-gravity (i.e. $\alpha_{\rm sg,vir} \approx 1$), as is the

case for the NGC 4429 clouds, we further obtain

$$\begin{cases} 2E_{\rm turb} + U_{\rm sg} = 0, \\ E_{\rm ext} + U_{\rm sg} = 0. \end{cases} \quad (50)$$

The top equation indicates an equilibrium between a cloud's self-gravitational energy and its turbulent kinetic energy, while the bottom equation indicates an equilibrium between a cloud's self-gravitational energy and its energy contributed by external gravity.

In general, one needs to compare $E_{\rm ext}$ with the self-gravitational energy of a cloud to assess its boundedness. If $E_{\rm ext} \gg |U_{\rm sg}|$ (i.e. $\beta \gg 1$), then external gravity is much more important and the cloud is not gravitationally bound (unless other forces are present). If $E_{\rm ext} \ll |U_{\rm sg}|$ (i.e. $\beta \ll 1$), then self-gravity is much more important and the effects of external gravity are negligible. If $E_{\rm ext} \approx |U_{\rm sg}|$ (i.e. $\beta \approx 1$), then external gravity and self-gravity are equally important and the cloud reaches a state of equilibrium between self-gravity and external gravity. Here, we have found that the NGC 4429 clouds have $E_{\rm ext}$ comparable to (the absolute values of) their self-gravitational energies, with both $\langle\beta\rangle \approx 1$ (see Section 5.5) and $\beta^{\rm mod} \approx 1$ (see Section 6.1). The energy of each cloud contributed by external gravity $E_{\rm ext}$ thus roughly equals its self-gravitational energy and the cloud remains marginally gravitationally bound.

6.2.1 *Tidal radius*

In the case where the gravitational motions of the clouds are completely dominated by shear motions, as is the case for the NGC 4429 clouds (see Section 6.1), the bottom equation of equations (50) then indicates an equilibrium between a cloud's self-gravitational energy and its kinetic energy associated with those shear motions. Another way to assess whether self-gravity or external gravity is more important is thus to consider the tidal radius of each cloud, which defines the volume over which self-gravity dominates over external gravity. Here, we adopt the tidal radius $R_{\rm t}$ defined by Gammie et al. (1991) and Tan (2000), which is the radial distance from the cloud's centre at which the shear velocity due to differential galactic rotation (i.e. our previously defined $v_{\rm shear}$; see equation 46) is equal to the escape velocity from the cloud:

$$R_{\rm t} \equiv (1 - \beta_{\rm circ,0})^{-2/3} \left(\frac{2M}{M_{\rm gal,0}}\right)^{1/3} R_0, \quad (51)$$

where as before M is the cloud's mass and R_0 the galactocentric distance of the cloud's CoM in the plane of the disc, $M_{\rm gal,0}$ is the total galactic mass interior to R_0, $\beta_{\rm circ,0} \equiv \frac{{\rm d}\ln V_{\rm circ}(R)}{{\rm d}\ln R}|_{R=R_0}$, and as before $V_{\rm circ}(R)$ is the galaxy circular velocity curve. Equation (51) assumes a spherical galaxy mass distribution, i.e. $M_{\rm gal}(R) = V_{\rm circ}(R)^2 R/G$, and can therefore be simplified to

$$R_{\rm t} = \left(\frac{G}{2A_0^2}\right)^{1/3} M^{1/3}. \quad (52)$$

The tidal radius defined in this manner is the maximum size of a cloud (of a given mass M) allowed by galactic rotational shear.

Interestingly, for a cloud with $R_{\rm c} = R_{\rm t}$, we have

$$\begin{aligned} \beta^{\rm mod}(R_{\rm c} = R_{\rm t}) &\equiv \frac{E_{\rm ext}^{\rm mod}(R_{\rm c} = R_{\rm t})}{|U_{\rm sg}(R_{\rm c} = R_{\rm t})|} \\ &= \frac{4b_{\rm e}A_0^2 M R_{\rm t}^2}{3b_{\rm s}GM^2/R_{\rm t}} \\ &= \frac{2}{3}\frac{b_{\rm e}}{b_{\rm s}} \\ &\approx 1 \end{aligned} \quad (53)$$

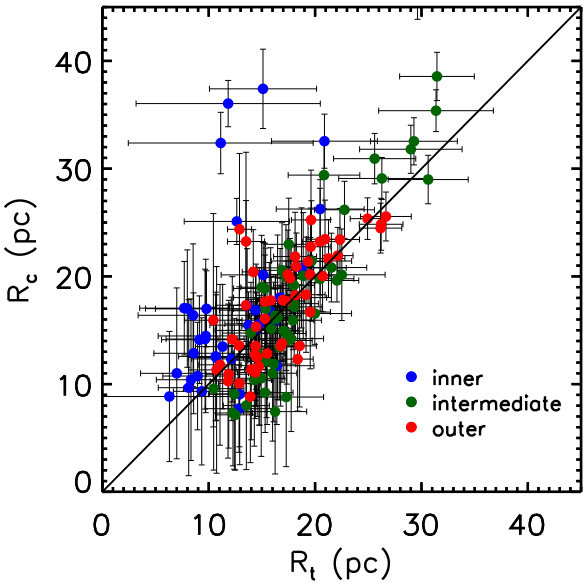

Figure 17. Comparison of the observed cloud size and expected tidal radius of the 141 spatially resolved clouds of NGC 4429. Data points are colour-coded by region. The black solid diagonal line shows the 1:1 relation.

(see equations 48 and 32), which is essentially identical to the measured β of the spatially resolved clouds of NGC 4429 (assuming axisymmetric clouds; see Sections 5.6 and 5.7). In our shear model, the tidal radius given by equation (52) thus approximately corresponds to the radial distance at which $\beta^{\rm mod} \approx 1$. It is thus clear the reason a cloud with $\beta^{\rm mod} \gg 1$ becomes gravitationally unbound is because the shear motions are so strong that the (outer) fluid elements manage to escape from the self-gravitational influence of the cloud. Fig. 17 compares the observed sizes (radii $R_{\rm c}$) of the spatially resolved clouds of NGC 4429 with their tidal radii expected from equation (52). There is generally a very good agreement, albeit with a few exceptions. The NGC 4429 clouds therefore seem to reach their maximum sizes allowed by galactic shear, further supporting our conclusion that the NGC 4429 clouds have reached a rough equilibrium between self-gravity and external gravity and thereby manage to remain marginally gravitationally bound. A few clouds in the inner region have sizes much larger than their tidal radii, suggesting that these inner clouds cannot be gravitationally bound due to shear, and indeed all these clouds have high β ($\beta \approx 4$–6) and $\alpha_{\rm eff,vir}$ ($\alpha_{\rm eff,vir} \approx 5$–$7$).

6.2.2 *Size and surface density*

For a cloud to be marginally gravitationally bound, the contribution of external gravity to the cloud's energy budget must not exceed the cloud's self-gravitational energy, i.e. $\beta^{\rm mod} = E_{\rm ext}^{\rm mod}/|U_{\rm sg}| = 4b_{\rm e}A_0^2 M R_{\rm c}^2/| - 3b_{\rm s}GM^2/R_{\rm c}| = 4b_{\rm e}A_0^2 R_{\rm c}/3\pi b_{\rm s} G\Sigma_{\rm gas} \leq 1$ (see equations 48 and 32). This implies that, at a given surface density, there is a maximum size ($R_{\rm shear}$) for a cloud to stay marginally bound against tidal/shear disruptions:

$$R_{\rm c} \leq R_{\rm shear} \approx \frac{3\pi b_{\rm s} G\Sigma_{\rm gas}}{4b_{\rm e}A_0^2}. \quad (54)$$

Equivalently, at a given size, there is a minimum surface density ($\Sigma_{\rm shear}$) for a cloud to remain marginally bound:

$$\Sigma_{\rm gas} \geq \Sigma_{\rm shear} \approx \frac{4b_{\rm e}A_0^2 R_{\rm c}}{3\pi b_{\rm s} G}. \quad (55)$$

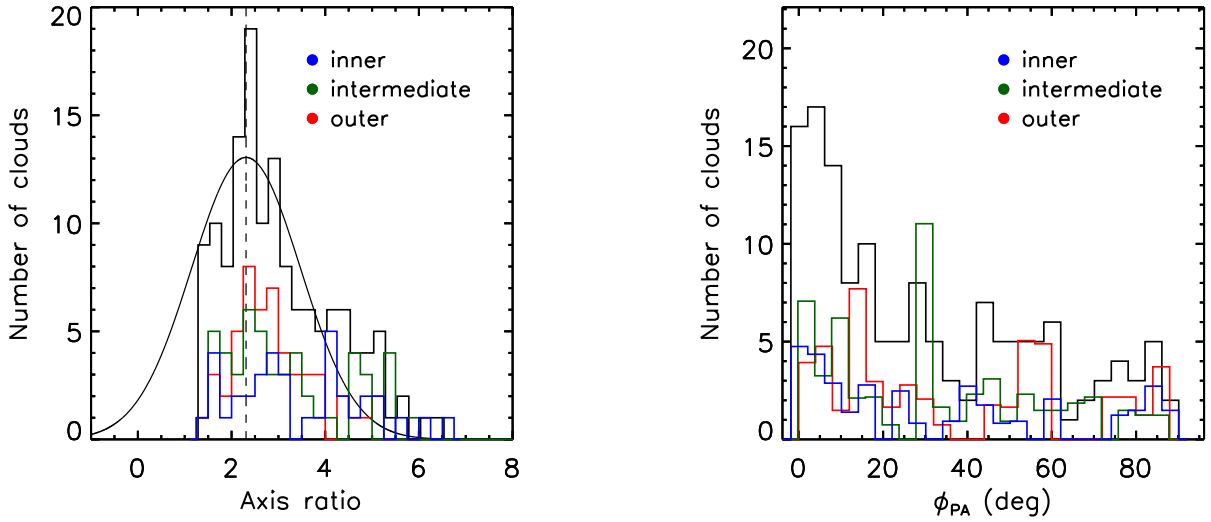

Figure 18. Distribution of deprojected axis ratios (*left*) and position angles ϕ_{PA} between the (morphological) major axes and the direction to the galaxy centre (*right*) for the 141 spatially resolved clouds of NGC 4429 (the black histograms), and for only the clouds in the inner (the blue histograms), intermediate (the green histograms), and outer (the red histograms) region of the galaxy, respectively. $\phi_{PA} = 0^\circ$ is the radial (i.e. galactocentric) direction, while $\phi_{PA} = 90^\circ$ is the azimuthal direction. The black vertical dashed line in the left-hand panel indicates the mean axial ratio derived from a Gaussian fit (the black solid line).

The spatially resolved clouds of NGC 4429 have a mean surface density $\langle \Sigma_{gas} \rangle \approx 160\ M_\odot\,pc^{-2}$ and a mean Oort's constant A_0 (i.e. shear) $\langle A_0 \rangle \approx 0.3\,km\,s^{-1}\,pc^{-1}$. A simple calculation using equation (54; and assuming $b_s = b_e = \frac{1}{5}$ for spherical homogeneous clouds as usual) then suggests that, if limited by shear, the mean size $\langle R_{shear} \rangle$ of the clouds in NGC 4429 should be ≈18 pc, that matches extremely well the observed mean size $\langle R_c \rangle \approx 17$ pc. We thus find again that typical clouds in NGC 4429 reach their maximal sizes (or minimum surface densities) allowed by shear, and are thus not limited by other processes (shear rules!).

Finally, as we have pointed out above, the effects of self-gravity are generally of the same order as those of external (i.e. galactic) gravity: $\beta \approx 1$ (see Section 5.6) and $R_c \approx R_t$. The motions of the fluid elements within these marginally gravitationally bound clouds will therefore not completely follow those prescribed by external gravity alone (i.e. the shear motions governed by equations 45). This is again expected, as if the bulk motions of cloud fluid elements were to exactly follow pure shear motions, the clouds could not be (marginally) gravitationally bound.

Therefore, the equations of (bulk) motions must include additional terms due to self-gravity (cf. equations 43):

$$\begin{cases} a'_{ext,x'} \approx T_0 x' + 2\Omega_0 v'_{gal,y'} - \dfrac{\partial \Phi_{sg}}{\partial x'}, \\ a'_{ext,y'} \approx -2\Omega_0 v'_{gal,x'} - \dfrac{\partial \Phi_{sg}}{\partial y'}, \end{cases} \tag{56}$$

where Φ_{sg} is the cloud's own (self) gravitational potential. Solving these coupled differential equations is very difficult and beyond the scope of this paper, although we do derive approximate analytic solutions in Section 6.3 for a particular case. We refer readers to Julian & Toomre (1966), Gammie et al. (1991), and Binney (2020) for some numerical solutions.

Gammie et al. (1991) suggested that equations (45) can provide good-zeroth-order solutions to equations (56) at large radii (where $R_c \geq R_t$). Therefore, the bulk motions of gravitationally unbound ($R_c \gg R_t$) clouds should roughly approximate the gravitational shear motions described by equations (45). However, unlike gravitationally unbound clouds, where the discrepancies between bulk motions and shear motions are expected to be negligible, marginally gravitationally bound clouds should have bulk motions that deviate considerably from shear motions. This is because the discrepancies between bulk motions and shear motions should increase with the importance of self-gravity. Indeed, while the bulk motions of the NGC 4429 clouds do approximately follow gravitational shear motions, noticeable deviations are also found (see Section 6.1). We provide approximate solutions for this case below.

6.3 Cloud morphology

Cloud morphology may reflect the origin of the gas motions (e.g. Meidt et al. 2018) and the physical mechanisms injecting energy into the gas on cloud scales (e.g. Koda et al. 2006). To quantify the morphology of the 141 spatially resolved clouds of NGC 4429, we considered their major and minor axes (and thus their axis ratios and position angles with respect to the radial/galactocentric direction) as measured in the plane of the sky (i.e. deprojected) in Section 5.7.

The distribution of the deprojected clouds' axis ratios is shown in the left-hand panel of Fig. 18. A Gaussian fit to the distribution yields a mean of 2.3 ± 0.2, suggesting that the clouds of NGC 4429 are significantly elongated. Moreover, the clouds in the inner and intermediate regions are more elongated (mean axial ratio of 2.9 and 2.6, respectively) than the clouds in the outer region (mean axial ratio of 2.2).

The distribution of deprojected position angles ϕ_{PA} is shown in the right-hand panel of Fig. 18. The distribution peaks at 5°, with a mean $\langle \phi_{PA} \rangle \approx 32^\circ$, confirming the impression from Fig. 3 that the clouds of NGC 4429 are preferentially elongated in the radial (i.e. galactocentric) direction. In fact, the clouds at small radii tend to have smaller ϕ_{PA}, i.e. they are even more preferentially elongated in the direction of the galaxy centre. The mean angle ϕ_{PA} of the clouds in the inner, intermediate, and outer region is 28°, 32°, and 34°, respectively.

It is worth noting that the tendency for the clouds to align with the radial direction could at least partially be due to an artefact of `CPROPS`. As `CPROPS` tends to assign the pixels with the shortest 'distances' (through the 3D data cube) to the same cloud, the clouds

identified by CPROPS could be preferentially elongated along the isovelocity contours, that are often nearly radial in NGC 4429 (see Fig. 7). Having said that, we note that the clouds identified by CPROPS in other galaxies do not seem to exhibit such a tendency (e.g. M33, Gratier et al. 2012; NGC 4526, Utomo et al. 2015; NGC 6946, Wu et al. 2017). This thus suggests that the observed trend of the clouds of NGC 4429 to be radially elongated could be real.

If the observed tendency is real, what are the physical mechanisms that could cause such a strong radial elongation of the clouds of NGC 4429? It is interesting to note that, according to equation (53),

$$\beta^{\rm mod}(R_{\rm c}) = \beta^{\rm mod}(R_{\rm t}) \left(\frac{R_{\rm c}}{R_{\rm t}}\right)^3 \approx \left(\frac{R_{\rm c}}{R_{\rm t}}\right)^3, \tag{57}$$

which suggests that if $R_{\rm c} < R_{\rm t}$ then $\beta^{\rm mod} < 1$ (and vice versa) and if $R_{\rm c} > R_{\rm t}$ then $\beta^{\rm mod} > 1$ (and vice versa). If a cloud is primarily dominated by self-gravity (i.e. $R_{\rm c} \ll R_{\rm t}$ or $\beta^{\rm mod} \ll 1$), the effects of external gravity are negligible and the cloud should be roughly round. On the other hand, if a cloud is largely dominated by external gravity (i.e. $R_{\rm c} \gg R_{\rm t}$ or $\beta^{\rm mod} \gg 1$), the cloud should be elongated in the azimuthal direction due to strong shear motions (Meidt et al. 2018). However, the NGC 4429 clouds are neither round nor azimuthally elongated, suggesting their morphologies cannot be regulated by either self-gravity and/or external gravity alone.

It is thus interesting to investigate the geometry of a marginally gravitationally bound cloud, as is the case for the bulk of the NGC 4429 clouds, where both self-gravity and external gravity are important (i.e. $R_{\rm c} \approx R_{\rm t}$ and $\beta \approx \beta^{\rm mod} \approx 1$; see Sections 5.6 and 6.2). For this, we must solve the equations of motions given by equations (56), which include both self-gravity and external gravity terms. If we can calculate the motions of the fluid elements near the external edge of each cloud, these motions will define the approximate overall shapes of marginally gravitationally bound clouds.

Exact analytic solutions to equations (56) may not be possible, so we instead turn to a mathematical technique analogous to perturbation theory to find approximate solutions. We define a new dimensionless variable $\epsilon \equiv 1$ and rewrite equations (56) as

$$\begin{cases} a'_{{\rm ext},x'} \approx T_0 x' + 2\Omega_0 v'_{{\rm gal},y'} - \dfrac{\partial \Phi_{\rm sg}}{\partial x'}, \\ a'_{{\rm ext},y'} \approx -2\Omega_0 \epsilon v'_{{\rm gal},x'} - \dfrac{\partial \Phi_{\rm sg}}{\partial y'}. \end{cases} \tag{58}$$

Approximate solutions to the above equations can be written as

$$\begin{cases} x'(t) \approx x'^{(0)}(t) + \epsilon x'^{(1)}(t), \\ y'(t) \approx y'^{(0)}(t) + \epsilon y'^{(1)}(t), \end{cases} \tag{59}$$

where analogously to perturbation theory we will refer to $x'^{(0)}$ and $y'^{(0)}$ as the zeroth-order solutions and to $x'^{(1)}$ and $y'^{(1)}$ as the first-order solutions, although the latter are not necessarily smaller than the former. Substituting equations (59) into equations (58), we can separate the zeroth- and first-order equations in ϵ:

$$\begin{cases} \ddot{x}'^{(0)} = T_0 x'^{(0)} + 2\Omega_0 \dot{y}'^{(0)} - \dfrac{\partial \Phi_{\rm sg}}{\partial x'}, \\ \ddot{y}'^{(0)} = -\dfrac{\partial \Phi_{\rm sg}}{\partial y'}, \end{cases} \tag{60}$$

and

$$\begin{cases} \ddot{x}'^{(1)} = T_0 x'^{(1)} + 2\Omega_0 \dot{y}'^{(1)}, \\ \ddot{y}'^{(1)} = -2\Omega_0 \dot{x}'^{(0)}. \end{cases} \tag{61}$$

We note that the solutions to equations (60) and (61) provide solutions to equations (58) for only a particular case, and they are only approximate solutions as the second-order term in ϵ is assumed to be negligible, i.e. $-2\Omega_0 \epsilon^2 \dot{x}'^{(1)} \approx 0$ (assumptions we will justify below).

We first solve the zeroth-order equations. While finding a general analytic solution to the equations (60) is beyond the scope of this paper, there must exist a particular cloudcentric radius $R_{\rm circ}$ where to zeroth order the fluid element has uniform circular motion of a particular angular frequency $\omega_{\rm circ}$ (and arbitrary phase ψ). We thus postulate

$$\begin{cases} x'^{(0)}(t) = R_{\rm circ} \cos(\omega_{\rm circ} t + \psi), \\ y'^{(0)}(t) = R_{\rm circ} \sin(\omega_{\rm circ} t + \psi). \end{cases} \tag{62}$$

Substituting equation (62) into the first equation of equation (60), we find that the first and second terms on the right-hand side (i.e. the tidal and Coriolis force terms) cancel out only for an angular frequency $\omega_{\rm circ} = -2A_0$ (as $T = 4A\Omega$). While shear does not lead to circular motions, that is of course simply equal to $v_{\rm shear}/x'^{(0)}$ (see equation 46), i.e.

$$\omega_{\rm circ} = -2A_0 = v_{\rm shear}/x'^{(0)} = \omega_{\rm shear} \tag{63}$$

(the same $\omega_{\rm shear}$ defined in Section 6.1). The term on the left-hand side and the third term on the right-hand side then lead to a condition on $R_{\rm circ}$. Assuming the entire cloud mass is contained within $R_{\rm circ}$, one obtains

$$\begin{aligned} R_{\rm circ} &= \left(\frac{GM}{4A_0^2}\right)^{1/3} \\ &= 2^{-\frac{1}{3}} R_{\rm t} \end{aligned} \tag{64}$$

(see equation 52). The same condition is obtained by substituting equations (62) into the second equation of equations (60). It is trivial to show that at this radius, $v_{\rm shear} = -v_{\rm circ}$, where $v_{\rm circ}$ is the circular velocity due to the cloud alone [i.e. $v_{\rm shear}(R_{\rm circ}) = -2A_0 R_{\rm circ} = -(GM/R_{\rm circ})^{1/2} = -v_{\rm circ}(R_{\rm circ})$ for $R_{\rm circ}$ given by equation 64].

In other words, the (zeroth-order in ϵ) solution to equations (60) is

$$\begin{cases} x'^{(0)}(t) = R_{\rm circ} \cos(-2A_0 t + \psi), \\ y'^{(0)}(t) = R_{\rm circ} \sin(-2A_0 t + \psi), \end{cases} \tag{65}$$

where $R_{\rm circ}$ is given by equation (64). This orbit is thus intuitive to understand. In the cloud rotating frame, to zeroth order, the fluid element will have uniform circular motion at the radius $R_{\rm circ}$ where the shear velocity due to the external (i.e. galactic) potential $v_{\rm shear}$ is equal to the cloud's own circular velocity $v_{\rm circ}$, and thus the shear angular velocity $\omega_{\rm shear}$ is equal to the cloud's angular velocity $\omega_{\rm circ}$ [i.e. $v_{\rm shear}(R_{\rm circ})/R_{\rm circ} = v_{\rm circ}(R_{\rm circ})/R_{\rm circ}$].

Equally important, the radius of this circular orbit is very close to the tidal radius and thus the external edge of the cloud ($R_{\rm circ} \approx 0.8\, R_{\rm t}$ according to equation 64). Our solutions can thus indeed help us understand the outer shapes of marginally bound clouds.

We note that our zeroth-order solutions in ϵ above are different from those found in Goldreich & Tremaine (1982) and Gammie et al. (1991; equations 45 in this paper). This is because we introduced ϵ in the azimuthal Coriolis force term while they applied ϵ to the self-gravity terms, and because we are considering a particular case where the fluid element's shear velocity is equal to its circular velocity. Equation (65) thus suggests that the fluid element should have a circular orbit about the cloud's CoM (i.e. the cloud should be round near its tidal radius) if the Coriolis force in the azimuthal direction is neglected (the $-2\Omega_0 v'_{{\rm gal},x'}$ term in the second equation

of equations 56). This is not surprising, since as we have shown the Coriolis force ($2\Omega_0 v'_{\mathrm{gal},y'}$) cancels out the tidal force ($T_0 x'$) in the radial direction, hence only the cloud's self-gravity needs to be considered.

Having solved the zeroth-order equations of motion (equations 60), we can now solve the first-order equations in ϵ (equations 61). Substituting the first equation of equations (65) into the second equation of equations (61) and imposing that the fluid element follows the zeroth-order solution at $t = 0$ (i.e. $\dot{y}'^{(1)}(t = 0) = y'^{(1)}(t = 0) = 0$) yields a solution for $y'^{(1)}(t)$. Substituting this in turn into the first equation of equations (61) and imposing again that the fluid element follows the zeroth-order solution at $t = 0$ (i.e. $\dot{x}'^{(1)}(t = 0) = x'^{(1)}(t = 0) = 0$) yields a solution for $x'^{(1)}(t)$. These first-order solutions are

$$
\begin{aligned}
x'^{(1)}(t) \approx \frac{\Omega_0}{A_0} R_{\mathrm{circ}} \Bigg[\frac{A_0}{A_0 + \Omega_0} \Bigg(& \cos(\psi)\cosh(\sqrt{T_0}\,t) \\
& - \sqrt{\frac{\Omega_0}{A_0}}\sin(\psi)\sinh(\sqrt{T_0}\,t)\Bigg) \\
& + \frac{\Omega_0}{A_0 + \Omega_0}\cos(-2A_0 t + \psi) - \cos(\psi)\Bigg], \\
y'^{(1)}(t) \approx \frac{\Omega_0}{A_0} R_{\mathrm{circ}} & [\sin(-2A_0 t + \psi) + 2A_0\cos(\psi)\,t - \sin(\psi)].
\end{aligned}
\tag{66}
$$

We therefore have complete zeroth- and first-order solutions in ϵ of the equations of motion equations (58), for fluid elements originally in uniform circular rotation around the cloud's CoM at a cloudcentric radius of R_{circ}.

In practice, with our treatment in term of ϵ, we have neglected the first-order Coriolis force term in the azimuthal direction (i.e. the $-2\Omega_0 v'^{(1)}_{\mathrm{gal},x'}$ term in the second equation of equations 56). Our solutions will thus only be valid as long as this term remains small compared to $\ddot{y}'$. A comparison of these two terms shows that this remains the case for times up to several $t_{\mathrm{shear}} \equiv 1/2A_0$ for nearly all phases ψ, when the fluid element remains relatively close to the circle of radius R_{circ}.

By sampling the phases ψ uniformly, Fig. 19 therefore shows how a circular ring of matter initially at a cloudcentric radius R_{circ} evolves over time (colour-coded), up to a time $t = 2\,t_{\mathrm{shear}}$. As expected from our solutions, particularly the diverging term in $x'^{(1)}(t)$ (see equations 66), the fluid element orbits and thus the ring become increasingly elongated over time, this almost always in the radial direction (i.e. along $\hat{x}'$), more so but not exclusively at late times.

Therefore, contrary to naive expectations, clouds with sizes $\approx R_{\mathrm{t}}$ and thus $\approx R_{\mathrm{circ}}$, which are necessarily marginally bound, should have shapes that are *radially* elongated. This state thus presumably represents an intermediate state between (i) small strongly bound clouds that are expected to be spherical (due to self-gravity) and (ii) large unbound gas accumulations that are expected to be azimuthally elongated (due to shear). In other words, the general radial elongation of the NGC 4429 clouds is fully consistent with the fact that the clouds extend to typically their tidal radii and are typically marginally gravitationally bound, with roughly equal impact from self- and external gravity (i.e. $\beta \approx 1$).

Interestingly, the numerical solutions of Julian & Toomre (1966) and Binney (2020) suggest a similar result. By solving equations (56) numerically, they derived density patterns for a shear flow under both self- and external gravity forces. While the outer contours at lower surface densities (where self-gravity is much less important than external gravity) are elongated azimuthally as expected, their results demonstrate that the innermost contours at higher densities (where self-gravity may be as important as external gravity) are *radially* elongated (see figs 7–9 in Julian & Toomre 1966 and fig. 9 in Binney 2020). These works thus reinforce our approximate analytical solutions above.

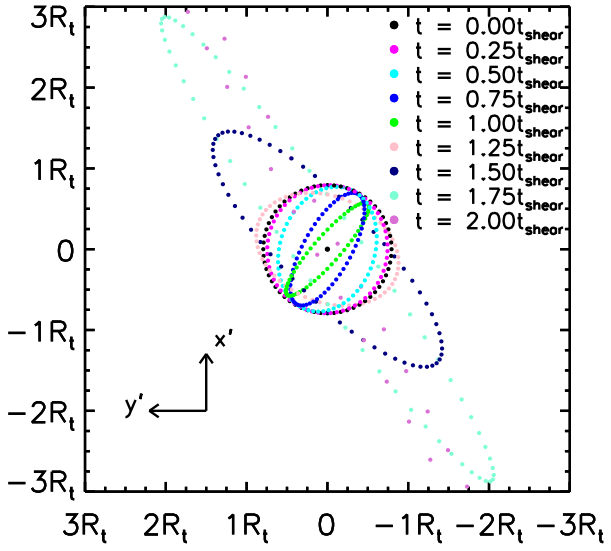

Figure 19. Orbits resulting from the zeroth- and first-order solutions to the equations of motion equations (58), for fluid elements originally in uniform circular rotation around the cloud's CoM at a cloudcentric radius of R_{circ}, in the rotating frame adopted in Appendix A2 (see Fig. A1). Several orbits are shown, sampling all phases uniformly and colour-coded as a function of time. The initially circular ring becomes increasingly elongated over time and is nearly always elongated radially. The small black solid circle marks the galaxy centre, while the large black-dashed circle shows the original configuration of the fluid elements (zeroth-order solution).

6.4 Cloud scale height

Our current analysis is based on the common assumption that the clouds of NGC 4429 are in vertical hydrostatic equilibria, i.e. $M(\sigma^2_{\mathrm{gal},z} - b_{\mathrm{e}}\nu_0^2 Z_{\mathrm{c}}^2) \approx 0$ (see equation 27). If this assumption is valid, we can derive the scale height of each cloud (Z_{c}) from estimates of ν_0 and $\sigma_{\mathrm{gal},z}$. As before, ν_0 is obtained directly from our stellar mass model (i.e. $\nu_0^2 = 4\pi G\rho_{*,0}$, where $\rho_{*,0}$ is provided by our our MGE model; see Appendix C). According to equation (20), $\sigma^2_{\mathrm{gal},z}\cos^2 i \approx \sigma^2_{\mathrm{gs,los}} - \sigma^2_{\mathrm{sg,los}}$, so if $\sigma_{\mathrm{sg,los}}$ can indeed be derived from equation (24) (i.e. $\sigma^2_{\mathrm{sg,los}} = \pi b_{\mathrm{s}} G R_{\mathrm{c}}\Sigma_{\mathrm{gas}}$), we can obtain $\sigma^2_{\mathrm{gal},z}$.

We note that the uncertainties of our measured physical quantities (i.e. $\sigma^2_{\mathrm{gs,los}}$, R_{c}, and Σ_{gas}) can be significant and prevent us from accurately estimating $\sigma_{\mathrm{gal},z}$ for individual clouds, as we find negative $\sigma^2_{\mathrm{gal},z}$ in a few cases. Instead, we therefore consider only the average quantities for $\sigma^2_{\mathrm{gal},z}$ and Z_{c}. We derive a mean $\langle\sigma^2_{\mathrm{gal},z}\rangle = 18 \pm 2$ km^2 s^{-2} for the 141 spatially resolved clouds of NGC 4429 (assuming $b_{\mathrm{s}} = \frac{1}{5}$ for spherical homogeneous clouds), whose mean line-of-sight projection ($\langle\sigma^2_{\mathrm{gal},z}\cos^2 i\rangle \approx 2$ km^2 s^{-2}) is indeed relatively small compared to $\langle\sigma^2_{\mathrm{gs,los}}\rangle \approx 11$ km^2 s^{-2} and $\langle\sigma^2_{\mathrm{sg,los}}\rangle \approx 8$ km^2 s^{-2}.

Utilizing our derived $\langle\sigma^2_{\mathrm{gal},z}\rangle = 18 \pm 2$ km^2 s^{-2} and $\langle\rho_{*,0}\rangle \approx 33$ M$_\odot$ pc^{-3} (and further assuming $b_{\mathrm{e}} = \frac{1}{5}$ for spherical homogeneous clouds), we derive a mean cloud scale height $\langle Z_{\mathrm{c}}\rangle \approx 7$ pc, which is clearly smaller than the average cloud radius $\langle R_{\mathrm{c}}\rangle \approx 16$ pc (see Section 3.3). Consequently, the clouds of NGC 4429 are not strictly

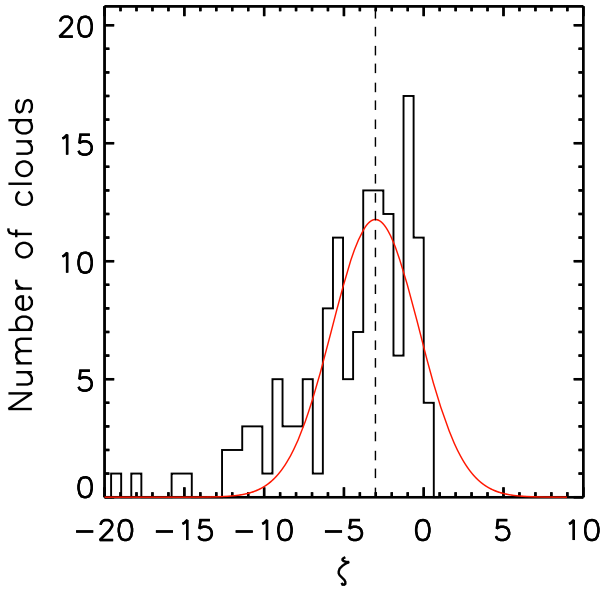

Figure 20. Distribution of ζ, defined as the the ratio between the vertical contribution of the external potential to a cloud's energy budget and the (absolute value of the) cloud's self-gravitational energy, assuming the cloud is roundish (i.e. $Z_c = R_c$), for the 141 spatially resolved clouds of NGC 4429. The black-dashed vertical line shows the mean of a Gaussian fit (red solid line) to the distribution.

spherical, but more likely to be elongated (i.e. flattened) in the plane, if the clouds are indeed in vertical hydrostatic equilibria.

The above analysis aimed to derive the scale heights of the clouds Z_c by assuming that the clouds are in vertical hydrostatic equilibria. However, we can also investigate the vertical equilibrium state of the clouds by assuming $Z_c = R_c$ instead. For such a roundish cloud, the contribution of the vertical component of the external potential to the cloud's gravitational energy budget is $\approx M(\sigma^2_{\rm gal,z} - b_e v_0^2 R_c^2)$. We thus define ζ as the ratio between $M(\sigma^2_{\rm gal,z} - b_e v_0^2 R_c^2)$ and the (absolute value of the) self-gravitational energy of a roundish cloud ($U_{\rm sg} = -3b_s GM^2/R_c$):

$$\zeta \equiv \frac{M\left(\sigma^2_{\rm gal,z} - b_e v_0^2 R_c^2\right)}{3b_s GM^2/R_c}. \tag{67}$$

The distribution of ζ for the 141 spatially resolved clouds of NGC 4429 is presented in Fig. 20, where we have assumed $b_s = b_e = \frac{1}{5}$ (spherical homogeneous clouds) as usual. We find that ζ is not negligible, but significantly below zero. A Gaussian fit to the ζ distribution yields a mean $\langle\zeta\rangle = -1.97 \pm 0.55$. This implies that the effect of external gravity on roundish clouds is to compress them in the vertical direction. In other words, if the clouds of NGC 4429 were roundish, the shear in the plane of the galaxy would be overwhelmed by compression in the vertical direction, and the net effect of external gravity would be to contribute to the (vertical) collapse of the clouds (as $|\langle\beta\rangle| < |\langle\zeta\rangle|$). This probably explains why the clouds of NGC 4429 appear to be flattened in the plane.

Indeed, a cloud in a thin disc is more likely to exhibit an elongated structure in the plane rather than be spherical, as the force applied by the background galactic potential in the vertical direction far exceeds the forcing experienced in the plane (e.g. Meidt et al. 2018). In fact, such elongations of molecular clouds in the equatorial plane have been observed in a sample of more than 500 MW clouds (Koda et al. 2006).

7 CONCLUSIONS

Using our modified version of the CPROPSTOO code, more robust and efficient to identify GMCs in complex and crowded environments, and ^{12}CO(J = 3–2) ALMA observations at $14 \times 11\,{\rm pc}^2$ resolution, we identified 217 GMCs (141 spatially resolved) in the central molecular gas disc of the lenticular galaxy NGC 4429. To investigate the dynamical states of the GMCs, we developed and utilized an MVT that fully accounts for the impacts of the background galactic potential. The main results are as follows:

(i) The GMCs of NGC 4429 appear to have smaller sizes (7–50 pc), lower gaseous masses ($0.3–8 \times 10^5\,{\rm M}_\odot$), higher gaseous mass surface densities (40–650 $\rm M_\odot\,pc^{-2}$), and higher observed linewidths (2–16 $\rm km\,s^{-1}$) than the GMCs of the MW disc and other Local Group galaxies.

(ii) Cloud properties exhibit several trends with galactocentric distance. Specifically, except for the three innermost resolved clouds at $R_{\rm gal} < 100$ pc, the GMCs at small radii tend to have smaller sizes, lower gaseous masses, higher gaseous mass surface densities, and higher observed linewidths than clouds farther out. However, we also find that all these quantities drop abruptly in the outermost region of the molecular gas disc ($R_{\rm gal} \gtrsim 375$ pc).

(iii) The GMCs of NGC 4429 appear to be elongated (mean axial ratio of $\approx 2.3 \pm 0.2$) and are preferentially aligned in the radial direction (i.e. towards the galactic centre). The clouds also appear to be flattened in the plane of the galaxy.

(iv) The cloud mass distribution follows a truncated power law with slope -2.18 ± 0.21 and truncation mass $(8.8 \pm 1.3) \times 10^5\,{\rm M}_\odot$, suggesting most of the molecular mass of NGC 4429 is in low-mass clouds. We find a slight variation of the mass spectrum with galactocentric distance, suggesting massive clouds are more favoured at intermediate radii ($220 < R_{\rm gal} < 330$ pc).

(v) Strong velocity gradients are observed within individual GMCs ($\omega \approx 0.05–0.91\,{\rm km\,s^{-1}\,pc^{-1}}$), significantly larger than those of GMCs in the MW and other Local Group galaxies. A steep size–linewidth relation (with a power-law index 0.82 ± 0.13) and large observed virial parameters ($\langle\alpha_{\rm obs,vir}\rangle \approx 4.04 \pm 0.22$) are also found for the clouds of NGC 4429. However, we argue the large velocity gradients, steep size–linewidth relation and large observed virial parameters are all a consequence of gas motions driven by the background galactic potential (i.e. local circular orbital rotation), not the clouds' self-gravity. To remove the contribution of galaxy rotation from the clouds' linewidths and derive linewidths quantifying turbulence only, we measure the gradient-subtracted linewidths of the clouds $\sigma_{\rm gs,los}$. Using this measure, an internal virial equilibrium appears to have been reached betweem the clouds' turbulent kinetic energies ($E_{\rm turb}$) and their self-gravitational energies ($U_{\rm sg}$), i.e. $\langle\alpha_{\rm sg,vir}\rangle \approx \langle\alpha_{\rm gs,vir}\rangle \approx 1.28 \pm 0.04$.

(vi) However, we argue that neither $\alpha_{\rm obs,vir}$ nor $\alpha_{\rm sg,vir}$ reflects the true dynamical state of a cloud. We thus discuss and revisit the conventional virial theorem, deriving a modified theorem that explicitly takes into account both the self-gravity of the clouds and the effects of the external (galactic) gravitational potential in the vertical direction and the plane separately. This allows us to define an effective velocity dispersion $\sigma_{\rm eff,los}$ and an effective virial parameter $\alpha_{\rm eff,vir} \equiv \alpha_{\rm sg,vir} + \frac{E_{\rm ext}}{|U_{\rm sg}|}$, that provide straightforward measurable diagnostics of cloud boundedness in the presence of a non-negligeable external potential.

(vii) Using our new diagnostics, we find the contributions of external gravity to the clouds' energy budgets $E_{\rm ext}$ are generally much larger than zero. This is because the bulk motions of the clouds

are dominated by gravitational shear motions rather than epicyclic motions. The clouds of NGC 4429 are in a critical state in which the energy contributed by external gravity $E_{\rm ext}$ is approximately equal to the self-gravitational energy, i.e. $\frac{E_{\rm ext}}{|U_{\rm sg}|} \approx 1$. As such, the clouds are not virialized but remain marginally gravitationally bound, with a mean effective virial parameter ($\langle\alpha_{\rm eff,vir}\rangle \approx 2.15 \pm 0.12$ and $\langle\alpha^{\rm mod}_{\rm eff,vir}\rangle \approx 2.02 \pm 0.03$) close to the threshold between gravitationally bound and unbound objects ($\alpha_{\rm vir,crit} = 2$). This is also true when the elongated shapes of the clouds are taken into account ($\langle\alpha_{\rm eff,vir}\rangle \approx 2.65 \pm 0.15$ and $\langle\alpha^{\rm mod}_{\rm eff,vir}\rangle \approx 2.46 \pm 0.06$ for ellipsoidal clouds). As the clouds appear to reach an equilibrium between self-gravity and external gravity, they also have sizes consistent with their tidal radii (i.e. $R_{\rm c} \approx R_{\rm t}$) and are radially elongated (with an average axial ratio of $\approx$2). Overall, external gravity appears to be as important as self-gravity to regulate the morphologies, dynamics and thus ultimately the fates of the clouds.

(viii) Galactic rotational shear appears to play a dominant role to regulate the properties of the clouds of NGC 4429. Our shear model predicts that, as rotational shear increases, the contribution of external gravity to a cloud's energy budget $E^{\rm mod}_{\rm ext}$ also increases and the cloud becomes less bound, leading to a maximum size (or equivalently a minimum gaseous mass surface density) for the cloud to remain marginally bound: $R_{\rm shear} \approx 3\pi b_{\rm s} G\Sigma_{\rm gas}/4b_{\rm e}A_0^2$ ($\Sigma_{\rm shear} \approx 4b_{\rm e}A_0^2 R_{\rm c}/3\pi b_{\rm s} G$), which matches very well the observed sizes of the clouds of NGC 4429.

DATA AVALABILITY

The data underlying this article are available in the ALMA archive (https://almascience.eso.org/asax/) under project code 2013.1.00493.S.

ACKNOWLEDGEMENTS

We thank Michele Cappellari, Marc Sarzi, Christopher McKee, and James Binney for valuable discussions. MB was supported by STFC consolidated grant 'Astrophysics at Oxford' ST/H002456/1 and ST/K00106X/1. TAD acknowledges support from an STFC Ernest Rutherford Fellowship. MDS acknowledges support from a STFC DPhil studentship ST/N504233/1. KO was supported by Shimadzu Science and Technology Foundation. This publication arises from research funded by the John Fell Oxford University Press Research Fund.

This paper uses the following ALMA data: ADS/JAO.ALMA#2013.1.00493.S. ALMA is a partnership of ESO (representing its member states), NSF (USA), and NINS (Japan), together with NRC (Canada) and NSC and ASIAA (Taiwan) and KASI (Republic of Korea), in cooperation with the Republic of Chile. The Joint ALMA Observatory is operated by ESO, AUI/NRAO, and NAOJ. This paper also uses observations made with the NASA/ESA *HST*, and obtained from the Hubble Legacy Archive, which is a collaboration between the Space Telescope Science Institute (STScI/NASA), the Space Telescope European Coordinating Facility (ST-ECF/ESA), and the Canadian Astronomy Data Centre (CADC/NRC/CSA). This research has used the NASA/IPAC Extragalactic Database (NED), which is operated by the Jet Propulsion Laboratory, California Institute of Technology, under contract with the National Aeronautics and Space Administration.

REFERENCES

Adelman-McCarthy J. K. et al., 2008, ApJS, 175, 297
Alatalo K. et al., 2013, MNRAS, 432, 1796
Ballesteros-Paredes J., 2006, MNRAS, 372, 443
Ballesteros-Paredes J., Gazol A., Kim J., Klessen R. S., Jappsen A.-K., Tejero E., 2006, ApJ, 637, 384
Ballesteros-Paredes J., Klessen R. S., Mac Low M.-M., Vazquez-Semadeni E., 2007, in Reipurth B., Jewitt D., Keil K., eds, Protostars and Planets V. Univ. Arizona Press, Tucson, AZ, p. 63
Ballesteros-Paredes J., Gómez G. C., Pichardo B., Vázquez-Semadeni E., 2009, MNRAS, 393, 1563
Ballesteros-Paredes J., Hartmann L. W., Vázquez-Semadeni E., Heitsch F., Zamora-Avilés M. A., 2011, MNRAS, 411, 65
Bertoldi F., McKee C. F., 1992, ApJ, 395, 140
Binney J., 2020, MNRAS, 496, 767
Binney J., Tremaine S., 2008, Galactic Dynamics, 2nd edn. Princeton Univ. Press, Princeton
Blitz L., 1993, in Levy E. H., Lunine J. I., eds, Protostars and Planets III. University of Arizona Press, Tucson, Arizona, p. 125
Blitz L., Fukui Y., Kawamura A., Leroy A., Mizuno N., Rosolowsky E., 2007, Protostars and Planets V. University of Arizona Press, Tucson, p. 81
Bolatto A. D., Leroy A. K., Rosolowsky E., Walter F., Blitz L., 2008, ApJ, 686, 948
Bolatto A. D., Wolfire M., Leroy A. K., 2013, ARA&A, 51, 207
Burkert A., Bodenheimer P., 2000, ApJ, 543, 822
Camacho V., Vázquez-Semadeni E., Ballesteros-Paredes J., Gómez G. C., Fall S. M., Mata-Chávez M. D., 2016, ApJ, 833, 113
Cappellari M., 2002, MNRAS, 333, 400
Cappellari M., 2008, MNRAS, 390, 71
Cappellari M. et al., 2011, MNRAS, 416, 1680
Cappellari M. et al., 2013, MNRAS, 432, 1862
Chen X., Amaro-Seoane P., Cuadra J., 2016, ApJ, 819, 138
Colombo D. et al., 2014, ApJ, 784, 3
Colombo D. et al., 2018, MNRAS, 483, 4291
Dale J. E., Kruijssen J. M. D., Longmore S. N., 2019, MNRAS, 486, 3307
Dame T. M., Hartmann D., Thaddeus P., 2001, ApJ, 547, 792
Davis T. A., 2014, MNRAS, 445, 2378
Davis T. A. et al., 2011, MNRAS, 417, 882
Davis T. A. et al., 2013, MNRAS, 429, 534
Davis T. A., Bureau M., Onishi K., Cappellari M., Iguchi S., Sarzi M., 2017, MNRAS, 468, 4675
Davis T. A. et al., 2018, MNRAS, 473, 3818
Dib S., Helou G., Moore T. J. T., Urquhart J. S., Dariush A., 2012, ApJ, 758, 125
Donovan Meyer J. et al., 2012, ApJ, 744, 42
Donovan Meyer J. et al., 2013, ApJ, 772, 107
Elmegreen B. G., 1989, ApJ, 338, 178
Elmegreen B. G., Falgarone E., 1996, ApJ, 471, 816
Emsellem E., Monnet G., Bacon R., 1994, A&A, 285, 723
Emsellem E. et al., 2011, MNRAS, 414, 888
Engargiola G., Plambeck R. L., Rosolowsky E., Blitz L., 2003, ApJS, 149, 343
Faesi C. M., Lada C. J., Forbrich J., 2016, ApJ, 821, 125
Faesi C. M., Lada C. J., Forbrich J., 2018, ApJ, 857, 19
Falgarone E., Phillips T. G., Walker C. K., 1991, ApJ, 378, 186
Field G. B., Blackman E. G., Keto E. R., 2008, MNRAS, 385, 181
Field G. B., Blackman E. G., Keto E. R., 2011, MNRAS, 416, 710
Fleck R. C., Jr., 1980, ApJ, 242, 1019
Fleck R. C., Jr., Clark F. O., 1981, ApJ, 245, 898
Fukui Y. et al., 2008, ApJS, 178, 56
Gammie C. F., Ostriker J. P., Jog C. J., 1991, ApJ, 378, 565
Goldreich P., Lynden-Bell D., 1965, MNRAS, 130, 125
Goldreich P., Tremaine S., 1982, ARA&A, 20, 249
Gratier P. et al., 2012, A&A, 542, A108
Hennebelle P., Chabrier G., 2013, ApJ, 770, 150
Henshaw J. D. et al., 2019, MNRAS, 485, 2457
Heyer M., Krawczyk C., Duval J., Jackson J. M., 2009, ApJ, 699, 1092

Hirota A., Kuno N., Sato N., Nakanishi H., Tosaki T., Sorai K., 2011, ApJ, 737, 40
Hughes A. et al., 2010, MNRAS, 406, 2065
Hughes A. et al., 2013, ApJ, 779, 46
Ibáñez-Mejía J. C., Mac Low M.-M., Klessen R. S., Baczynski C., 2016, ApJ, 824, 41
Imara N., Blitz L., 2011, ApJ, 732, 78
Imara N., Faesi C. M., 2019, ApJ, 876, 141
Imara N., Bigiel F., Blitz L., 2011, ApJ, 732, 79
Julian W. H., Toomre A., 1966, ApJ, 146, 810
Kauffmann J., Pillai T., Zhang Q., 2013, ApJ, 765, L35
Kauffmann J., Pillai T., Zhang Q., Menten K. M., Goldsmith P. F., Lu X., Guzmán A. E., 2017, A&A, 603, A89
Koda J., Sawada T., Hasegawa T., Scoville N. Z., 2006, ApJ, 638, 191
Koyama H., Ostriker E. C., 2009, ApJ, 693, 1346
Kruijssen J. M. D. et al., 2019, MNRAS, 484, 5734
Larson R. B., 1981, MNRAS, 194, 809
Lequeux J., 2005, The Interstellar Medium. Springer, Astronomy and astrophysics library, Berlin
Leroy A. K. et al., 2015, ApJ, 801, 25
Leroy A. K. et al., 2016, ApJ, 831, 16
Lin G., Chawla M., Olson K., Barnes C., Guzowsk J., Bjornss C., Shain W., Roysam B., 2007, Cytometry A, 71, 724
Lombardi M., Alves J., Lada C. J., 2010, A&A, 519, L7
Mac Low M.-M., Klessen R. S., 2004, Rev. Mod. Phys., 76, 125
MacLaren I., Richardson K. M., Wolfendale A. W., 1988, ApJ, 333, 821
McKee C. F., 1989, ApJ, 345, 782
McKee C. F., 1999, in Lada C. J., Kylafis N. D., eds, NATO Advanced Study Institute (ASI) Series C Vol. 540, The Origin of Stars and Planetary Systems. Kluwer Academic Publishers, p. 29
Meidt S. E., 2016, ApJ, 818, 69
Meidt S. E. et al., 2013, ApJ, 779, 45
Meidt S. E. et al., 2015, ApJ, 806, 72
Meidt S. E. et al., 2018, ApJ, 854, 100
Melchior A.-L., Combes F., 2017, A&A, 607, L7
Miura R. E., Espada D., Hirota A., Nakanishi K., Bendo G. J., Sugai H., 2018, ApJ, 864, 120
Miville-Deschenes M. A., Murray N., Lee E. J., 2017, ApJ, 834, 57
Miville-Deschênes M.-A., Murray N., Lee E. J., 2017b, ApJ, 834, 57
Muller E. et al., 2010, ApJ, 712, 1248
North E. V. et al., 2019, MNRAS, 473, 3818
Nyland K. et al., 2016, MNRAS, 458, 2221
Oka T., Hasegawa T., Sato F., Tsuboi M., Miyazaki A., Sugimoto M., 2001, ApJ, 562, 348
Onishi K., Iguchi S., Davis T. A., Bureau M., Cappellari M., Sarzi M., Blitz L., 2017, MNRAS, 468, 4663
Padoan P., Haugbølle T., Nordlund Å., Frimann S., 2017, ApJ, 840, 48
Pan H.-A., Kuno N., 2017, ApJ, 839, 133
Phillips J. P., 1999, A&AS, 134, 241
Rebolledo D., Wong T., Xue R., Leroy A., Koda J., Donovan Meyer J., 2015, ApJ, 808, 99
Rice T. S., Goodman A. A., Bergin E. A., Beaumont C., Dame T. M., 2016, ApJ, 822, 52
Rosolowsky E., 2005, PASP, 117, 1403
Rosolowsky E., 2007, ApJ, 654, 240
Rosolowsky E., Blitz L., 2005, ApJ, 623, 826
Rosolowsky E., Leroy A., 2006, PASP, 118, 590
Rosolowsky E., Engargiola G., Plambeck R., Blitz L., 2003, ApJ, 599, 258
Rosolowsky E., Keto E., Matsushita S., Willner S. P., 2007, ApJ, 661, 830
Rousseeuw P., Driessen K., 2006, Data Min. Knowl. Discovery, 12, 29
Schruba A., Kruijssen J. M. D., Leroy A. K., 2019, ApJ, 883, 2
Smith M. D. et al., 2019, MNRAS, 473, 3818
Smith M. D. Bureau M. Davis T. A. Cappellari M. Liu L. Onishi K. Iguchi S. North E. et al. 2021a, MNRAS, 503, 5984
Smith M. D. Bureau M Davis T. A. Cappellari M. Liu L. Onishi K. Iguchi S. North E. V. et al., 2021b, MNRAS, 500, 1933
Solomon P. M., Rivolo A. R., Barrett J., Yahil A., 1987, ApJ, 319, 730
Stark A. A., Blitz L., 1978, ApJ, 225, L15
Strong A. W. et al., 1988, A&A, 207, 1
Sun J. et al., 2018, ApJ, 860, 172
Tan J. C., 2000, ApJ, 536, 173
Tasker E. J., Tan J. C., 2009, ApJ, 700, 358
Thilliez E., Maddison S. T., Hughes A., Wong T., 2014, Publ. Astron. Soc. Aust., 31, e003
Tosaki T. et al., 2017, PASJ, 69, 18
Utomo D., Blitz L., Davis T., Rosolowsky E., Bureau M., Cappellari M., Sarzi M., 2015, ApJ, 803, 16
Utreras J. et al., 2020, ApJ, 892, 94
Verschuur G. L., 1993, AJ, 106, 2580
Williams J. P., de Geus E. J., Blitz L., 1994, ApJ, 428, 693
Wong T. et al., 2011, ApJS, 197, 16
Wong T. et al., 2019, ApJ, 885, 50
Wu Y.-L., Sakamoto K., Pan H.-A., 2017, ApJ, 839, 6
Yang H., Ahuja N., 2014, Pattern Recognit., 47, 2266
Young L. M. et al., 2011, MNRAS, 414, 940
Yusef-Zadeh F., Wardle M., Schödel R., Roberts D. A., Cotton W., Bushouse H., Arendt R., Royster M., 2016, ApJ, 819, 60

SUPPORTING INFORMATION

Supplementary data are available at *MNRAS* online.

Table 1. Observed properties of the clouds in NGC 4429.
Table 3. Derived properties of the clouds in NGC 4429.

Please note: Oxford University Press is not responsible for the content or functionality of any supporting materials supplied by the authors. Any queries (other than missing material) should be directed to the corresponding author for the article.

APPENDIX A: MODIFIED VIRIAL THEOREM

Our goal in this appendix is to derive an MVT that encompasses not only a cloud's self-gravity but also the effects of the external (i.e. galactic) potential. We thus envision each cloud as a continuous structure with well-defined borders in position and velocity space, located in a rotating gas disc with a circular velocity determined by an axisymmetric background galactic gravitational potential ($\Phi_{\rm gal}$). We assume each cloud has a homogeneous density distribution and an ellipsoidal geometry. The cloud's CoM and its two semi-axes (semimajor axis $X_{\rm c}$ and semiminor axis $Y_{\rm c}$) are assumed to be located in the orbital plane (i.e. the mid-plane of the galaxy disc; see Fig. A1). We assume each fluid element of a cloud experiences two kinds of motions: (1) random turbulent motions (velocity dispersion $\sigma_{\rm sg}$) arising from self-gravity (i.e. the cloud's own gravitational potential $\Phi_{\rm sg}$) and (2) bulk gravitational motions (velocity $\vec{v}_{\rm gal}$ and RMS velocity $\sigma_{\rm gal}$) arising from the external gravity (i.e. the galactic gravitational potential $\Phi_{\rm gal}$). We neglect thermal motions, as they are often small compared to turbulent motions in a cold gas cloud (e.g. Fleck 1980). The turbulent motions due to self-gravity are expected to be quasi-isotropic in three dimensions (Field et al. 2008; Ballesteros-Paredes et al. 2011), while the gas motions induced by the external gravitational potential are often non-isotropic (Meidt et al. 2018). We assume the cloud's own gravitational potential $\Phi_{\rm sg}$ to be (statistically) independent of the local external gravitational potential $\Phi_{\rm gal}$, and the motions due to self-gravity ($\sigma_{\rm sg}$) to be uncorrelated with the motions due to external gravitational potential ($\sigma_{\rm gal}$), as suggested by Meidt et al. (2018). We ignore external pressure and magnetic fields, and consider only the effects of self-gravity and external gravity.

Assuming the surface terms are negligible (Larson 1981), the general form of the virial theorem for a cloud is

$$\frac{\ddot{I}}{2} = 2E_{\rm k} + \int_V (\vec{a}(\vec{d}) \cdot \vec{d}) {\rm d}m \tag{A1}$$

(see e.g. equations 14.6 and 14.7 of Lequeux 2005), where I is the cloud's moment of inertia, $E_{\rm k}$ its total kinetic energy, $\vec{d}$ the position vector of a fluid element inside the cloud with respect to the cloud's CoM, $\vec{a} \equiv \ddot{\vec{d}}$ the acceleration of the fluid element inside the cloud, ${\rm d}m \equiv \rho {\rm d}V$ the mass of the fluid element, and the integral is taken over all fluid elements within the volume V of the cloud of total mass M ($\int_V {\rm d}m = M$). We use $\vec{d}$ rather than the usual variable $\vec{r}$ to avoid confusion with the position vector (with respect to the galactic centre) in the plane of the disc $\vec{R}$ and its associated magnitude R, where $\vec{R}_0$ and R_0 are evaluated at the cloud's CoM (see Fig. A1). The equilibrium condition associated with equation (A1) should be that the time-averaged $\ddot{I}(t)$ is equal to zero, i.e. $\langle \ddot{I}(t) \rangle = 0$ (McKee 1999; Binney & Tremaine 2008). However, it is unclear how one can evaluate the resulting long-term average if the system is not in a time-independent state. We therefore adopt instead the instantaneous equilibrium condition $\ddot{I} = 0$, commonly adopted across several works (e.g. Lequeux 2005; Ballesteros-Paredes 2006). As such, $\ddot{I} > 0$ indicates that the cloud is expanding, while $\ddot{I} < 0$ indicates that the cloud is contracting (Ballesteros-Paredes 2006).

The above virial equation can be split into two independent parts based on our assumptions that $\Phi_{\rm sg}$ and $\Phi_{\rm gal}$ are independent (i.e. $\vec{a} = -\nabla\Phi_{\rm sg} + \vec{a}_{\rm ext}$, where $\vec{a}_{\rm ext}$ is the external acceleration due to galactic forces only) and $\sigma_{\rm sg}$ and $\sigma_{\rm gal}$ are uncorrelated [i.e. $E_{\rm k} = \frac{1}{2}M(\sigma_{\rm sg}^2 + \sigma_{\rm gal}^2)$]:

$$\frac{\ddot{I}}{2} = \left[3M\sigma_{\rm sg,los}^2 + \int_V (-\nabla\Phi_{\rm sg}(\vec{d}) \cdot \vec{d}) {\rm d}m\right] + \left[M\sigma_{\rm gal}^2 + \int_V (\vec{a}_{\rm ext}(\vec{d}) \cdot \vec{d}) {\rm d}m\right], \tag{A2}$$

where $\sigma_{\rm sg,los}$ is the line-of-sight (i.e. 1D) turbulent velocity dispersion due to self-gravity ($\sigma_{\rm sg,los}^2 \equiv \frac{1}{3}\sigma_{\rm sg}^2$) and $\sigma_{\rm gal}$ the RMS velocity of gravitational motions associated with external gravity ($\sigma_{\rm gal} \equiv \frac{1}{M}\int_V (\vec{v}_{\rm gal} - \overline{\vec{v}}_{\rm gal})^2 {\rm d}m$, where $\overline{\vec{v}}_{\rm gal}$ is the mean velocity of the cloud's gravitational motions due to external gravity). The first term in square brackets on the right-hand side of equation (A2) comprises the energy terms regulated by self-gravity, while the second term in square brackets contains the contribution of external gravity to the cloud's energy budget $E_{\rm ext}$.

Self-gravity. The integration of the self-gravity term on the right-hand side of equation (A2) is straightforward:

$$\int_V (-\nabla\Phi_{\rm sg}(\vec{d}) \cdot \vec{d}) {\rm d}m = -\frac{3b_{\rm s}GM^2}{R_{\rm c}}, \tag{A3}$$

where G is the gravitational constant, $R_{\rm c}$ the measured cloud's radius ($R_{\rm c} \equiv \sqrt{X_{\rm c}Y_{\rm c}}$), and $b_{\rm s}$ a geometrical factor that quantifies the effects of inhomogeneities and/or non-sphericity of the cloud mass distribution on its self-gravitational energy. For a cloud in which the isodensity contours are homoeoidal ellipsoids, $b_{\rm s} = b_{\rm s_1}b_{\rm s_2}$, where $b_{\rm s_1}$ quantifies the effects of the inhomogeneities and $b_{\rm s_2}$ those of the ellipticity. Bertoldi & McKee (1992) derived $b_{\rm s_1} = \frac{(1-\psi/3)}{(5-2\psi)}$ for a cloud with a radial mass volume density profile $\rho(r) \propto r^{-\psi}$, while $b_{\rm s_2} = \frac{R_{\rm m}}{R_{\rm d}}\frac{\arcsin(e)}{e}$ for an ellipsoidal cloud, where $R_{\rm m}$ is the observed (i.e. projected) cloud radius averaged over all possible cloud orientations (i.e. averaged over 4π steradians), $R_{\rm d}$ is the deprojected cloud radius, and e is the cloud's eccentricity ($e \equiv \sqrt{1-(Y_{\rm c}/X_{\rm c})^2}$). The $R_{\rm m}/R_{\rm d}$ ratio depends on the cloud's aspect ratio $Z_{\rm c}/\sqrt{X_{\rm c}Y_{\rm c}}$, where $Z_{\rm c}$ is the cloud's scale height, and $R_{\rm m}/R_{\rm d} = 1$ when $Z_{\rm c}/\sqrt{X_{\rm c}Y_{\rm c}} = 1$ (see fig. 2 in Bertoldi & McKee 1992). For a homogeneous spherical cloud, $b_{\rm s} = \frac{1}{5}$.

An equation suitable for a cloud regulated by self-gravity only is thereby obtained:

$$\frac{\ddot{I}}{2} = 3M\sigma_{\rm sg,los}^2 - \frac{3b_{\rm s}GM^2}{R_{\rm c}}. \tag{A4}$$

For a self-gravitating cloud in equilibrium (i.e. $\ddot{I} = 0$), this yields

$$\sigma_{\rm sg,los}^2 = b_{\rm s}GM/R_{\rm c}, \tag{A5}$$

or equivalently

$$M = \frac{\sigma_{\rm sg,los}^2 R_{\rm c}}{b_{\rm s}G} \equiv M_{\rm sg,vir} \tag{A6}$$

(cf. equation 7).

External gravity. The contribution of external gravity to a cloud's energy budget is given by the second term in square brackets on the right-hand side of equation (A2):

$$E_{\rm ext} = M\sigma_{\rm gal}^2 + \int_V (\vec{a}_{\rm ext}(\vec{d}) \cdot \vec{d}) {\rm d}m. \tag{A7}$$

If we assume the gravitational motions in the plane to be separable from those in the vertical direction (perpendicular to the orbital plane), the above equation can easily be separated into two parts, one in the vertical direction ($E_{\rm ext,z}$) and the other in the orbital plane

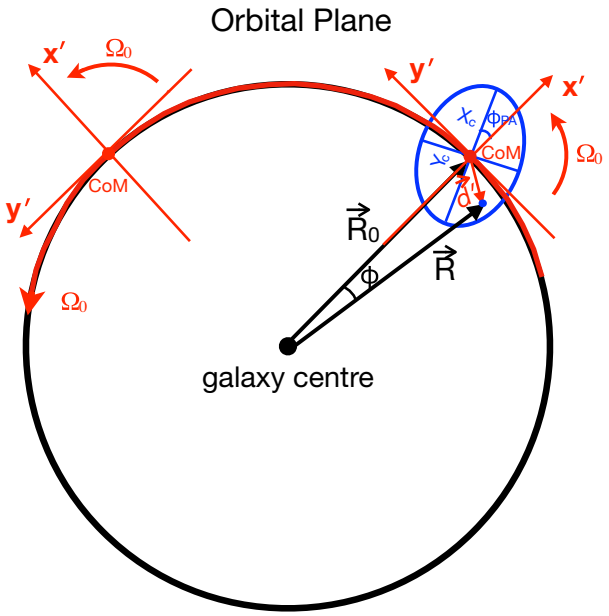

Figure A1. Schematic diagram of our rotating frame of reference in the orbital plane (i.e. the mid-plane of the galaxy disc). This rotating frame is a local Cartesian coordinate system centred at the cloud's CoM, which both orbits around the galaxy centre with the cloud's CoM (with angular velocity Ω_0, the circular orbital angular velocity of the cloud's CoM) and rotates on itself (with the same angular velocity Ω_0), such that the x'-axis always points in the direction of increasing galactocentric radius and the y'-axis always points in the direction of the orbital rotation at the cloud's CoM. We assume a homogenous ellipsoidal cloud, whose semimajor axis $X_{\rm c}$ and semiminor axis $Y_{\rm c}$ are located in the orbital plane. The semimajor axis $X_{\rm c}$ makes an angle $\phi_{\rm PA}$ with respect to the radial (i.e. $\hat{x}'$ or $\vec{R}_0$) direction.

($E_{\rm ext,plane}$):

$$E_{\rm ext} = \underbrace{\left(M\sigma^2_{\rm gal,z} + \int_V (a_{\rm ext,z} d_{\rm z}) {\rm d}m\right)}_{\text{external, vertical direction}} + \underbrace{\left(M\sigma^2_{\rm gal,plane} + \int_V (\vec{a}_{\rm ext,plane} \cdot \vec{d}_{\rm plane}) {\rm d}m\right)}_{\text{external, plane}}, \quad \text{(A8)}$$

where $\sigma^2_{\rm gal,z}$, $a_{\rm ext,z}$, and $d_{\rm z}$ are the components of $\sigma^2_{\rm gal}$, $\vec{a}_{\rm ext}$, and $\vec{d}$ along the vertical direction, respectively, and $\sigma^2_{\rm gal,plane}$, $\vec{a}_{\rm ext,plane}$,and $\vec{d}_{\rm plane}$ are the components of $\sigma^2_{\rm gal}$, $\vec{a}_{\rm ext}$, and $\vec{d}$ in the orbital plane, respectively.

We derive $E_{\rm ext,z}$ (the first term on the right-hand side of equation A8) in Appendix A1 (see equation A21) for a homogenous ellipsoidal cloud whose semimajor axis $X_{\rm c}$ and semiminor axis $Y_{\rm c}$ are located in the orbital plane, yielding

$$E_{\rm ext,z} \approx M\left(\sigma^2_{\rm gal,z} - b_{\rm e}\nu_0^2 Z_{\rm c}^2\right), \quad \text{(A9)}$$

where as before $Z_{\rm c}$ is the scale height of the cloud ($Z_{\rm c} = \sqrt{X_{\rm c}Y_{\rm c}} \equiv R_{\rm c}$ for a spherical cloud), $\nu_0^2 \equiv 4\pi G\rho_{*,0}$ (formally the total mass volume density evaluated at the cloud's CoM, but we use here $\rho_{*,0}$, the stellar mass volume density ρ_* evaluated at the cloud's CoM using our MGE model, as it is accurately constrained; see Appendix C), and $b_{\rm e}$ is a geometrical factor that quantifies the effects of inhomogeneities of the cloud mass distribution (analogously to $b_{\rm s_l}$ but for the external gravity term; $b_{\rm e} = \frac{1}{5}$ again for a homogeneous cloud).

Similarly, we derive $E_{\rm ext,plane}$ (the second term on the , of equation A8) for a homogenous ellipsoidal cloud in Appendix A2 (see equation A36), yielding

$$E_{\rm ext,plane} \approx M\left(\sigma^2_{\rm gal,r} + \sigma^2_{\rm gal,t} + b_{\rm e}T_0\left(X_{\rm c}^2\cos^2\phi_{\rm PA} + Y_{\rm c}^2\sin^2\phi_{\rm PA}\right) - b_{\rm e}\Omega_0^2\left(X_{\rm c}^2 + Y_{\rm c}^2\right)\right), \quad \text{(A10)}$$

where $\sigma^2_{\rm gal,r}$ and $\sigma^2_{\rm gal,t}$ are the RMS velocities of gas motions due to external gravity in, respectively, the radial (i.e. $\hat{r}$ the direction pointing from the galaxy centre to the cloud's CoM, thus parallel to $\vec{R}_0$) and the azimuthal (i.e. $\hat{t}$, the direction along the orbital rotation, thus perpendicular to $\hat{r}$ and $\vec{R}_0$) direction as measured in an inertial frame (i.e. by a distant observer), ($\sigma^2_{\rm gal,r} + \sigma^2_{\rm gal,t}$) is thus the RMS velocity of in-plane gravitational motions (i.e. $\sigma^2_{\rm gal,plane}$) measured in the inertial frame, $\phi_{\rm PA}$ is the angle the semimajor axis $X_{\rm c}$ makes with respect to the radial (i.e. $\hat{r}$ or $\vec{R}_0$) direction (see Fig. A1), Ω_0 is the circular orbital angular velocity of the cloud's CoM, $T_0 \equiv -R\frac{{\rm d}\Omega^2(R)}{{\rm d}R}|_{R=R_0}$ (e.g. Stark & Blitz 1978) is the tidal acceleration per unit length in the radial direction T evaluated at the cloud's CoM, and R is the galactocentric distance in the plane of the disc, while R_0 is that at the cloud's CoM. We note that here and throughout, $\Omega(R)$ is the theoretical quantity $\Omega(R) \equiv \sqrt{\frac{1}{R}\frac{{\rm d}\Phi_{\rm gal}}{{\rm d}R}}$ defined by the galaxy potential $\Phi_{\rm gal}$, i.e. it is the angular velocity of a fluid element moving in perfect circular motion [$\Omega(R) = V_{\rm circ}(R)/R$, where $V_{\rm circ}(R)$ is the circular velocity curve] rather than the observed angular velocity of the fluid element [$V_{\rm rot}(R)/R$, where $V_{\rm rot}$ is the observed rotation curve]. For an axisymmetric cloud (i.e. $X_{\rm c} = Y_{\rm c} = R_{\rm c}$), we then have

$$E_{\rm ext,plane} \approx M\left(\sigma^2_{\rm gal,r} + \sigma^2_{\rm gal,t} + b_{\rm e}\left(T_0 - 2\Omega_0^2\right)R_{\rm c}^2\right). \quad \text{(A11)}$$

Combining equations (A9) and A10, we obtain the total contribution of external gravity to a cloud's energy budget:

$$\begin{aligned} E_{\rm ext} &= E_{\rm ext,z} + E_{\rm ext,plane} \\ &\approx M\left(\sigma^2_{\rm gal,z} - b_{\rm e}\nu_0^2 Z_{\rm c}^2\right) + M\left(\sigma^2_{\rm gal,r} + \sigma^2_{\rm gal,t}\right) \\ &\quad + M\left(b_{\rm e}T_0\left(X_{\rm c}^2\cos^2\phi_{\rm PA} + Y_{\rm c}^2\sin^2\phi_{\rm PA}\right) - b_{\rm e}\Omega_0^2\left(X_{\rm c}^2 + Y_{\rm c}^2\right)\right). \end{aligned} \quad \text{(A12)}$$

For an axisymmetric cloud (i.e. $X_{\rm c} = Y_{\rm c} = R_{\rm c}$), we then have

$$\begin{aligned} E_{\rm ext} &\approx M\left(\sigma^2_{\rm gal,z} - b_{\rm e}\nu_0^2 Z_{\rm c}^2\right) \\ &\quad + M\left(\sigma^2_{\rm gal,r} + \sigma^2_{\rm gal,t} + b_{\rm e}\left(T_0 - 2\Omega_0^2\right)R_{\rm c}^2\right). \end{aligned} \quad \text{(A13)}$$

Total. Substituting equation (A4) and (A12) into equation (A2), we obtain our final MVT for a homogenous ellipsoidal cloud:

$$\begin{aligned} \frac{\ddot{I}}{2} &= \left[3M\sigma^2_{\rm sg,los} - 3b_{\rm s}GM^2/R_{\rm c}\right] + E_{\rm ext} \\ &\approx \left[3M\sigma^2_{\rm sg,los} - 3b_{\rm s}GM^2/R_{\rm c}\right] + \left[M\left(\sigma^2_{\rm gal,z} - b_{\rm e}\nu_0^2 Z_{\rm c}^2\right)\right. \\ &\quad + M\left(\sigma^2_{\rm gal,r} + \sigma^2_{\rm gal,t} + b_{\rm e}T_0\left(X_{\rm c}^2\cos^2\phi_{\rm PA} + Y_{\rm c}^2\sin^2\phi_{\rm PA}\right)\right. \\ &\quad \left.\left. - b_{\rm e}\Omega_0^2\left(X_{\rm c}^2 + Y_{\rm c}^2\right)\right)\right]. \end{aligned} \quad \text{(A14)}$$

For an axisymmetric cloud (i.e. $X_{\rm c} = Y_{\rm c} = R_{\rm c}$), we then have

$$\frac{\ddot{I}}{2} \approx \underbrace{\left[3M\sigma^2_{\rm sg,los} - 3b_{\rm s}GM^2/R_{\rm c}\right]}_{\text{self gravity}} + \left[\underbrace{M\left(\sigma^2_{\rm gal,z} - b_{\rm e}\nu_0^2 Z_{\rm c}^2\right)}_{\text{external, vertical direction}} + \underbrace{M\left(\sigma^2_{\rm gal,r} + \sigma^2_{\rm gal,t} + b_{\rm e}\left(T_0 - 2\Omega_0^2\right)R_{\rm c}^2\right)}_{\text{external, plane}}\right]. \quad \text{(A15)}$$

A1 Calculating $E_{\rm ext,z}$

According to equation (A8), the contribution of external gravity to a cloud's energy budget in the vertical direction is

$$E_{\rm ext,z} = M\sigma^2_{\rm gal,z} + \int_V \left(a_{\rm ext,z} d_{\rm z}\right){\rm d}m. \quad \text{(A16)}$$

As we have assumed the cloud's CoM to be in the galaxy mid-plane, the component of the acceleration $\vec{a}_{\rm ext}$ in the vertical direction can be approximated to

$$\begin{aligned} a_{\rm ext,z} &= -\frac{\partial\Phi_{\rm gal}(\vec{d})}{\partial z} \\ &\approx -\left.\frac{\partial\Phi_{\rm gal}(\vec{d})}{\partial z}\right|_{z=0} - \left.\frac{\partial^2\Phi_{\rm gal}(\vec{d})}{\partial^2 z}\right|_{z=0} d_{\rm z} \\ &\approx -\left.\frac{\partial^2\Phi_{\rm gal}(\vec{d})}{\partial^2 z}\right|_{z=0} d_{\rm z}. \end{aligned} \quad \text{(A17)}$$

For a thin gas disc,

$$\left.\frac{\partial^2\Phi_{\rm gal}(\vec{d})}{\partial^2 z}\right|_{z=0} \approx 4\pi G\rho_*(R, z=0), \quad \text{(A18)}$$

and we further assume

$$\left.\frac{\partial^2\Phi_{\rm gal}(\vec{d})}{\partial^2 z}\right|_{z=0} \approx 4\pi G\rho_{*,0}, \quad \text{(A19)}$$

formally the total mass volume density, but we use here $\rho_*(R, z = 0)$, the stellar mass volume density in the mid-plane of the disc, that can be reliably estimated from observations (here our MGE model; see Appendix C), and again $\rho_{*,0} \equiv \rho_*(R = R_0, z = 0)$ is

evaluated at the cloud's CoM. As expected from Poisson's equation, equation (A18) only applies to a (thin) disc where the variations in the gravitational potential are larger in the vertical direction than in the plane (i.e. $\frac{\partial^2\Phi_{\rm gal}(\vec{d})}{\partial^2 z} \gg \frac{\partial^2\Phi_{\rm gal}(\vec{d})}{\partial^2 r}$ and $\frac{\partial^2\Phi_{\rm gal}(\vec{d})}{\partial^2 z} \gg \frac{\partial^2\Phi_{\rm gal}(\vec{d})}{\partial^2 t}$; see also Koyama & Ostriker 2009 and Meidt et al. 2018). Again as expected, given that ρ_* is positive, the gravitational potential of the galaxy along the z-axis always has a confining effect on the cloud, i.e. a fluid element moving away from the cloud's CoM will always experience a restoring force in the z-direction back towards the galactic (i.e. mid-) plane.

With these expressions (equations A17 and A19), the volume integral in the second term on the right-hand side of equation (A16) simplifies to $\int_V d_z^2\,{\rm d}m$. For an ellipsoidal cloud with semimajor axis $Z_{\rm c}$ in the vertical direction (i.e. along the z-axis),

$$\int_V d_{\rm z}^2\,{\rm d}m = b_{\rm e} M Z_{\rm c}^2, \tag{A20}$$

where $b_{\rm e}$ is the aforementioned geometrical factor that quantifies the effects of the density inhomogeneities for the external gravity term ($b_{\rm e} = \frac{1}{5}$ for a homogenous cloud).

Therefore, the total contribution of external gravity to the cloud's energy budget in the vertical direction is

$$E_{{\rm ext},z} \approx M\left(\sigma_{{\rm gal},z}^2 - b_{\rm e}\nu_0^2 Z_{\rm c}^2\right), \tag{A21}$$

where as before $\nu_0^2 \equiv 4\pi G\rho_{*,0}$.

A2 Calculating $E_{\rm ext,plane}$ in the rotating frame

In this section, we derive the contribution of external gravity to a cloud's energy budget in the orbital plane $E_{\rm ext,plane}$, using a frame of reference (x', y') that we will refer to as the 'rotating frame'. This rotating frame is a local Cartesian coordinate system centred at the cloud's CoM, which both orbits around the galaxy centre with the cloud's CoM (with angular velocity Ω_0) and rotates on itself (with the same angular velocity Ω_0), such that the x'-axis always points in the direction of increasing galactocentric radius and the y'-axis always points in the direction of orbital rotation at the cloud's CoM (see Fig. A1).

In the rotating frame, the contribution of external gravity to a cloud's energy budget in the plane is (cf. equation A8)

$$\begin{aligned} E_{\rm ext,plane} &= M\left(\sigma_{{\rm gal},x'}'^2 + \sigma_{{\rm gal},y'}'^2\right) + \int_V \left(a'_{{\rm ext},x'}x' + a'_{{\rm ext},y'}y'\right){\rm d}m \\ &= \underbrace{\left(M\sigma_{{\rm gal},x'}'^2 + \int_V (a'_{{\rm ext},x'}x')\,{\rm d}m\right)}_{E_{{\rm ext},x'}} \\ &\quad + \underbrace{\left(M\sigma_{{\rm gal},y'}'^2 + \int_V (a'_{{\rm ext},y'}y')\,{\rm d}m\right)}_{E_{{\rm ext},y'}}, \end{aligned} \tag{A22}$$

where $\sigma_{{\rm gal},x'}'^2$, $a'_{{\rm ext},x'}$, and x' are the components of $\sigma_{\rm gal}'^2$, $\vec{a}'_{\rm ext}$, and $\vec{d}'_{\rm plane}$ along the $\hat{x}'$-direction, respectively, similarly for $\sigma_{{\rm gal},y'}'^2$, $a'_{{\rm ext},y'}$, and y'. Here, $E_{{\rm ext},x'}$ and $E_{{\rm ext},y'}$ are the contributions of external gravity to the cloud's energy budget in the radial and the azimuthal direction, respectively.

In the rotating frame, the acceleration of a fluid element due to galactic forces (i.e. the galactic gravitational potential) is

$$\begin{aligned} \vec{a}'_{\rm ext,plane}(\vec{d}'_{\rm plane}) &= -\nabla\Phi_{\rm gal}(\vec{d}'_{\rm plane}) + \Omega_0^2\vec{R} - 2\vec{\Omega}_0 \times \vec{v}'_{\rm gal} \\ &= -\Omega^2(R)\vec{R} + \Omega_0^2\vec{R} - 2\vec{\Omega}_0 \times \vec{v}'_{\rm gal}, \end{aligned} \tag{A23}$$

where $\vec{v}'_{\rm gal} \equiv \dot{\vec{d}}'_{\rm plane} = v'_{{\rm gal},x'}\hat{x}' + v'_{{\rm gal},y'}\hat{y}'$ is the in-plane velocity of gravitational motions induced by the external potential as measured in the rotating frame. The last two terms on the right-hand side of equation (A23) represent the centrifugal and the Coriolis acceleration, respectively, as perceived in the rotating frame.

We then expand $\vec{a}'_{\rm ext,plane}$ from equation (A23) in the radial ($\hat{x}'$) and azimuthal ($\hat{y}'$) directions, and obtain

$$\begin{cases} a'_{{\rm ext},x'} = \left(-\Omega^2(R) + \Omega_0^2\right) R\cos\phi + 2\Omega_0 v'_{{\rm gal},y'}, \\ a'_{{\rm ext},y'} = \left(-\Omega^2(R) + \Omega_0^2\right) R\sin\phi - 2\Omega_0 v'_{{\rm gal},x'}, \end{cases} \tag{A24}$$

where ϕ is the angle between $\vec{R}$ and $\vec{R}_0$ (see Fig. A1). If we assume the size of the cloud to be much smaller than its galactocentric distance (i.e. $R_{\rm c} \ll R_0$), then $\cos\phi \approx 1$ and $\sin\phi \approx y'/R$. The accelerations $a'_{{\rm ext},x'}$ and $a'_{{\rm ext},y'}$ can thus be approximated to

$$\begin{cases} a'_{{\rm ext},x'} \approx \left(-\Omega^2(R)R + \Omega_0^2 R\right) + 2\Omega_0 v'_{{\rm gal},y'} \\ \qquad \approx \left(-\left(\Omega_0^2 R_0 + \dfrac{{\rm d}(\Omega^2 R)}{{\rm d}R}\Big|_{R=R_0}(R-R_0)\right)\right. \\ \qquad\quad \left. + \left(\Omega_0^2 R_0 + \dfrac{{\rm d}(\Omega_0^2 R)}{{\rm d}R}\Big|_{R=R_0}(R-R_0)\right)\right) + 2\Omega_0 v'_{{\rm gal},y'} \\ \qquad \approx \left(-\left(\Omega_0^2 R_0 + \left(\Omega_0^2 + R\dfrac{{\rm d}\Omega^2}{{\rm d}R}\Big|_{R=R_0}\right)x'\right)\right. \\ \qquad\quad \left. + \left(\Omega_0^2 R_0 + \Omega_0^2 x'\right)\right) + 2\Omega_0 v'_{{\rm gal},y'} \\ \qquad \approx -\left(R\dfrac{{\rm d}\Omega^2}{{\rm d}R}\Big|_{R=R_0}\right)x' + 2\Omega_0 v'_{{\rm gal},y'} \\ \qquad \approx T_0 x' + 2\Omega_0 v'_{{\rm gal},y'}, \\ a'_{{\rm ext},y'} \approx \left(-\Omega^2(R) + \Omega_0^2\right)y' - 2\Omega_0 v'_{{\rm gal},x'} \\ \qquad \approx \left(-\left(\Omega_0^2 + \dfrac{{\rm d}\Omega^2}{{\rm d}R}\Big|_{R=R_0}(R-R_0)\right) + \Omega_0^2\right)y' - 2\Omega_0 v'_{{\rm gal},x'} \\ \qquad \approx -\dfrac{{\rm d}\Omega^2}{{\rm d}R}\Big|_{R=R_0} x'y' - 2\Omega_0 v'_{{\rm gal},x'} \\ \qquad \approx -2\Omega_0 v'_{{\rm gal},x'}, \end{cases} \tag{A25}$$

where we have assumed $(R - R_0) \approx x'$ (as $R_{\rm c} \ll R_0$) and expanded $a'_{{\rm ext},x'}$ and $a'_{{\rm ext},y'}$ to first order in x' and y' (i.e. $x'^2 \approx 0$, $y'^2 \approx 0$, and $x'y' \approx 0$). The term $T_0 x'$ represents the tidal force (i.e. a combination of the external gravity and centrifugal force), which is exclusively in the radial direction, while the terms $2\Omega_0 v'_{{\rm gal},y'}$ and $-2\Omega_0 v'_{{\rm gal},x'}$ represent the Coriolis force, which is in both the radial and azimuthal directions.

It is worth noting that equation (A25) has solutions

$$\begin{cases} x' = {\rm S}_1\sin(\kappa_0 t + \varphi) + {\rm S}_2, \\ y' = \frac{2\Omega_0}{\kappa_0}\,{\rm S}_1\cos(\kappa_0 t + \varphi) - 2A_0\,{\rm S}_2\,t + S_3, \end{cases} \tag{A26}$$

where κ_0 is the epicyclic frequency evaluated at the cloud's CoM ($\kappa_0^2 \equiv (R\frac{{\rm d}\Omega^2(R)}{{\rm d}R} + 4\Omega^2(R))|_{R=R_0}$), A_0 is the Oort's constant A quantifying shear evaluated at the cloud's CoM ($A_0 \equiv -\frac{R}{2}\frac{{\rm d}\Omega(R)}{{\rm d}R}|_{R=R_0}$), and $\rm S_1$, $\rm S_2$, and $\rm S_3$ (as well as the arbitrary phase φ) are constants that depend on the given boundary (e.g. initial) conditions. Equation (A26) shows that the gravitational motions associated with external gravity have two contributions: epicyclic motions around the cloud's CoM (i.e. the 'guiding centre'; see e.g. Meidt et al. 2018), indicated by the trigonometric terms ${\rm S}_1\sin(\kappa_0 t + \varphi)$ and $\frac{2\Omega_0}{\kappa_0}\,{\rm S}_1\cos(\kappa_0 t + \varphi)$, and linear shear motion, indicated by the $-2A_0\,{\rm S}_2\,t$ term (e.g. Gammie et al. 1991; Tan 2000; Binney 2020). It is worth noting that, in a model where all fluid elements of a cloud move on perfectly circular

orbits (around the galaxy centre) determined by the galactic potential, the epicyclic amplitudes vanish and the gravitational motions are completely dominated by the shear motions (see equation B21).

To calculate $E_{\rm ext,x'}$ and $E_{\rm ext,y'}$ (and thus $E_{\rm ext,plane}$), we also need $\sigma'^2_{\rm gal,x'}$ and $\sigma'^2_{\rm gal,y'}$ measured in the rotating frame (see equation A22). However, as $\sigma'^2_{\rm gal,x'}$ and $\sigma'^2_{\rm gal,y'}$ cannot be obtained directly from observations, we instead calculate them from the RMS velocities of gravitational motions $\sigma^2_{\rm gal,r}$ and $\sigma^2_{\rm gal,t}$ measured in an inertial frame centred at the galaxy centre, which are related to the observed velocity dispersions $\sigma_{\rm obs,los}$ and $\sigma_{\rm gs,los}$ through equation (19).

To achieve this, we must first derive the velocity transformation between the chosen inertial frame and our rotating frame. The velocity of each fluid element due to gravitational motions in the inertial frame is $\vec{v}_{\rm gal,plane} \equiv \dot{\vec{R}} = \dot{\vec{R}}_0 + \dot{\vec{d}}_{\rm plane} = \vec{\Omega}_0 \times \vec{R}_0 + \dot{\vec{d}}_{\rm plane}$, where $\vec{d}_{\rm plane}$ is the in-plane position vector of the fluid element with respect to the cloud's CoM in the inertial frame (see Fig. A1). The time derivative of $\vec{d}_{\rm plane}$ is related to the time derivative of $\vec{d}'_{\rm plane}$ (i.e. $\vec{v}'_{\rm gal,plane}$, the velocity of the fluid element due to gravitational motions measured in the rotating frame; see equation A23) through the usual velocity transformation between an inertial and a rotating frame, i.e. $\dot{\vec{d}}_{\rm plane} = \dot{\vec{d}}'_{\rm plane} + \vec{\Omega}_0 \times \vec{d}_{\rm plane} = \vec{v}'_{\rm gal,plane} + \vec{\Omega}_0 \times \vec{d}_{\rm plane}$. We thus obtain $\vec{v}_{\rm gal,plane} = \vec{\Omega}_0 \times \vec{R}_0 + \vec{v}'_{\rm gal,plane} + \vec{\Omega}_0 \times \vec{d}_{\rm plane}$, or equivalently

$$\vec{v}'_{\rm gal,plane} = \vec{v}_{\rm gal,plane} - \vec{\Omega}_0 \times \vec{R}_0 - \vec{\Omega}_0 \times \vec{d}_{\rm plane}. \tag{A27}$$

Expanding $\vec{v}'_{\rm gal,plane}$ in the radial ($\hat{x}'$) and azimuthal ($\hat{y}'$) directions, we derive

$$\begin{cases} v'_{\rm gal,x'} = v_{\rm gal,r} + \Omega_0 d_{\rm t}, \\ v'_{\rm gal,y'} = v_{\rm gal,t} - \Omega_0 R_0 - \Omega_0 d_{\rm r}, \end{cases} \tag{A28}$$

where $v'_{\rm gal,x'}$ and $v'_{\rm gal,y'}$ are the velocities of the fluid element due to gravitational motions measured in the rotating frame along the radial ($\hat{x}'$) and the azimuthal ($\hat{y}'$) direction, respectively, $v_{\rm gal,r}$ and $v_{\rm galt}$ are the corresponding velocities measured in the inertial frame along the radial ($\hat{r}$ or $\vec{R}_0$) and the azimuthal ($\hat{t}$) direction, respectively, and $d_{\rm r}$ and $d_{\rm t}$ are the radial and the azimuthal component of $\vec{d}_{\rm plane}$ measured in the inertial frame, respectively. Using equation (A28), we thus derive the mean velocities $\overline{v'}_{\rm gal,x'}$ and $\overline{v'}_{\rm gal,y'}$ of the fluid elements as measured in the rotating frame:

$$\begin{cases} \overline{v'}_{\rm gal,x'} \equiv \dfrac{\int_V v'_{\rm gal,x'}\,{\rm d}m}{M} \\ \qquad = \dfrac{\int_V v_{\rm gal,r}\,{\rm d}m}{M} + \dfrac{\int_V (\Omega_0 d_{\rm t})\,{\rm d}m}{M} \\ \qquad = \overline{v}_{\rm gal,r}, \\ \overline{v'}_{\rm gal,y'} \equiv \dfrac{\int_V v'_{\rm gal,y'}\,{\rm d}m}{M} \\ \qquad = \dfrac{\int_V v_{\rm gal,t}\,{\rm d}m}{M} - \dfrac{\int_V (\Omega_0 R_0)\,{\rm d}m}{M} - \dfrac{\int_V (\Omega_0 d_{\rm r})\,{\rm d}m}{M} \\ \qquad = \overline{v}_{\rm gal,t} - \Omega_0 R_0, \end{cases} \tag{A29}$$

where $\overline{v}_{\rm gal,r}$ and $\overline{v}_{\rm gal,t}$ are the mean velocities of the fluid elements as measured in the inertial frame, and we have used $\int_V d_{\rm r}\,{\rm d}m = \int_V d_{\rm t}\,{\rm d}m = 0$ as a homogenous ellipsoidal cloud has been assumed.

With equations (A28) and (A29), the desired RMS velocities of the fluid elements measured in the rotating frame (i.e. $\sigma'^2_{\rm gal,x'}$ and $\sigma'^2_{\rm gal,y'}$) can thus be related to those measured in the inertial frame (i.e. $\sigma^2_{\rm gal,r}$ and $\sigma^2_{\rm gal,t}$):

$$\begin{cases} \sigma'^2_{\rm gal,x'} \equiv \dfrac{\int_V (v'_{\rm gal,x'} - \overline{v'}_{\rm gal,x'})^2\,{\rm d}m}{M} \\ \qquad = \dfrac{\int_V \left((v_{\rm gal,r} - \overline{v}_{\rm gal,r}) + \Omega_0 d_{\rm t}\right)^2\,{\rm d}m}{M} \\ \qquad = \sigma^2_{\rm gal,r} + \dfrac{\Omega_0^2 \int_V d_{\rm t}^2\,{\rm d}m}{M} + \dfrac{2\Omega_0 \int_V (v_{\rm gal,r} - \overline{v}_{\rm gal,r}) d_{\rm t}\,{\rm d}m}{M}, \\ \sigma'^2_{\rm gal,y'} \equiv \dfrac{\int_V (v'_{\rm gal,y'} - \overline{v'}_{\rm gal,y'})^2\,{\rm d}m}{M} \\ \qquad = \dfrac{\int_V \left((v_{\rm gal,t} - \overline{v}_{\rm gal,t}) - \Omega_0 d_{\rm r}\right)^2\,{\rm d}m}{M} \\ \qquad = \sigma^2_{\rm gal,t} + \dfrac{\Omega_0^2 \int_V d_{\rm r}^2\,{\rm d}m}{M} - \dfrac{2\Omega_0 \int_V (v_{\rm gal,t} - \overline{v}_{\rm gal,t}) d_{\rm r}\,{\rm d}m}{M}, \end{cases} \tag{A30}$$

where we have used $\sigma^2_{\rm gal,r} \equiv \frac{1}{M}\int_V (v_{\rm gal,r} - \overline{v}_{\rm gal,r})^2 {\rm d}m$ and $\sigma^2_{\rm gal,t} \equiv \frac{1}{M}\int_V (v_{\rm gal,t} - \overline{v}_{\rm gal,t})^2 {\rm d}m$.

Substituting equations (A25), (A28), and (A30) into equation (A22) yields

$$\begin{cases} E_{\rm ext,x'} = M\sigma^2_{\rm gal,r} + \left(T_0 - 2\Omega_0^2\right)\int_V d_{\rm r}^2\,{\rm d}m + \Omega_0^2 \int_V d_{\rm t}^2\,{\rm d}m \\ \qquad\qquad + 2\Omega_0 \int_V \left(v_{\rm gal,r} d_{\rm t} + v_{\rm gal,t} d_{\rm r}\right)\,{\rm d}m, \\ E_{\rm ext,y'} = M\sigma^2_{\rm gal,t} + \Omega_0^2 \int_V d_{\rm r}^2\,{\rm d}m - 2\Omega_0^2 \int_V d_{\rm t}^2\,{\rm d}m \\ \qquad\qquad - 2\Omega_0 \int_V (v_{\rm gal,r} d_{\rm t} + v_{\rm gal,t} d_{\rm r})\,{\rm d}m, \end{cases} \tag{A31}$$

where we have adopted $\int_V x'^2\,{\rm d}m = \int_V x' d_{\rm r}\,{\rm d}m = \int_V d_{\rm r}^2\,{\rm d}m$, $\int_V y' d_{\rm t}\,{\rm d}m = \int_V d_{\rm t}^2\,{\rm d}m$, $\int_V v_{\rm gal,t} x'\,{\rm d}m = \int_V v_{\rm gal,t} d_{\rm r}\,{\rm d}m$, and $\int_V v_{\rm gal,r} y'\,{\rm d}m = \int_V v_{\rm gal,r} d_{\rm t}\,{\rm d}m$ to simplify the notation, and again $\int_V x'\,{\rm d}m = \int_V d_{\rm r}\,{\rm d}m = \int_V d_{\rm t}\,{\rm d}m = 0$ as a homogenous ellipsoidal cloud has been assumed. The last term of $E'_{\rm ext,x'}$ (resp. $E'_{\rm ext,y'}$) represents the integration of the Coriolis force in the $\hat{x}'$ (resp. $\hat{y}'$) direction.

We now calculate the terms $\int_V d_{\rm r}^2\,{\rm d}m$ and $\int_V d_{\rm t}^2\,{\rm d}m$ of equations (A31) for a homogenous ellipsoidal cloud with two semi-axes (semimajor axis $X_{\rm c}$ and semiminor axis $Y_{\rm c}$) located in the orbital plane. For such a cloud, we have

$$\begin{cases} d_{\rm r} = x_{\rm maj}\cos\phi_{\rm PA} - y_{\rm min}\sin\phi_{\rm PA}, \\ d_{\rm t} = x_{\rm maj}\sin\phi_{\rm PA} + y_{\rm min}\cos\phi_{\rm PA}, \end{cases} \tag{A32}$$

where $x_{\rm maj}$ and $y_{\rm min}$ are the components of $\vec{d}_{\rm plane}$ along the major and the minor axis of the cloud, respectively, and as before $\phi_{\rm PA}$ is the angle the semimajor axis $X_{\rm c}$ makes with respect to the radial (i.e. $\hat{r}$ or $\vec{R}_0$) direction (see Fig. A1).

With equations (A32), we then have

$$\begin{aligned}\int_V d_{\rm r}^2\,{\rm d}m &= \int_V (x_{\rm maj}\cos\phi_{\rm PA} - y_{\rm min}\sin\phi_{\rm PA})^2\,{\rm d}m\\ &= \int_V \left(x_{\rm maj}^2\cos^2\phi_{\rm PA} + y_{\rm min}^2\sin^2\phi_{\rm PA}\right){\rm d}m\\ &= \cos^2\phi_{\rm PA}\int_V x_{\rm maj}^2\,{\rm d}m + \sin^2\phi_{\rm PA}\int_V y_{\rm min}^2\,{\rm d}m\\ &= \cos^2\phi_{\rm PA}\int_{-X_{\rm c}}^{X_{\rm c}} x_{\rm maj}^2\,\rho\pi Z_{\rm c}Y_{\rm c}\left(1-\frac{x_{\rm maj}^2}{X_{\rm c}^2}\right){\rm d}x_{\rm maj}\\ &\quad + \sin^2\phi_{\rm PA}\int_{-Y_{\rm c}}^{Y_{\rm c}} y_{\rm min}^2\,\rho\pi Z_{\rm c}X_{\rm c}\left(1-\frac{y_{\rm min}^2}{Y_{\rm c}^2}\right){\rm d}y_{\rm min}\\ &= b_{\rm e}M\left(X_{\rm c}^2\cos^2\phi_{\rm PA} + Y_{\rm c}^2\sin^2\phi_{\rm PA}\right),\end{aligned} \tag{A33}$$

and

$$\begin{aligned}\int_V d_{\rm t}^2\,{\rm d}m &= \int_V (x_{\rm maj}\sin\phi_{\rm PA} + y_{\rm min}\cos\phi_{\rm PA})^2\,{\rm d}m\\ &= \int_V \left(x_{\rm maj}^2\sin^2\phi_{\rm PA} + y_{\rm min}^2\cos^2\phi_{\rm PA}\right){\rm d}m\\ &= \sin^2\phi_{\rm PA}\int_V x_{\rm maj}^2\,dm + \cos^2\phi_{\rm PA}\int_V y_{\rm min}^2\,{\rm d}m\\ &= \sin^2\phi_{\rm PA}\int_{-X_{\rm c}}^{X_{\rm c}} x_{\rm maj}^2\,\rho\pi Z_{\rm c}Y_{\rm c}\left(1-\frac{x_{\rm maj}^2}{X_{\rm c}^2}\right){\rm d}x_{\rm maj}\\ &\quad + \cos^2\phi_{\rm PA}\int_{-Y_{\rm c}}^{Y_{\rm c}} y_{\rm min}^2\,\rho\pi Z_{\rm c}X_{\rm c}\left(1-\frac{y_{\rm min}^2}{Y_{\rm c}^2}\right){\rm d}y_{\rm min}\\ &= b_{\rm e}M\left(X_{\rm c}^2\sin^2\phi_{\rm PA} + Y_{\rm c}^2\cos^2\phi_{\rm PA}\right),\end{aligned} \tag{A34}$$

where $b_{\rm e}$ is the usual geometrical factor quantifying the effects of density inhomogeneities for the external gravity term ($b_{\rm e} = \frac{1}{5}$ for a homogenous cloud), we have used $\int_V x_{\rm maj}y_{\rm min}\,{\rm d}m = 0$ as a homogenous ellipsoidal cloud has been assumed, and ${\rm d}m = \rho{\rm d}V = \rho\pi Z_{\rm c}Y_{\rm c}(1-x_{\rm maj}^2/X_{\rm c}^2){\rm d}x_{\rm maj} = \rho\pi Z_{\rm c}X_{\rm c}(1-y_{\rm min}^2/Y_{\rm c}^2){\rm d}y_{\rm min}$.

Finally, substituting equation (A33) and (A34) into equation (A31), we obtain

$$\begin{cases} E_{{\rm ext},x'} = M\sigma_{\rm gal,r}^2 + b_{\rm e}M\left(T_0 - 2\Omega_0^2\right)\left(X_{\rm c}^2\cos^2\phi_{\rm PA} + Y_{\rm c}^2\sin^2\phi_{\rm PA}\right)\\ \qquad\qquad + b_{\rm e}M\Omega_0^2\left(X_{\rm c}^2\sin^2\phi_{\rm PA} + Y_{\rm c}^2\cos^2\phi_{\rm PA}\right)\\ \qquad\qquad + 2\Omega_0\int_V (v_{\rm gal,r}d_{\rm t} + v_{\rm gal,t}d_{\rm r})\,{\rm d}m,\\ E_{{\rm ext},y'} = M\sigma_{\rm gal,t}^2 + b_{\rm e}M\Omega_0^2\left(X_{\rm c}^2\cos^2\phi_{\rm PA} + Y_{\rm c}^2\sin^2\phi_{\rm PA}\right)\\ \qquad\qquad - 2b_{\rm e}M\Omega_0^2\left(X_{\rm c}^2\sin^2\phi_{\rm PA} + Y_{\rm c}^2\cos^2\phi_{\rm PA}\right)\\ \qquad\qquad - 2\Omega_0\int_V (v_{\rm gal,r}d_{\rm t} + v_{\rm gal,t}d_{\rm r})\,{\rm d}m,\end{cases} \tag{A35}$$

and thus

$$\begin{aligned}E_{\rm ext,plane} &= E_{{\rm ext},x'} + E_{{\rm ext},y'}\\ &= M\left(\sigma_{\rm gal,r}^2 + \sigma_{\rm gal,t}^2 + b_{\rm e}T_0\left(X_{\rm c}^2\cos^2\phi_{\rm PA} + Y_{\rm c}^2\sin^2\phi_{\rm PA}\right)\right.\\ &\quad \left. - b_{\rm e}\Omega_0^2\left(X_{\rm c}^2 + Y_{\rm c}^2\right)\right),\end{aligned} \tag{A36}$$

where $(\sigma_{\rm gal,r}^2 + \sigma_{\rm gal,t}^2) = \sigma_{\rm gal,plane}^2$ is the RMS velocity of in-plane gravitational motions caused by the external potential as measured in the inertial frame.

For an axisymmetric cloud ($X_{\rm c} = Y_{\rm c} = R_{\rm c}$), we thus have

$$\begin{cases} E_{{\rm ext},x'} = M\sigma_{\rm gal,r}^2 + b_{\rm e}M\left(T_0 - \Omega_0^2\right)R_{\rm c}^2\\ \qquad\qquad + 2\Omega_0\int_V (v_{\rm gal,r}d_{\rm t} + v_{\rm gal,t}d_{\rm r})\,{\rm d}m,\\ E_{{\rm ext},y'} = M\sigma_{\rm gal,t}^2 - b_{\rm e}M\Omega_0^2R_{\rm c}^2\\ \qquad\qquad - 2\Omega_0\int_V (v_{\rm gal,r}d_{\rm t} + v_{\rm gal,t}d_{\rm r})\,{\rm d}m,\end{cases} \tag{A37}$$

and

$$\begin{aligned}E_{\rm ext,plane} &= E_{{\rm ext},x'} + E_{{\rm ext},y'}\\ &= M\left(\sigma_{\rm gal,r}^2 + \sigma_{\rm gal,t}^2 + b_{\rm e}\left(T_0 - 2\Omega_0^2\right)R_{\rm c}^2\right).\end{aligned} \tag{A38}$$

APPENDIX B: EFFECTIVE VIRIAL PARAMETER

Overall, our MVT can be written simply as (see equation A14)

$$\begin{aligned}\frac{\ddot{I}}{2} &= \left(3M\sigma_{\rm sg,los}^2 - 3b_{\rm s}GM^2/R_{\rm c}\right) + E_{\rm ext}\\ &= \frac{3b_{\rm s}GM^2}{R_{\rm c}}\left(\frac{\sigma_{\rm sg,los}^2R_{\rm c}}{b_{\rm s}GM} + \frac{E_{\rm ext}}{3b_{\rm s}GM^2/R_{\rm c}} - 1\right),\end{aligned} \tag{B1}$$

where $E_{\rm ext}$ is the contribution of external gravity to a cloud's energy budget (see equations A12 and A13). We define

$$\beta \equiv \frac{E_{\rm ext}}{3b_{\rm s}GM^2/R_{\rm c}}, \tag{B2}$$

the ratio between the contribution of external gravity and the (absolute value of the) cloud's self-gravitational energy ($|U_{\rm sg}| = 3b_{\rm s}GM^2/R_{\rm c}$), so that equation (B1) can be written as

$$\frac{\ddot{I}}{2} = \frac{3b_{\rm s}GM^2}{R_{\rm c}}(\alpha_{\rm sg,vir} + \beta - 1), \tag{B3}$$

where

$$\alpha_{\rm sg,vir} \equiv \frac{\sigma_{\rm sg,los}^2R_{\rm c}}{b_{\rm s}GM} \tag{B4}$$

is the traditional virial parameter regulated by self-gravity only (see equation 13).

This naturally leads us to define an effective virial parameter

$$\alpha_{\rm eff,vir} \equiv \alpha_{\rm sg,vir} + \beta \tag{B5}$$

such that

$$\frac{\ddot{I}}{2} = \frac{3b_{\rm s}GM^2}{R_{\rm c}}(\alpha_{\rm eff,vir} - 1). \tag{B6}$$

Thus, just like the standard virial parameter, this effective virial parameter informs on the dynamical stability of a cloud. If $\alpha_{\rm eff,vir} \approx 1$, the cloud is gravitationally bound and in virial equilibrium even in the presence of the external (i.e. galactic) gravitational potential. If $\alpha_{\rm eff,vir} \gg 1$, the cloud is unlikely to be bound (i.e. it is transient unless confined by other forces). If $\alpha_{\rm eff,vir} \lesssim 1$, the molecular cloud is likely to collapse. For clouds that are (marginally) gravitationally bound, we again require $\alpha_{\rm eff,vir} \leq \alpha_{\rm vir,crit} = 2$ (Kauffmann et al. 2013, 2017), or equivalently $\beta \leq 1$ if an internal virial equilibrium is established by self-gravity (i.e. if $\alpha_{\rm sg,vir} \approx 1$; see equation 34).

Equivalently, from equation (13), we can define an effective velocity dispersion

$$\sigma_{\rm eff,los}^2 = \alpha_{\rm eff,vir}\,b_{\rm s}GM/R_{\rm c}, \tag{B7}$$

and thus our modified virial equation (equation B1) can be simplified to

$$\frac{\ddot{I}}{2} \approx \left(3M\sigma_{\rm eff,los}^2 - 3b_{\rm s}GM^2/R_{\rm c}\right). \tag{B8}$$

The parameters $\alpha_{\rm eff,vir}$ (via equation B6) or equivalently $\sigma_{\rm eff,los}$ (via equation B8) thus embody our MVT and offer a straightforward method to test the gravitational boundedness of a cloud in the presence of an external (i.e. galactic) gravitational field.

Having said that, a major challenge to calculate the effective virial parameter $\alpha_{\rm eff,vir}$ (and β) or the effective velocity dispersion $\sigma_{\rm eff,los}$ is to determine the in-plane ($\sigma_{\rm gal,r}$ and $\sigma_{\rm gal,t}$) and vertical ($\sigma_{\rm gal,z}$) RMS velocities of gravitational motions induced by the external potential in an inertial frame (see equations A12 and A13). By making increasingly stringent assumptions, we however show below that it is possible to evaluate those quantities from observables alone.

If we assume the cloud to be in vertical equilibrium, i.e. $E_{\rm ext,z} = M(\sigma_{\rm gal,z}^2 - b_{\rm e}v_0^2Z_{\rm c}^2) \approx 0$, we have

$$\beta \equiv \frac{E_{\rm ext}}{3b_{\rm s}GM^2/R_{\rm c}} \approx \frac{E_{\rm ext,plane}}{3b_{\rm s}GM^2/R_{\rm c}}. \tag{B9}$$

In this case, we only need to derive the in-plane RMS velocities of gravitational motions (i.e. $\sigma_{\rm gal,plane}^2 = \sigma_{\rm gal,r}^2 + \sigma_{\rm gal,t}^2$).

In the following, we will estimate $\sigma_{\rm gal,r}$ and $\sigma_{\rm gal,t}$ (and thereby β, $\alpha_{\rm eff,vir}$, and $\sigma_{\rm eff,los}$) using two different methods: one using observations, the other using a shear model.

Observations. Although $\sigma_{\rm gal,r}$ and $\sigma_{\rm gal,t}$ cannot be measured directly from observations, it is nevertheless possible to glean some information about them from the observables $\sigma_{\rm obs,los}$ and $\sigma_{\rm gs,los}$. Indeed, the observed velocity dispersion of a cloud $\sigma_{\rm obs,los}$ can be expressed as

$$\sigma_{\rm obs,los}^2 \approx \sigma_{\rm sg,los}^2 + \left(\sigma_{\rm gal,r}^2\sin^2\theta + \sigma_{\rm gal,t}^2\cos^2\theta\right)\sin^2 i + \sigma_{\rm gal,z}^2\cos^2 i, \tag{B10}$$

where i is the inclination of the galactic disc with respect to the line of sight, and θ is the (deprojected) azimuthal angle of the cloud's CoM with respect to the kinematic major axis of the disc (see equation 32 of Meidt et al. 2018).

Assuming that the vertical gravitational motions can be treated as random motions that balance the weight of the disc (i.e. no bulk motion in the vertical direction), analogously to turbulent motions due to self-gravity, the only bulk motions will originate from in-plane gravitational motions. The gradient-subtracted velocity dispersion $\sigma_{\rm gs,los}$ can therefore be written as

$$\sigma_{\rm gs,los}^2 \approx \sigma_{\rm sg,los}^2 + \sigma_{\rm gal,z}^2\cos^2 i. \tag{B11}$$

Our gradient-subtracted velocity dispersion $\sigma_{\rm gs,los}$ thus removed the second term (in-plane bulk gravitational motions) but kept the first term (turbulent self-gravitational motions) and last term (vertical random gravitational motions) on the right-hand side of equation (B10).

If we assume the gas motions induced by the galactic potential to be isotropic in the plane (i.e. $\sigma_{\rm gal,r} = \sigma_{\rm gal,t}$), the RMS velocities of the in-plane gravitational motions due to external gravity can easily be derived by combining equations (B10) and (B11):

$$\sigma_{\rm gal,r}^2 = \sigma_{\rm gal,t}^2 \approx \frac{\sigma_{\rm obs,los}^2 - \sigma_{\rm gs,los}^2}{\sin^2 i}. \tag{B12}$$

Substituting equation (B12) into equation (A36), we then obtain

$$\begin{aligned} E_{\rm ext} &\approx E_{\rm ext,plane} \\ &\approx M\left[\frac{2\left(\sigma_{\rm obs,los}^2 - \sigma_{\rm gs,los}^2\right)}{\sin^2 i}\right. \\ &\quad \left. + b_{\rm e}T_0\left(X_{\rm c}^2\cos^2\phi_{\rm PA} + Y_{\rm c}^2\sin^2\phi_{\rm PA}\right) - b_{\rm e}\Omega_0^2\left(X_{\rm c}^2 + Y_{\rm c}^2\right)\right], \end{aligned} \tag{B13}$$

and thus (see equations B2, B4, B5, and B7)

$$\begin{aligned} \alpha_{\rm eff,vir} \approx \frac{\sigma_{\rm gs,los}^2R_{\rm c}}{b_{\rm s}GM} + \frac{R_{\rm c}}{3b_{\rm s}GM}\left[\frac{2\left(\sigma_{\rm obs,los}^2 - \sigma_{\rm gs,los}^2\right)}{\sin^2 i}\right. \\ \left. + b_{\rm e}T_0\left(X_{\rm c}^2\cos^2\phi_{\rm PA} + Y_{\rm c}^2\sin^2\phi_{\rm PA}\right) - b_{\rm e}\Omega_0^2\left(X_{\rm c}^2 + Y_{\rm c}^2\right)\right] \end{aligned} \tag{B14}$$

and

$$\begin{aligned} \sigma_{\rm eff,los}^2 \approx \sigma_{\rm gs,los}^2 + \frac{1}{3}\left[\frac{2\left(\sigma_{\rm obs,los}^2 - \sigma_{\rm gs,los}^2\right)}{\sin^2 i}\right. \\ \left. + b_{\rm e}T_0\left(X_{\rm c}^2\cos^2\phi_{\rm PA} + Y_{\rm c}^2\sin^2\phi_{\rm PA}\right) - b_{\rm e}\Omega_0^2\left(X_{\rm c}^2 + Y_{\rm c}^2\right)\right], \end{aligned} \tag{B15}$$

where we have used $\sigma_{\rm gs,los}^2 \approx \sigma_{\rm sg,los}^2$.

For an axisymmetric cloud (i.e. $X_{\rm c} = Y_{\rm c} = R_{\rm c}$), we have

$$\begin{aligned} E_{\rm ext} &\approx E_{\rm ext,plane} \\ &\approx M\left[\frac{2\left(\sigma_{\rm obs,los}^2 - \sigma_{\rm gs,los}^2\right)}{\sin^2 i} + b_{\rm e}\left(T_0 - 2\Omega_0^2\right)R_{\rm c}^2\right], \end{aligned} \tag{B16}$$

and thus

$$\begin{aligned} \alpha_{\rm eff,vir} \approx \frac{\sigma_{\rm gs,los}^2R_{\rm c}}{b_{\rm s}GM} + \frac{R_{\rm c}}{3b_{\rm s}GM}\left[\frac{2\left(\sigma_{\rm obs,los}^2 - \sigma_{\rm gs,los}^2\right)}{\sin^2 i}\right. \\ \left. + b_{\rm e}(T_0 - 2\Omega_0^2)R_{\rm c}^2\right] \end{aligned} \tag{B17}$$

and

$$\sigma_{\rm eff,los}^2 \approx \sigma_{\rm gs,los}^2 + \frac{1}{3}\left[\frac{2\left(\sigma_{\rm obs,los}^2 - \sigma_{\rm gs,los}^2\right)}{\sin^2 i} + b_{\rm e}(T_0 - 2\Omega_0^2)R_{\rm c}^2\right]. \tag{B18}$$

B1 Shear model

For the model we will refer to as our 'shear model', we assume that all fluid elements of a cloud populate perfectly circular orbits (around the galaxy centre) determined by the galactic potential. In this case, the radial and azimuthal velocities of each fluid element measured in

the inertial frame (centred at the galaxy centre) can be written as

$$\begin{cases} v_{\rm gal,r}^{\rm mod} = -\Omega(R)R\sin\phi \\ \quad\approx -\Omega(R)d_{\rm t} \\ \quad\approx -\left(\Omega_0 + \left.\dfrac{{\rm d}\Omega(R)}{{\rm d}R}\right|_{R=R_0}(R-R_0)\right)d_{\rm t} \\ \quad\approx -\left(\Omega_0 + \left.\dfrac{{\rm d}\Omega(R)}{{\rm d}R}\right|_{R=R_0}d_{\rm r}\right)d_{\rm t} \\ \quad\approx -\Omega_0 d_{\rm t}, \\ v_{\rm gal,t}^{\rm mod} = \Omega(R)R\cos\phi \\ \quad\approx \Omega(R)R \\ \quad\approx \Omega_0 R_0 + \left.\dfrac{{\rm d}(\Omega(R)R)}{{\rm d}R}\right|_{R=R_0}(R-R_0) \\ \quad\approx \Omega_0 R_0 + \left(\Omega_0 + R\left.\dfrac{{\rm d}\Omega(R)}{{\rm d}R}\right|_{R=R_0}\right)d_{\rm r} \\ \quad\approx \Omega_0 R_0 + (\Omega_0 - 2A_0)d_{\rm r}, \end{cases} \tag{B19}$$

where as before ϕ is the angle between $\vec{R}$ and $\vec{R}_0$ (see Fig. A1), we have assumed $\cos\phi \approx 1$, $\sin\phi \approx d_{\rm t}/R$ and $R - R_0 \approx d_{\rm r}$ (as $R_{\rm c} \ll R_0$), and we have expanded $v_{\rm gal,r}$ and $v_{\rm gal,t}$ to first order about R_0 (i.e. $d_{\rm r}d_{\rm t} \approx 0$).

Using the velocity transformation between the rotating frame and the inertial frame (equation A28), we can derive the gravitational motion of each fluid element due to the external potential as measured in the rotating frame:

$$\begin{cases} v_{\rm gal,x'}^{\prime\rm mod} = 0, \\ v_{\rm gal,y'}^{\prime\rm mod} = -2A_0 d_{\rm r}, \end{cases} \tag{B20}$$

that have solutions

$$\begin{cases} x^{\prime\rm mod} = {\rm S}_2, \\ y^{\prime\rm mod} = -2A_0\,{\rm S}_2\,t + {\rm S}_3, \end{cases} \tag{B21}$$

where $\rm S_2$ and $\rm S_3$ are constants that depend on the given boundary (e.g. initial) conditions. As expected, if all fluid elements of a cloud move on perfectly circular orbits (around the galaxy centre) determined by the galactic potential, the gravitational motions of the cloud are completely dominated by shear motions and the epicyclic amplitudes vanish (cf. equation 45). We thus refer to this model as the 'shear model'.

Considering equations (B19), the mean velocities of the fluid elements of a cloud along the radial ($\hat{r}$ or $\vec{R}_0$) and azimuthal ($\hat{t}$) directions as measured in the inertial frame are

$$\begin{cases} \overline{v}_{\rm gal,r}^{\rm mod} \equiv \dfrac{1}{M}\displaystyle\int_V v_{\rm gal,r}^{\rm mod}\,{\rm d}m \\ \quad\approx \dfrac{1}{M}\displaystyle\int_V (-\Omega_0 d_{\rm t})\,{\rm d}m, \\ \quad\approx 0, \\ \overline{v}_{\rm gal,t}^{\rm mod} \equiv \dfrac{1}{M}\displaystyle\int_V v_{\rm gal,t}^{\rm mod}\,{\rm d}m \\ \quad\approx \dfrac{1}{M}\displaystyle\int_V (\Omega_0 R_0 + (\Omega_0 - 2A_0)d_{\rm r})\,{\rm d}m \\ \quad\approx \Omega_0 R_0, \end{cases} \tag{B22}$$

where as before we have used $\int_V d_{\rm r}\,{\rm d}m = \int_V d_{\rm t}\,{\rm d}m = 0$ as a homogenous ellipsoidal cloud has been assumed. The RMS velocities of gravitational motions cause by an external potential as measured in the inertial frame are thus

$$\begin{cases} \left(\sigma_{\rm gal,r}^{\rm mod}\right)^2 \equiv \dfrac{1}{M}\displaystyle\int_V \left(v_{\rm gal,r}^{\rm mod} - \overline{v}_{\rm gal,r}^{\rm mod}\right)^2{\rm d}m \\ \quad\approx \dfrac{1}{M}\displaystyle\int_V (-\Omega_0 d_{\rm t})^2{\rm d}m, \\ \quad\approx \Omega_0^2 b_{\rm e}\left(X_{\rm c}^2\sin^2\phi_{\rm PA} + Y_{\rm c}^2\cos^2\phi_{\rm PA}\right), \\ \left(\sigma_{\rm gal,t}^{\rm mod}\right)^2 \equiv \dfrac{1}{M}\displaystyle\int_V \left(v_{\rm gal,t}^{\rm mod} - \overline{v}_{\rm gal,t}^{\rm mod}\right)^2{\rm d}m \\ \quad\approx \dfrac{1}{M}\displaystyle\int_V ((\Omega_0 - 2A_0)d_{\rm r})^2{\rm d}m, \\ \quad\approx (\Omega_0 - 2A_0)^2 b_{\rm e}\left(X_{\rm c}^2\cos^2\phi_{\rm PA} + Y_{\rm c}^2\sin^2\phi_{\rm PA}\right), \end{cases} \tag{B23}$$

where equations (A33) and (A34) have been used for the integrals $\int_{\rm V} d_{\rm r}^2\,{\rm d}m$ and $\int_{\rm V} d_{\rm t}^2\,{\rm d}m$ for a homogenous ellipsoidal cloud.

Substituting equation (B23) into equation (A36), we obtain

$$\begin{aligned} E_{\rm ext}^{\rm mod} &\approx E_{\rm ext,plane}^{\rm mod} \\ &\approx 4A_0^2 b_{\rm e} M\left(X_{\rm c}^2\cos^2\phi_{\rm PA} + Y_{\rm c}^2\sin^2\phi_{\rm PA}\right), \end{aligned} \tag{B24}$$

and thus (see equations B2, B5, and B7)

$$\alpha_{\rm eff,vir}^{\rm mod} = \alpha_{\rm sg,vir} + \frac{4A_0^2 b_{\rm e}\left(X_{\rm c}^2\cos^2\phi_{\rm PA} + Y_{\rm c}^2\sin^2\phi_{\rm PA}\right)}{3b_{\rm s}GM/R_{\rm c}} \tag{B25}$$

and

$$\left(\sigma_{\rm eff,los}^{\rm mod}\right)^2 = \sigma_{\rm sg,los}^2 + \frac{4A_0^2 b_{\rm e}\left(X_{\rm c}^2\cos^2\phi_{\rm PA} + Y_{\rm c}^2\sin^2\phi_{\rm PA}\right)}{3}. \tag{B26}$$

For an axisymmetric cloud (i.e. $X_{\rm c} = Y_{\rm c} = R_{\rm c}$), we then have

$$\begin{aligned} E_{\rm ext}^{\rm mod} &\approx E_{\rm ext,plane}^{\rm mod} \\ &\approx 4A_0^2 b_{\rm e} M R_{\rm c}^2, \end{aligned} \tag{B27}$$

and thus

$$\alpha_{\rm eff,vir}^{\rm mod} = \alpha_{\rm sg,vir} + \frac{4A_0^2 b_{\rm e} R_{\rm c}^2}{3b_{\rm s}GM/R_{\rm c}} \tag{B28}$$

and

$$\left(\sigma_{\rm eff,los}^{\rm mod}\right)^2 = \sigma_{\rm sg,los}^2 + \frac{4A_0^2 b_{\rm e} R_{\rm c}^2}{3}. \tag{B29}$$

Finally, if we assume an internal virial equilibrium has been established by self-gravity (i.e. $3M\sigma_{\rm sg,los}^2 - 3b_{\rm s}GM^2/R_{\rm c} \approx 0$) and the cloud is in vertical equibrium (i.e. $E_{\rm ext,z} \approx 0$), our shear model predicts that

$$\begin{aligned} \frac{\ddot{I}^{\rm mod}}{2} &\approx E_{\rm ext,plane}^{\rm mod} \\ &\approx 4A_0^2 b_{\rm e} M\left(R_{\rm c}^{\rm mod}\right)^2 \\ &= 2A_0^2 I^{\rm mod}, \end{aligned} \tag{B30}$$

where $I^{\rm mod} = 2b_{\rm e}M(R_{\rm c}^{\rm mod})^2$ for a spherical cloud. As $A_0 > 0$ for all clouds, we easily obtain $I^{\rm mod} \propto e^{2A_0 t}$ and thus $R_{\rm c}^{\rm mod} \propto e^{A_0 t}$ and $\Sigma_{\rm gas}^{\rm mod} \propto e^{-2A_0 t}$ for a spherical cloud with a constant mass. This suggests that, if all fluid elements of a cloud move on perfectly circular orbits (around the galaxy centre) determined by the galactic potential, a cloud experiencing strong shear will grow larger and larger and become less and less bound over a timescale $\sim 1/2A_0$, which we name the 'shear time-scale'.

APPENDIX C: STELLAR DENSITY CALCULATION

For a number of calculations, we must know the local stellar mass density at the position of each cloud ($\rho_{*,0}$). For this, we adopt the

MGE formalism of Emsellem et al. (1994) and Cappellari (2002), and specifically the existing model of NGC 4429 from Davis et al. (2018), constrained from dynamical modelling of the same molecular gas data as used here.

In short, the luminous matter distribution was first parametrized using an MGE model of the stellar light, constructed by applying the `MGE_FIT_SECTORS` package of Cappellari (2002) to a *HST* Wide-Field Planetary Camera 2 *F606W* image combined with an r'-band image from the Sloan Digital Sky Survey (Adelman-McCarthy et al. 2008). Each Gaussian component j of the model has an observed surface brightness I_j, standard deviation (width) σ_j and axial ratio q_j. The best-fitting MGE model is tabulated in table 1 of Davis et al. (2018) and is shown visually in their fig. 7. Using this MGE parametrization, the surface brightness distribution of the galaxy can be accurately reproduced (see equation 12 of Cappellari 2008). The next step is to obtain the intrinsic luminosity density by deprojecting the surface brightness model, which the MGE parametrization allows to do trivially under the assumption of (oblate) axisymmetry and a known inclination (see equation 13 of Cappellari 2008). The stellar density of the cloud is then derived by multiplying the deprojected MGE luminosity density with the (spatially variable) stellar mass-to-light ratio $\Psi(R_{\rm gal})$ derived from the Davis et al. (2018) dynamical modelling:

$$\rho_*(R_{\rm gal}) = \Psi(R_{\rm gal}) \sum_j^N \frac{I_j q_j}{\sqrt{2\pi}\,\sigma_j q'_j} \exp\left(-\frac{R_{\rm gal}^2}{2\sigma_j^2}\right), \tag{C1}$$

where we have assumed that all the clouds are in the equatorial plane ($z = 0$), $R_{\rm gal}$ is the galactocentric distance (radius in the plane of the disc) of the cloud as usual, q'_j is the intrinsic axial ratio of the jth Gaussian component,

$$q'_j = \frac{\sqrt{q_j^2 - \cos^2 i}}{\sin i}, \tag{C2}$$

(note that Cappellari 2008 instead uses q and q' for the intrinsic and the observed axial ratio, respectively), and the sum is taken over the N Gaussian components. The derived central stellar mass density of each cloud is listed in Table 3 and ranges from 6 to 60 $\mathrm{M_\odot\,pc^{-3}}$.

This paper has been typeset from a TEX/LATEX file prepared by the author.